ELECTRONIC AND MAGNETIC PROPERTIES OF METAL CLUSTERS

THESIS SUBMITTED FOR THE DEGREE OF DOCTOR OF PHILOSOPHY (SCIENCE) OF THE JADAVPUR UNIVERSITY

MUKUL KABIR

SATYENDRA NATH BOSE NATIONAL CENTRE
FOR BASIC SCIENCES
JD BLOCK, SECTOR III, SALT LAKE CITY
KOLKATA 700 098, INDIA

NOVEMBER, 2006

CERTIFICATE FROM THE SUPERVISOR

This is to certify that the thesis entitled **Electronic and Magnetic Properties of Metal Clusters** submitted by **Md. Mukul Kabir**, who got his name registered on **May 17, 2004** for the award of **Ph.D. (Science) degree** of **Jadavpur University**, is absolutely based upon his own work under the supervision of **Professor Abhijit Mookerjee** at **S. N. Bose National Centre For Basic Sciences, Kolkata, India** and that neither this thesis not any part of its has been submitted for any degree/diploma or any other academic award anywhere before.

ABHIJIT MOOKERJEE
Senior Professor and Head
Department of Material Sciences
Satyendra Nath Bose National Centre For Basic Sciences,
JD Block, Sector III, Salt Lake City, Kolkata 700 098
INDIA
Date :

to my parents

Acknowledgments

A journey is easier when we travel together. This thesis is the result of five years of work whereby I have been accompanied and supported by many people. It is a pleasant aspect that I now have the opportunity to express my gratitude for all of them.

The first person I would like to thank is my supervisor Prof. Abhijit Mookerjee. I have been introduced to him in 2000 through 'Symmetries in Quantum Mechanics', when I was in my MSc. Since then his enthusiastic and integral view on research have made a deep impression on me. He could not even realize how much I have learned from him. He gave me enough freedom in thinking, choosing my own problems and collaborating with other colleagues which helped me to bring out my best. I owe him my sincere gratitude for having me shown this way of research. Besides of being an excellent supervisor, he is as close as a relative and a good friend to me. I am really glad that I have come to know him in my life.

I am glad to thank Prof. D. G. Kanhere for an active collaboration on 'Magnetism in pure and doped manganese clusters'. I am grateful to him for allowing me to use every resource in his laboratory during my visit in 2004. I would also like to thank Dr. Tanusri Saha Dasgupta for her continuous encouragement during this period. Valuable discussions and an active collaboration with her helped me to expand my area of research and to grow myself. It is a great pleasure to acknowledge Dr. P. A. Sreeram for his neverending help on any computer related problems. He always had the right answer whenever I knocked his door. I express my sincere thanks to him for all his help and becoming a very good friend. During this period, I enjoyed all scientific and nonscientific discussions with him.

I would like to express my sincere gratitude to Prof. S. Dattagupta who always kept an eye on the progress of my work and was always available when I needed his advice. I have learned a lot on the realm of science and life from him and he is a neverending source of inspiration.

I had the pleasure to supervise and work with few juniors in the group, which have been beneficial for this thesis. Soumendu and Shreemoyee worked on Cobalt clusters with me, which are discussed in chapter 7. I have enjoyed working with my friends like Sudipta and Malay on the 'Electronic structure of DNA'. I have also enjoyed an active collaboration with Dr. Biplab Sanyal and Diana Iusan of Uppasala University on 'Spintronic Materials'. Although this is out of the interest of the present thesis but it helped me to grow up. I thank them all for becoming my friend and for their active collaboration.

Life is always been a tough task without good friends. During these years I have been accompanied by my friends: Rupa, Atis, Monodeep, Jose, Ain-Ul, Kamal, Mani, Suman,

Jayee, Tomaghna, Soumen and Suvankar. I thank them all for standing beside me all the time. It is my pleasure to thank Dulal'da for his patience over the years.

Financial support from Warwick University for the first couple of years and then form the Department of Science and Technology, India is gratefully acknowledged. Some of the works have been done during my visit to Pune University and Uppasala University. I take this opportunity to acknowledge the congenial hospitality at both the universities.

Mukul Kabir
Kolkata, India
November, 2006

List of Publications

1. **Mukul Kabir**, Abhijit Mookerjee, R. P. Datta, Amitava Banerjea and A. K. Bhattacharya
   Study of small metallic nanoparticles : An ab-initio full-potential muffin-tin orbitals based molecular dynamics study of small Cu clusters.
   Int. J. of Mod. Phys. B 17, 2061, (2003); Citation: 7

2. **Mukul Kabir**, Abhijit Mookerjee and A. K. Bhattacharya
   Structure and stability of Cu clusters : A tight-binding molecular dynamics study.
   Physical Review A 69, 043203 (2004); Citation: 20

3. **Mukul Kabir**, Abhijit Mookerjee and A. K. Bhattacharya
   Copper clusters : Electronic effect dominates over geometrical effect
   European Physical Journal D 31, 477 (2004); Citation: 4

4. **Mukul Kabir**, Abhijit Mookerjee and A. K. Bhattacharya
   Tight-Binding Molecular Dynamics Study of Copper Clusters
   Nano-Scale Materials: From Science to Technology Eds., S.N.Sahu, R.K. Choudhury and P. Jena (Nova, New York, 2006).

5. **Mukul Kabir**, Abhijit Mookerjee and D. G. Kanhere
   Structure, electronic properties and magnetic transition in manganese clusters
   Physical Review B 73, 224439 (2006); Also at Virtual Journal of Nanoscale Science and Technology, Vol. 14 (2006).

6. **Mukul Kabir**, D. G. Kanhere and Abhijit Mookerjee
   Emergence of noncollinear magnetic ordering in small magnetic clusters
   Submitted to Phys. Rev. B (2006).

7. **Mukul Kabir**, D. G. Kanhere and Abhijit Mookerjee
   Large magnetic moments and anomalous exchange coupling in As-doped Mn clusters
   Physical Review B 73, 75210 (2006).

8. **Mukul Kabir**, Abhijit Mookerjee, D. G. Kanhere
   Magnetism in pure and doped manganese clusters.
   Lecture series on computer and computational sciences, Vol-4 pp 1018-1021 (Brill Academic Publishers, The Netherlands, 2005).

9. S. Datta, **Mukul Kabir**, S. Ganguly, Biplab Sanyal, T. Saha Dasgupta and Abhijit Mookerjee
   Structure, bonding and magnetic properties of Co_n clusters
   Submitted to Phys. Rev. B (2006).

10. **Mukul Kabir**, Abhijit Mookerjee and D. G. Kanhere
    Magnetism in pure and doped manganese clusters: A review
    Atomic and Molecular Clusters: New Research (Nova, New York, 2006).

Contents

List of Figures

List of Tables

Chapter 1

Introduction

There is enough room at the bottom.

- Richard P. Feynman

1.1 What are clusters?

From the time of John Dalton, when the idea of atoms as building blocks of matter became generally accepted, there have been two distinct strands in the study of materials : on one hand one looks at molecules and atoms and then look downward leading to nuclear and particle physics, on the other hand one can also study the many body problem of interacting atoms and electrons, as many as $\sim O(10^{22})$ (in principle treated as infinitely many). Between these two extreme limits are clusters of a few atoms. The effort now is to bridge this gap and understand how atomic properties cross-over to those of bulk solids made out of those atoms.

Since late 1970's interest in the study of what have come to be called clusters has grown exponentially. This is because of two reasons : first, the need to understand how properties change in this reduced dimension from a fundamental physics point of view, and second, the knowledge of how one can manipulate these properties to obtain materials for specific applications in the modern and future technologies.

Clusters are generally aggregates of atoms and molecules intermediate in size between the bulk matter and the individual atoms and molecules. Clusters can be classified

as small, medium-sized and large depending upon the number of constituent atoms or molecules. Small clusters are those whose "properties" vary abruptly as we change their sizes and shapes. So that we cannot assign a smooth variation of their properties as a function of size. If, on the other hand, these "properties" vary relatively smoothly with the number of component atoms, nevertheless showing significant finite size effects, then those clusters are called medium-sized or large. Clusters can be homogeneous, that is, made of one kind of atom or molecule or can be heterogeneous, that is, composed of more than one kind.

The properties of the clusters differ considerably from both bulk and individual atoms or molecules [1, 2]. As compared to bulk materials, clusters have a very large surface to bulk volume ratio, i.e. a large fraction of the constituent particles lie on the surface . This makes surface chemistry extremely important in determining their properties. On the other hand molecules are characterized by definite composition and structure and clusters differ in both. Clusters may be composed of any number of atoms or molecules. The "most stable structure" depends upon the number of particles into it. However, it is possible to have many stable local structures for a particular sized cluster within very small energy window from the most stable or the ground state structure and these are called as 'isomers'. The number of isomers increases very rapidly with the number of atoms constituting the clusters. Consequently, the number of local minima in the potential energy surface increases exponentially with the number of atoms in the cluster. Not only the structure, but most of the properties like binding energy, relative stability, energy level spacing, magnetism and bonding also depend sharply on the number of atoms constituting the cluster.

1.2 Why are clusters interesting?

Cluster science is currently one of the most active and evolving fields of research in both physics and chemistry and attracts attention from both the basic scientific viewpoint and also from the viewpoint of their potential technological applications. As mentioned earlier, these systems bridge the domains of atomic and molecular physics on one hand and condensed matter physics on the other. Their properties are dominated by their large

surface-to-volume ratio, providing a unique opportunity for us to study the interplay between surface and volume effects. Clusters exhibit discrete spectroscopy because of their finite size. Here we enumerate some of the specific questions which have been under investigation from the fundamental view point.

- How are cluster properties influenced by electron delocalization? Quantum mechanical degrees of freedom give rise to the shell structure and magic numbers in clusters similar to nuclei. The insulator-metal transition is an aspect which can be studied in these systems. Although we have to be careful how we define metallicity or otherwise in a finite system. One way is to check whether the HOMO (highest occupied molecular orbital) in the ground state is partially filled or fully occupied with electrons. In fact, in clusters one sees a richer behavior, with the shells organized into super-shells. Moreover, in metal and semiconductor clusters the electronic shell structure and geometric shell structure compete to determine the shape and stability. Shell effects may be pronounced in the ionization potentials of metallic clusters.

- What determines the cluster geometry? The existence of spherical shells in alkali metal clusters proves that the electron delocalization can be crucial, forcing near-spherical geometric shapes at specific electron numbers. There are many other possibilities as well. For Lennard-Jones systems such as the noble gas (Ar, Xe, etc.), one see polyhedral shapes having highest symmetry possible in finite systems namely icosahedra. The possibility of phase change into amorphous of clusters and and their thermal stability is of interest. As are the ways of identifying critical parameters that uniquely signal this phase change. Carbon clusters have an especially rich set of shapes, including chains, rings, buckyballs, tubes and onions.

- What are the collective degrees of freedom and the elementary excitations of atomic clusters ? In a system with delocalized electrons, at some frequencies the electrons respond to an external field collectively like a plasmon resonance. The form of electron-electron interaction is still a topic which needs further refinements. The position and the line shape of the plasmon carry valuable information about the

geometry, shape fluctuation, geometry of the packing and temperature of the cluster and about the electron-ion coupling.

- What is the electron-ion interaction? The interaction of electronic degrees of freedom with geometric or vibrational degrees of freedom (phonons) is a subject of tremendous interest. The alkali-doped fullerenes may provide the best examples of BCS superconductors with the pairing driven by the intra-molecular vibrational coupling.

- At this point it is obvious to ask, "How does magnetism behave in this 'reduced' dimension and how does it approach the bulk limit ?" Experiments show that the magnetic behaviour differs considerably in this size regime from the corresponding bulk behaviour. The magnetic properties of clusters reveal a series of interesting and unexpected features such as non-monotonic dependence of magnetization on particle number or external field, strong magnetism in normally nonmagnetic elements. Generally an enhancement in the magnetic moment has been observed, which can be understood from the strong *d*-electron localization. This resulted from the reduced atomic coordination in this finite system. However, the variation of the magnetic moment with the size of the cluster (i.e. with the number of atoms in the cluster) is not at all smooth for small clusters and gives interesting local structures. Another obvious question is, "At what size of the cluster do the magnetic properties resembles the bulk behaviour?" The observed superparamagnetism of small magnetic clusters provides a new impetus to try to understand the coupling between spin and other degrees of freedom. Previously, magnetic clusters were embedded in a rare gas and their magnetism studied by electron spin resonance (ESR) technique, for example. However, due to tremendous improvements in present day technology, now it is possible to produce free standing clusters and measure their magnetic moment by the Stern-Gerlach experiment. Magnetism in finite systems is an interesting and evolving field in cluster science, which include tremendous notions to the basic sciences to the emerging new technology.

- Do we understand the notion of " phase transitions" , which are thermodynamic or bulk phenomena, when one shrinks the system to finite sized clusters ? Do finite

sized materials "melt" ? In the case of magnetic clusters, do they have a Curie temperature ? In this context one important question is : "In finite systems, what is analogous to a second-order transition in bulk ?" Experimentally, there is indirect evidence so far for some of these interesting aspects. Atomic and molecular clusters provide tools for studying potential landscapes, the microscopic factors that lead to either glass formation to 'structure- seeking" or crystal formation and protein formation.

- Cluster-cluster, atom-cluster and electron-cluster interactions are themes which emerge both experimentally and theoretically.

- Interaction of cluster with external fields like strong laser fields, where the nonlinear response of the system has to evaluated is an emerging field of interest.

- Quantum confinement as seen in quantum dots presents a plethora of very exciting phenomena: exciton confinement, collective excitation, conductance fluctuations etc. It seems that the studies of Coulomb clusters confined in an external potential are also interesting for both theory and applications. The quantum systems with the Coulomb interaction are electrons and holes in the quantum dots and wires. The low dimensionality leads to a lot of new effects and allows to treat the transition from cluster to bulk and cluster melting with larger assurance.

This list, along with many more, merely illustrates the richness of the field and its tremendous potential. Since the properties of the clusters depend upon their size, it gives us a wide opportunity to tailor their electronic, chemical, optical and magnetic properties for use in emerging nanotechnologies. The chemical reactivity of metal clusters have far-reaching consequences for catalysis. Small metal clusters provide both a large surface-to-volume ratio and properties, such as activity, selectivity and stability, that have been tailored to catalyze specific reactions. Electronic and optical properties of the clusters are tailored for their particular use in e.g information storage, lasers whose properties can be fine-tuned by the variation of cluster size. Metal clusters with closed electronic shell are very stable and have been shown to have high potential to absorb hydrogen, which can be used as building blocks for a new hydrogen storage material.

Magnetic clusters and their self-organized assembly of surfaces can be employed in the development of recording media. These magnetic particles should be magnetically hard, i.e. they do not easily loose their magnetization direction once the external magnetic field is removed. On the other hand, soft magnetic nanoparticles open applications in entirely different areas For example, combining biomolecules with a single magnetic nanoparticles will initiate new advances in medical diagnostics, drug targeting or innovative cancer therapies. The opportunity to deliberately control the movement of the magnetic nanoparticles together with the fact that magnetic fields penetrate human tissues without impediment allow nanoparticles to carry and deliver packages, such as anticancer drugs or radioactive atoms, to a targeted area. Additionally, magnetic nanoparticles respond strongly to time-modulated magnetic fields, and hence enable dynamic methods of cancer treatment, and they could be used to enhance the contrast in magnetic resonance imaging. Finally, the viscoelastic architecture inside the living cells can be studied by controlled positioning of magnetic nanoparticles into the internal skeleton of cells, and following the response of the nanoparticles to dynamic magnetic fields. Magnetic nanoparticles offer tremendous scientific possibilities and will offer more as this field matures. Gold nanoclusters have been studied with the short segment with DNA, which could form the basis of an easy-to-read test to single out genetic sequences.

1.3 Transition metal clusters

1.3.1 Electronic configuration and bonding

The presence of the unfilled d shell in transition metal elements has a number of important consequences. Because of different ways of arranging the electrons in the unfilled d shell and the fact that the $(n+1)s$ shell is almost isoenergetic with the nd shell, there are large number of low lying excited electronic states possible. This is partly responsible for the important chemical properties of the transition metals.

Morse [3] has pointed few important factors to be considered : the size of the $(n+1)s$ and nd orbitals and the $(n+1)s^2nd^m \rightarrow (n+1)s^1nd^{m+1}$ promotion energy. The $(n+1)s$ orbitals are larger than the nd orbitals so the former have larger contribution to bonding. The nd orbitals contract moving to the right in the periodic table and expand moving

down the periodic table. Thus nd contribution to the bonding is expected to be more important for the second and third transition series than the first. The importance of the $(n+1)s^2nd^m \rightarrow (n+1)s^1nd^{m+1}$ promotion energy can be demonstrated by considering the Mn_2 dimer. Mn atom has half-field d and fully-filled s ($4s^2\ 3d^5$) electronic configuration. Due to the stability of the half-filled d shell the $4s^2\ 3d^5 \rightarrow 4s^1\ 3d^6$ promotion is large, namely 2.14 eV [4]. Its ground state is $(4s\sigma_g)^2\ (4s\sigma_u^*)^2\ (3d)^{10}$ and the binding energy is very low, varies between 0.10 ± 0.1 to 0.56 ± 0.26 eV [3, 5, 6, 7]. These are often called van der Walls molecules and have zero formal bond order. The dissociation energy of the Mn_2^+ cation is rather large, namely 1.39 eV [8]. It has an electronic configuration $(4s\sigma_g)^2$ $(4s\sigma_u^*)^1\ (3d)^{10}$ and formal bond order 1/2. Therefore, this 1/2 bond appears to be worth ~ 1 eV energy. Thus it is clear that Mn_2 can not recoup the 2.14 eV promotion energy from increased bonding and so it has a $(4s\sigma_g)^2\ (4s\sigma_u^*)^2\ (3d)^{10}$ instead of $(4s\sigma_g)^2\ (4s\sigma_u^*)^1$ $(3d)^{11}$ configuration.

However, for other transition metals the promotion energies are generally much smaller (for example it is 0.87 eV for Fe) and there is a delicate balance between the promotion energy and the energy gain in increased bonding.

The nature and relative contribution of the nd orbitals to the bonding is not well understood. Cu_2 has an electronic configuration $3d^{10}\ 3d^{10}\ 4s\sigma_g^2$ while Cu atom has a $4s^1\ 3d^{10}$ configuration. However, it is necessary to consider the d electrons in order to reproduce the correct equilibrium dissociation energy, bond length and vibrational frequency. Correlation of the $3d$ electrons increases the calculated bond energy of Cu_2 by 0.8 eV [9]. Correlation reduces the $d-d$ repulsion and allow the atoms to move closer forming a strong $4s\sigma_g^2$ bond.

1.3.2 Shell effects and magic numbers: Cu, Ag and Au clusters

Cu, Ag and Au atoms lie at the end of the $3d$, $4d$ and $5d$ periods, respectively, and are often called noble metals. The d shell is filled with 10 electrons and the valence shell contains a single s electron. This leads one to expect some similarities between small clusters of noble metals and the clusters of alkali metals. Experiments for noble metal clusters (Cu_n, Ag_n and Au_n) indicate the existence of shell effects similar to those observed in alkali clusters

[10, 11]. For example, the mass spectrum of Ag_n^+ clusters obtained by bombarding the metal with inert-gas ions show expected similarities with the alkali clusters. For small clusters and odd-even alternation of the cluster intensities is observed, i.e the intensity of the odd-N clusters is greater than the intensity of even-N clusters. On the other hand a steep drop in the cluster intensities occur at N = 3, 9, 21, 35, 41 and 59. The reason for both this observation is similar to those in alkali clusters. Therefore, the mass spectrum reflects the relative stabilities of charged clusters in which the number of electrons, which take part in the bonding, is $N - 1$. This reflects that a cluster with 2, 8, 20, 34, 40, 58 ... electrons are relatively more stable than the others i.e the electronic shell is closed for these number of electrons. This is known as electronic 'magic numbers'. Mass spectra of Cu_n^+ and Au_n^+ also show the same magic numbers. Furthermore, the negatively charged clusters, Cu_n^-, Ag_n^- and Au_n^-, have magic number corresponding to N = 7, 19, 33, 39, 57, ... , which again have a total 8, 20, 34, 40, 58 electrons. Winter *et al.* [12] have measured the mass spectrum of Cu clusters generated by laser vaporization of copper and these have passed through a flow tube reactor with O_2 and found that the Cu_{20}, Cu_{34}, Cu_{40}, Cu_{58} and Cu_{92} are nonreactive toward O_2. This lack of reactivity is attributed to the corresponding electronic shell closing leading to greater stability of these clusters. Measurements of ionization potential of Cu clusters show an expected drop at the electronic shell closing [13]. Moreover, the photo-electron threshold should reflect the shell effects. Indeed, the measured photo-detachment-energies of Ag_n^- [14] and Cu_n^- [15, 16] show drops between N= 7 and 8 and between N=19 and 20, which again reflects the shell closing.[1]

1.3.3 Magnetic properties

What has been observed experimentally?

Magnetic properties of transition-metal clusters are very fascinating and unique; and the search for it largely motivated by the fundamental question," How do the magnetic properties behave in reduced dimension and how they evolve toward the bulk limit as size increases. Here in this section we concentrate on the internal magnetic structure. Several unexpected magnetic behaviours have already been observed in transition metal clusters:

[1] All these would be largely discussed in the Chapter 3.

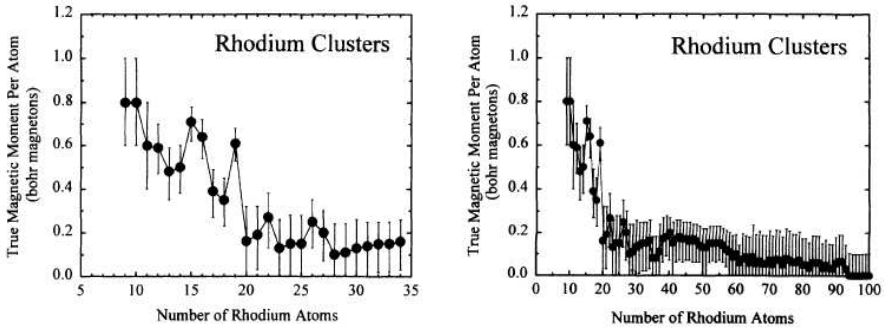

Figure 1.1: (Left) Size dependence of the magnetic moment per atom of Rhodium cluster in the size range $N \leq 100$. The magnetic moment decreases with the cluster size and approaches toward zero, the bulk value for $N \geq 60$. (Right) The same has been plotted for the size range Rh_9 - Rh_{34}. The Rh_{15}, Rh_{16} and Rh_{19} exhibit anomalously large magnetic moment. Adopted from Cox *et al.* (Ref. [17]).

1. *Non-zero magnetic moment in the clusters of nonmagnetic bulk material.* For example, Cox and co-workers found that the bare rhodium clusters display non-zero magnetic moment for sizes less than 60 atoms [17]. This is an indication of either ferromagnetic or ferrimagnetic ordering even though the bulk rhodium is a Pauli paramagnet at all temperature Fig.1.1 shows that Rh_n clusters have strong size dependent magnetism The magnetic moment per atom decreases as the cluster size increases and become non-magnetic above sizes of 60 atoms or more [17].

2. *Enhancement of magnetic moment in the clusters which is already ferromagnetic in bulk.* For example, Fe_n clusters [18], it was found that the magnetic moment per atom is larger than the bulk value and oscillates with the size of the cluster, slowly approaching its bulk value (2.2 μ_B/atom) as the number of Fe atoms in the cluster increases. This has been shown in the Figure 1.2. Earlier Bloomfield and co-workers [19, 20] and de Heer group [21], and very recently, Knickelbein [22] and Xu *et al.* [23] found that the magnetic moment of free Co clusters are larger than 2 μ_B/atom in the size range $N \leq 200$, which is larger than its bulk value (1.71 μ_B/atom [24]). It is observed that the magnetic moment per atom increases from 2 μ_B/atom for Co_{12} and reaches a maximum for Co_{34} followed by a general decrease (Figure 1.2),

with weak oscillations, to 2 μ_B for $N = 150$.

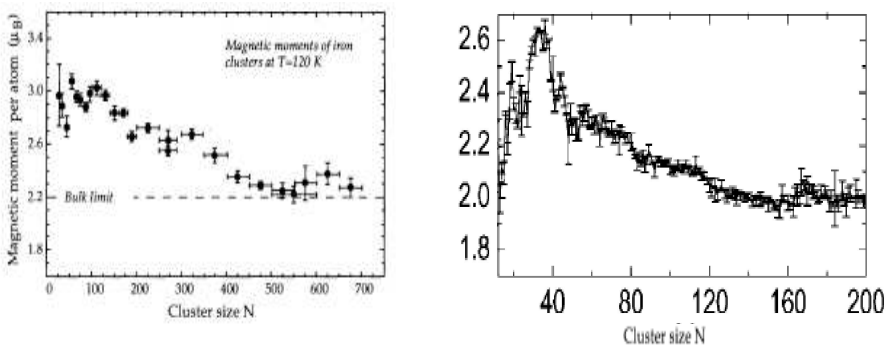

Figure 1.2: (Left) Size dependence of the magnetic moment per atom of Fe_n cluster ($n < 100$). The magnetic moment decreases with the cluster size and approaches toward zero, the bulk value for $N \geq 60$. Adopted from Billas *et al.* [18]. (Right) Plot of magnetic moment per atom for Co_n clusters in the size range $12 \leq n \leq 200$. Adopted from Xu *et al.* [23]

3. *Finite magnetic moment observed in the atomic clusters which are antiferromagnetic as bulk.* For example,the Cr_n [25]and Mn_n [26, 27] clusters have shown such behaviour. It has been found that Cr_n clusters have magnetic moment 0.5-1 μ_B per atom. Very recently, Knickelbein observed, Mn_5 - Mn_{99} clusters posses finite magnetic moment. Whereas, the most stable α-Mn exhibits a complex antiferromagnetic order below the Néel temperature of 95 K and is nonmagnetic at room temperature. The size dependent magnetic behaviour is shown in the Figure 1.3.

Therefore, in general, the magnetic moments in these finite clusters are enhanced compared to their bulk values. This can be understood from the fact that due to low coordination the *d*-electrons are more localized. However, in all cases, the variation of magnetic moment is not a smooth function of cluster size giving rise to unique local structures to the size dependence of magnetic moments. For example, Mn_n clusters [26, 27] show relative decrease in their magnetic moment at n=13 and 19. Generally the uncertainty in the measurement decreases as the number of atoms in the cluster increase as the cluster production efficiency increases with the size. However, the uncertainty in

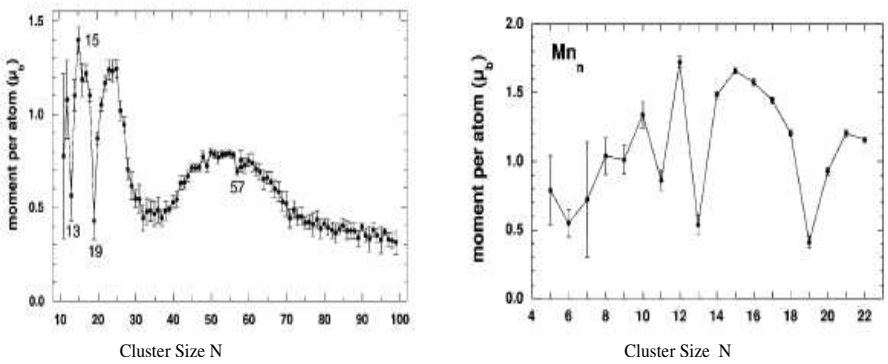

Figure 1.3: (Left) Plot of magnetic moment per atom as a function of cluster size N for manganese cluster for the size range $11 \leq N \leq 100$. (Right) The same has been plotted for the size range 5-22. Both of the figures are after Knickelbein (Ref. [26] and Ref. [27])

the measured magnetic moment is very high ($\pm$ 58% of the measured value) for Mn_7 cluster [27]. All these will be discussed in the Chapter 4.

How is the magnetic moment measured experimentally?

For all the results discussed, the magnetic moments of the free clusters have been measured through the Stern-Gerlach experiment. A schematic diagram of the experiment is shown in the Figure 1.4. Metal clusters are produced in a laser vaporization cluster source, leave the source in a supersonic expansion of helium gas and form a cluster beam. This cluster beam passes through a series of collimating slits and a rotating beam chopper before entering the gradient field magnet.

The beam chopper allows us to determine the cluster beam's velocity and measure how long the cluster resides inside the source's growth region before entering the beam. Only after residing for a long time in the source, the clusters come into the thermal equilibrium with the source, and thereby one can control the cluster temperature by controlling the source temperature. The temperature of the source, and so also the temperature of the cluster, is controlled by a cryorefrigerator. We can control the cluster temperature over a range $\sim$ 60 — 300 K. This temperature control is essential.

As they pass through the gradient magnet, the magnetic clusters experience transverse

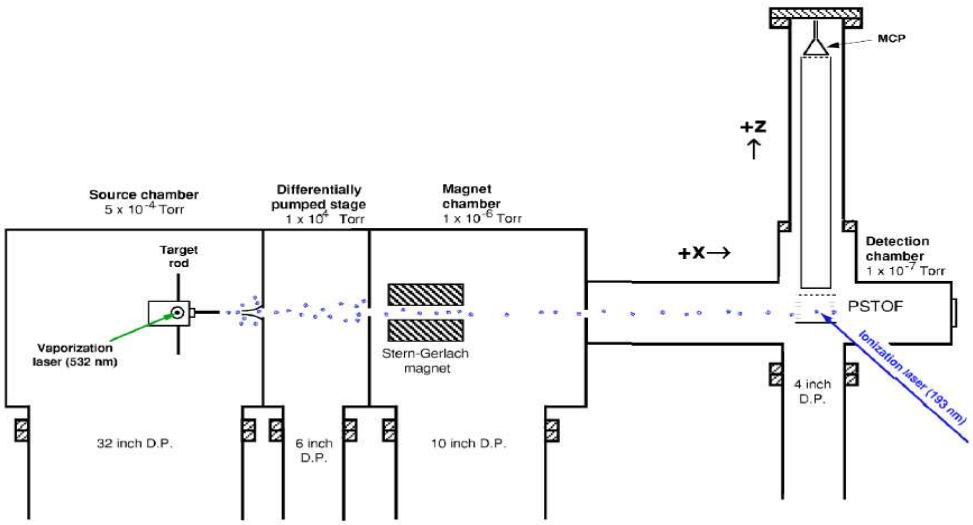

Figure 1.4: Schematic diagram of the Stern-Gerlach cluster beam experiment. Adopted from Knickelbein (Ref. [27]).

forces and begin to deflect. This deflection continues until the cluster reaches the detection region. There the clusters are photoionized by a narrowly collimated laser beam and identified in time-of-flight mass spectrometer. The ionizing beam is scanned across the cluster beam profile to determine the extent to which the clusters were deflected by the magnetic field.

All the clusters deflect toward the strong field and each cluster profile is merely shifted over, not broadened, indicating that the clusters of a single size deflect homogeneously toward the high field side. This homogeneous, single sided deflection is the signature of a relaxation process that causes the cluster to forget their initial conditions as it passes through the magnet. This behaviour is known as superparamagnetism. Here the measured magnetic moment is actually the time-averaged projection of the true, internal moment on the external magnetic field. In a small mono-domain particle, the thermal energy can exceed the magnetocrystaline anisotropy energy and decouple the magnetic moment's orientation from that of the atomic lattice. The internal moment of such a particle fluctuates rapidly in orientation, under thermal fluctuation. In the absence of external magnetic field , all orientations of the magnetic moment are equally likely and the magnetic moment is entirely masked at long time scales by thermal averaging process.

Only in a strong magnetic field and at low temperatures, the internal magnetic moment of a superparamagnetic particle becomes apparent. When the interaction energy between the internal magnetic moment and the external magnetic field becomes comparable to the thermal energy, the time averaged magnetic moment begins to shift noticeably toward alignment with the external field. This response is similar to the paramagnetic behavior but because it involves the giant moment of the entire particle it is called superparamagnetism.

The measurement time of the cluster magnetic moment is much larger than the nanosecond time scale of the thermal fluctuations, so we can observe only the time-averaged of effective magnetic moment of a superparamagnetic cluster and not the internal moment itself. The effective magnetic moment per atom μ_{eff} is reduced from the internal moment per atom μ by a factor of the Langevin function $\mathcal{L}$:

$$\mu_{\text{eff}} = \mu \mathcal{L}\left(\frac{N\mu B}{k_B T}\right) = \mu\left[\coth\left(\frac{N\mu B}{k_B T}\right) - \frac{k_B T}{N\mu B}\right], \tag{1.1}$$

where N is the number of atoms in the cluster, k_B is the Boltzmann's constant, T is the temperature of the cluster and B the external magnetic field. Because the angular momentum of an isolated cluster is conserved, rotational temperature doesn't participate in the thermal fluctuations. For a superparamagnetic cluster, the magnetic moment per atom found by the experiment is a measure of the effective magnetic moment per atom μ_{eff}.

At high magnetic field and low temperature, $N\mu B/k_B T << 1$, and the equation reduces to,

$$\mu_{\text{eff}} \simeq \frac{N\mu^2 B}{3k_B T} \tag{1.2}$$

Thus the effective magnetic moment per atom of a superparamagnetic cluster is proportional to the square of the internal magnetic moment per atom μ and increases linearly with the applied magnetic field B. Finally, one measures the effective magnetic moment experimentally and uses the above equation to calculate the internal magnetic moment.

1.4 How theory can help?

Cluster science is a fascinating subject for theoretical studies. It is possible to apply the same quantum mechanical theoretical tools that are applied to studying molecules We could use the *ab initio* variational methods such as density functional theory under local density approximations to the exchange-correlation energy. One can apply gradient correction to this exchange-correlation. Recently, molecular dynamics based on the pseudo-potential method within the density functional theory has been developed. In Chapter 2, we would discuss these *ab initio* methods briefly.

We can use empirical potentials to study molecular dynamics of clusters. For example, the Lennard-Jones potentials can describe the dynamics of the inert gas clusters. Likewise, the Born- Mayer potentials for the short ranged Coulombic interaction or the exponential short range potential describe well the dynamics of alkali clusters. For other cluster, the approximations necessary are more subtle. For example embedded-atom potentials are of one kind of approximation, effective potentials have been used for metal clusters. If one can find a reliable form of the potential it would be easy to solve the simultaneous equations of motion and to explore at least some of the properties. However, this kind of semi-empirical potentials have their own limitations to describe certain properties.

Tight-binding molecular dynamics are also useful in describing the electronic properties and dynamics of the clusters. In this method, one can fit the tight-binding parameters form *ab initio* or experimental results in the size range where the results are available and then carry out tight-binding molecular dynamics to explore the cluster properties. This method is computationally much less expensive as compared with the ab initio methods. In the Chapter 2, we shall describe one such tight-binding molecular dynamics. This has been applied to study the copper clusters and discussed in the Chapter 3.

Chapter 2

Theoretical background of electronic structure calculations

2.1 Tight-Binding Molecular Dynamics

One of the simplest molecular dynamics extensively used is the empirical tight-binding molecular dynamics (TBMD). The method started as a spin-off from the linear combination of atomic orbitals (LCAO) method used by chemists to study molecules and eventually crystallized into a localized basis set of representation. This could be Wannier functions. Recently, the empiricity has been replaced by first-principles technique based on the more sophisticated localized representation arising out of the NMTO method proposed by Andersen and co-workers [28]. However, to our knowledge, a full molecular dynamics based on the NMTO is yet to be developed.

As compared to the *ab initio* methods, the parametrized tight-binding Hamiltonian reduces the computational cost dramatically and we can deal with really very large clusters. However, the main problem with the semi-empirical TB methods has always been the lack of transferability of its parameters. In this section we briefly describe the main ingredients of this TB method. We have used this technique to study very large Cu clusters, described in a following chapter.

The wave-function in this technique is expanded in a localized (tight-binding) basis :

$$|\Psi_k\rangle \;=\; \sum_i \; c^k_{i\nu} \; |\phi_{i\nu}\rangle$$

where i may label an atomic site and ν other quantum labels. If this is substituted into

the Schrödinger equation and premultiplied by $|\phi_{j\mu}\rangle$ to get :

$$\sum_i c_{i\nu}^k \left[\langle\phi_{j\mu}|H\phi_{i\nu}\rangle - \epsilon_k\langle\phi_{j\mu}|\phi_{i\nu}\rangle\right] = 0$$

These set of equations have a unique solution if the secular equation holds :

$$\det \parallel \langle\phi_{j\mu}|H|\phi_{i\nu}\rangle - \epsilon_k\langle\phi_{j\mu}|\phi_{i\nu}\rangle \parallel = 0$$

In the TBMD method, first we construct the TB Hamiltonian from which the electronic eigenstates and the corresponding eigenvalues are calculated. This includes efficient scaling scheme for the Slater-Koster (SK) TB matrix elements to ensure satisfactory transferability. In the subsequent step we calculate the total energy of the cluster and then use the Helmann-Feynmann theorem to calculate the forces acting on each atom of the cluster and then we use classical Newtonian equation of motion to find out the 'global' minima.

In this TB scheme the total energy E is written as a sum,

$$E = E_{el} + E_{rep} + E_{bond}. \tag{2.1}$$

E_{el} is the sum of the one-electron energies for the occupied states ϵ_k,

$$E_{el} = \sum_k f_k\epsilon_k, \tag{2.2}$$

where f_k is 0 or 1 according to whether the state labeled by k is occupied or not and the energy eigenvalues ϵ_k are calculated from the secular equation.

The single particle wave functions $|\Psi_k\rangle$ are cast as a linear combination of a minimum basis set, e/g/ for transition metal clusters $\nu = s, p_x, p_y, p_z, d_{xy}, d_{yz}, d_{zx}, d_{x^2-y^2}, d_{3z^2-r^2}$

The TB Hamiltonian H is constructed within the Slater-Koster scheme [29], where the diagonal matrix elements are taken to be configuration independent and the off-diagonal matrix elements are taken to have Slater-Koster type angular dependence with respect to the inter-atomic separation vector $\mathbf{r}$ and scaled exponentially with the inter-atomic separation r:

$$V_{\lambda,\lambda',\mu} = V_{\lambda,\lambda',\mu}(d)S(l,m,n)exp[-\alpha(r-d)], \tag{2.3}$$

where d is the equilibrium bond length of the material we are concern with in the bulk phase, $S(l, m, n)$ is the Slater-Koster type function of the direction cosines l, m, n of the separation vector $\mathbf{r}$ and α is an adjustable parameter ($= 2/d$) [30].

The Hamiltonian parameters are determined from the dimensionless universal parameters $\eta_{\lambda,\lambda',\mu}$ [31],

$$V_{\lambda,\lambda',\mu}(d) = \eta_{\lambda,\lambda',\mu}\left(\frac{\hbar^2 r_d^{\tau}}{m d^{\tau+2}}\right), \tag{2.4}$$

Where r_d is characteristic length for the transition metal and the parameter $\tau = 0$ for $s-s$, $s-p$ and $p-p$ interactions, $\tau = 3/2$ for $s-d$ and $p-d$ interactions and $\tau = 3$ for $d-d$ interaction.

The repulsive energy E_{rep} is described by a sum of short-ranged repulsive pair potentials, ϕ_{ij}, which scaled exponentially with inter-atomic distance,

$$\begin{aligned} E_{rep} &= \sum_i \sum_{j(>i)} \phi_{ij}(r_{ij}) \\ &= \sum_i \sum_{j(>i)} \phi_0 exp[-\beta(r_{ij} - d)], \end{aligned} \tag{2.5}$$

where r_{ij} is the separation between the atom i and j and $\beta(= 4\alpha)$ is a parameter. E_{rep} contains ion-ion repulsive interaction and correction to the double counting of the electron-electron repulsion present in E_{el}. The value of ϕ_0 is fitted to reproduce the correct experimental bond length of the dimer.

The first two terms of the total energy are not sufficient to exactly reproduce cohesive energies of dimers through bulk structures. Tomaňek and Schluter [32] introduced a coordination dependent correction term, E_{bond}, to the total energy, which does not contribute to the force, it is added to the total energy after the relaxation has been achieved. However, for the metal clusters, this correction term is significant in distinguishing various isomers for a given cluster [30].

$$E_{bond} = -n\left[a\left(\frac{n_b}{n}\right)^2 + b\left(\frac{n_b}{n}\right) + c\right], \tag{2.6}$$

where n and n_b are the number of atoms and total number of bonds of the cluster, respectively. Number of bonds n_b are evaluated by summing over all bonds according to

a cut-off distance r_c and bond length

$$n_b = \sum_i \left[exp\left(\frac{r_{ij} - r_c}{\triangle} \right) + 1 \right]^{-1}. \tag{2.7}$$

The parameters a, b and c in the equation 2.6 are then calculated by fitting the coordination dependent term, E_{bond}, to the *ab initio* results for three small clusters of different sizes according to the following equation

$$E_{bond} = E_{ab\ \ initio} - E_{el} - E_{rep}. \tag{2.8}$$

Thus we have four parameters ϕ_0, a, b, and c in this TB model. These parameters are once calculated for small clusters to reproduce known results (whatever experimental or theoretical) and then kept fixed for other arbitrary size cluster.

In molecular dynamics scheme the trajectories $\{R_j(t)\}$ of the ions are determined by the potential energy surface $E[\{R_j(t)\}]$ corresponding to the total energy of the electronic system. The force acting on the i-th ion is thus given by,

$$\begin{aligned} \mathbf{F}_i &= -\nabla_{R_i} E[\{R_j\}] \\ &= -\nabla_{R_i} \left[\sum_k \langle \Psi_k | H | \Psi_k \rangle + E_{rep} \right] \end{aligned} \tag{2.9}$$

This equation can be further simplified by making use of the Hellmann-Feynman [33] theorem:

$$\mathbf{F}_i = -\sum_k \langle \Psi_k \, | \nabla_{R_i} H | \, \Psi_k \rangle - \nabla_{R_i}\ E_{rep}. \tag{2.10}$$

The second term in the above equation is the short-ranged repulsive force. We should note that Pulay correction term does not play any role in any semi-empirical TBMD. Pulay terms appear when the basis set itself changes as we move the ions. In the TBMD we work with a *fixed* basis set. Moreover, in the TBMD we directly compute the derivative of the TB Hamiltonian matrix element and the basis wave functions never appear explicitly, rather they are implicitly contained in the fitted matrix entries.

The motion of the ions follow a classical behaviour and is governed by the Newton's law :

$$m \frac{d^2 \mathbf{R}_i}{dt^2} = \mathbf{F}_i, \tag{2.11}$$

where m is the atomic mass.

For numerical simulation of Newtonian dynamics, we use the velocity Verlet molecular dynamics method [34] for updating the atomic coordinates, which is given by,

$$\mathbf{R}_i(t+\delta t) = \mathbf{R}_i(t) + \mathbf{V}_i(t)\delta t + \frac{1}{2m}\mathbf{F}_i(t)(\delta t)^2, \tag{2.12}$$

where the velocity $\mathbf{V}_i$ of the ith atom at $t+\delta t$ is calculated from $\mathbf{F}_i$ at t and $t+\delta t$ as

$$\mathbf{V}_i(t+\delta t) = \mathbf{V}_i(t) + \frac{1}{2m}[\mathbf{F}_i(t) + \mathbf{F}_i(t+\delta t)]\delta t. \tag{2.13}$$

At this stage one carry out either dissipative dynamics or free dynamics with feedback [35]. The reason for this is as follows : for numerical integration of Newton's equations we have to choose a *finite* time-step δt. Ideally this should be as small as possible, but that would require an excessively long time for locating the global minimum. However, a large choice of δt leads to unphysical heating up of the system, leading to instability. Dissipative dynamics has been suggested as a way of overcoming this. We add a small extra friction term carefully $\mathbf{F} \Rightarrow \mathbf{F} - \gamma m\dot{\mathbf{R}}$ [30]. In the present calculation $\gamma m = 0.32$ amu/psec, and the time step δt is taken to be 1 fsec and the total time for molecular dynamics simulation is $\sim$ 100 - 200 psec, depending upon the cluster size and initial cluster configuration with the several annealing schedule. Methfessel and Schilfgaarde [35] have also used an alternative technique of free dynamics with feedback to overcome the above difficulty.

The results of the molecular dynamics may depend sensitively on the starting configuration chosen. The final equilibrium configurations often correspond to local minima of the total energy surface and are metastable states. For the smaller clusters simulated annealing can lead to the global minimum. We have found the global minimum configurations of the smaller clusters by the simulated annealing technique. However, this is often not the case for the larger clusters. Recently more sophisticated techniques like the genetic algorithm has been proposed [36, 37, 38, 39].

2.2 The many-body problem

One of the main problems with empirical molecular dynamics techniques is that the parameters are, in general, *not* transferable from one environment to another. We have no

a priori knowledge of how to modify them in different situations. We therefore, require to develop, first principles technique methods of actually *deriving* a Hamiltonian for electrons and ions in a full many-body system.

The Schrödinger equation is the starting point of any problem in the electronic structure of matter. The molecules, clusters or solids comprise of two kinds of electrons : *valence electrons* which contribute to the chemical bonding and *core electrons* which are tightly bound to the closed shell of the ions and which scarcely influence the properties of materials. Now let us first set up the exact Hamiltonian for a system of $\mathcal{N}$ atoms with w valence electrons each:

$$\mathcal{H} = \sum_{i=1}^{\mathcal{N}} \frac{\mathbf{P}_i^2}{2M_i} + \sum_{k}^{N} \frac{\mathbf{p}_k^2}{2m_k} + \sum_{i,i'(>i)}^{\mathcal{N}} \frac{(we)^2}{|\mathbf{R}_i - \mathbf{R}_{i'}|} - \sum_{i=1}^{\mathcal{N}} \sum_{k=1}^{N} \frac{we^2}{|\mathbf{R}_i - \mathbf{r}_k|} + \sum_{k,k'(>k)}^{N} \frac{e^2}{|\mathbf{r}_k - \mathbf{r}_{k'}|}$$

where i denote the ions and k denote the electrons. The above Hamiltonian is for $\mathcal{N} + N$ interacting particles, where $N = w\mathcal{N}$ is the total number of valence electrons in the system.

Now the mass of the ion is much larger than that of an electron ($M >> m$), so that the frequency of the vibration of electrons is much larger than that of the ions ($\omega_e >> \omega_{\text{ion}}$). Therefore, the characteristic time scale associated with ionic is much larger than that of the electrons ($\tau_{\text{ion}} >> \tau_e$). We may then assume that in the short time τ_e during which electrons change their state, the ions are *fixed*. This is the Born-Oppenheimer or Adiabatic approximation. The wave function may then be written in a separable form $\Phi(\{\mathbf{r}_k\})\Psi(\{\mathbf{R_i}\})$ and the Schrödinger equation becomes :

$$\left(\sum_{k}^{N} \frac{\mathbf{p}_k^2}{2m_k} + \sum_{i=1}^{\mathcal{N}} \sum_{k=1}^{N} \frac{we^2}{|\mathbf{R}_i - \mathbf{r}_k|} + \sum_{k,k'(>k)}^{N} \frac{e^2}{|\mathbf{r}_k - \mathbf{r}_{k'}|} \right) \Phi(\{\mathbf{r_k}\}) \;=\; E(\{\mathbf{R}_i\})\Phi(\{\mathbf{r_k}\})$$

Once the electronic part is solved for a fixed position of ions, the ionic part may now be obtained from :

$$\left(\sum_{i=1}^{\mathcal{N}} \frac{\mathbf{P}_i^2}{2M_i} + \sum_{i,i'(>i)}^{\mathcal{N}} \frac{(we)^2}{|\mathbf{R}_i - \mathbf{R}_{i'}|} + E(\{\mathbf{R}_i\}) \right) \Psi(\{\mathbf{R}_i\}) \;=\; E_{tot}\Psi(\{\mathbf{R}_i\})$$

The electronic contribution gives rise to an effective attractive potential between ions which leads to bonding. The effective potential in which the ions move is then :

$$V_{NN}^{eff} = \sum_{i=1}^{\mathcal{N}} \sum_{k=1}^{N} \frac{we^2}{|\mathbf{R}_i - \mathbf{r}_k|} + E(\{\mathbf{R}_i\}$$

2.2.1 The Hartree-Fock Approximation

The difficulty with the solution of the reduced electronic problem lies in the interaction between the individual electrons. This electron-electron interaction couples the electronic degrees of freedom, which makes the problem an impossible task to solve. However, in the absence of this electron-electron interaction, the many-body problem would decouple into one-body problem, i.e. an electron moving in a given potential. We can rewrite the electronic Hamiltonian as:

$$\begin{aligned} \mathcal{H} &= -\sum_k \frac{\hbar^2}{2m_k}\nabla_k^2 + \sum_k V(\mathbf{r}_k) + \sum_{kk'} \frac{e^2}{|\mathbf{r}_k - \mathbf{r}_{k'}|} \\ &= \sum_k H_k + \sum_{k,k'} H_{kk'}. \end{aligned} \tag{2.14}$$

In the above equation the first two terms are single particle operator. Now in case if we neglect the relatively strong electron-electron interaction then the solution would be simple. In that case the wave function Φ of the corresponding Schrödinger equation $\sum_k H_k\Phi = E\Phi$ can be written as,

$$\Phi(\mathbf{r}_1...\mathbf{r}_k...\mathbf{r}_N) = \varphi_1(\mathbf{r}_1)...\varphi_k(\mathbf{r}_k)...\varphi_N(\mathbf{r}_N). \tag{2.15}$$

With $E = \sum_k E_k$, the Schrödinger equation reduces to sum of one-electron equation, $\sum_k H_k\varphi_k(\mathbf{r}_k) = \sum_k E_k\varphi_k(\mathbf{r}_k)$. However, the rather strong electron-electron interaction, i.e. the two-body term in the Hamiltonian $H_{kk'}$ prevents this possibility. In the next step, we therefore insert the function $\Phi(\mathbf{r}_1...\mathbf{r}_k...\mathbf{r}_N)$ into the Schrödinger equation $\mathcal{H}\Phi = E\Phi$ with $\mathcal{H} = \sum_k H_k + \sum_{kk'} H_{kk'}$ and calculate the expectation value of energy, $E = \langle\Phi|\mathcal{H}|\Phi\rangle$, which has $\langle\varphi_k|H_k|\varphi_k\rangle$ and $\langle\varphi_{kk'}|H_{kk'}|\varphi_{kk'}\rangle$ matrix elements and we assume that the φ_k are normalized then,

$$E = \langle\Phi|\mathcal{H}|\Phi\rangle = \sum_k \langle\varphi_k|H_k|\varphi_k\rangle + \frac{e^2}{2}\sum_{kk'} \left\langle \varphi_k\varphi_{k'} \left| \frac{1}{|\mathbf{r}_k - \mathbf{r}_{k'}|} \right| \varphi_k\varphi_{k'} \right\rangle. \tag{2.16}$$

This is the expectation value of E for an arbitrary φ_k. Now one could apply variational principle to find out the best set of φ_k functions for the ground state which minimize the energy E, i,e,

$$\delta\left[E - \sum_k E_k\left(\langle\varphi_k|\varphi_{k'}\rangle - 1\right)\right] = 0. \tag{2.17}$$

Then we get,

$$\langle\delta\varphi_j|H_j|\varphi_j\rangle + \sum_{k(>j)}\left\langle\delta\varphi_j\varphi_k\left|\frac{e^2}{|\mathbf{r}_k - \mathbf{r}_j|}\right|\varphi_j\varphi_k\right\rangle - E_j\langle\delta\varphi_j|\varphi_j\rangle = 0 \tag{2.18}$$

As the above equation is valid for any variation $\langle\delta\varphi_j|$, therefore φ_j satisfy the following equation:

$$\left[-\frac{\hbar^2}{2m}\nabla^2 + V(\mathbf{r}) + \sum_{k(>j)}\int\frac{|\varphi_k(\mathbf{r}'|^2}{\mathbf{r} - \mathbf{r}'|}\delta\mathbf{r}'\right]\varphi_j(\mathbf{r}) = E_j\varphi_j(\mathbf{r}) \tag{2.19}$$

This is a single particle Schrödinger equation which is called the Hartree equation. This describes an electron in an ionic potential field $V(\mathbf{r})$ and interacting with all other electrons via and average distribution of electron density. However, separating one electron out of all and treating all other electrons as a smooth charge density is a crude approximation to make. In the next step we therefore extend the expansion of $\Phi(\mathbf{r}_1...\mathbf{r}_k...\mathbf{r}_N)$ by applying the Pauli principle and the indistinguability of quantum particles. There are $N!$ possible ways to distribute N electrons at the positions $\mathbf{r}_1...\mathbf{r}_k...\mathbf{r}_N$ and due to indistinguability of electrons all those possibilities are equally likely. So we use a sum of $N!$ such terms, which includes all possible electron permutations. Moreover, to antisymmetries the total wave function we introduce plus or minus sign with all such individual terms as the wave function changes sign due to the interchange of any two electrons. Therefore, the form of Φ can be better approximated by using Slater determinant:

$$\Phi = \frac{1}{\sqrt{N!}}\begin{vmatrix} \varphi_1(\mathbf{q}_1) & \cdots & \cdots & \cdots & \varphi_N(\mathbf{q}_1) \\ \vdots & & & & \vdots \\ \vdots & & & & \vdots \\ \vdots & & & & \vdots \\ \varphi_1(\mathbf{q}_N) & \cdots & \cdots & \cdots & \varphi_N(\mathbf{q}_N) \end{vmatrix}, \tag{2.20}$$

where $\mathbf{q}$ are composite index for electronic coordinates and spin. Here we see that if the two electrons are interchanged, two columns of the determinant are interchanged and Φ

changes sign and if two electrons have same coordinate, two columns are same and the wave function Φ vanishes.

With this form of wave function Φ, we again calculate the expectation value of energy E as,

$$\begin{aligned} E &= \langle\Psi|\mathcal{H}|\Psi\rangle \\ &= \sum_k \int \varphi_k^*(\mathbf{q}_1) H_k \varphi_k(\mathbf{q}_1) d\tau + \frac{e^2}{2}\sum_{kk'}\int \frac{|\phi_k(\mathbf{q}_1)|^2 |\varphi_{k'}(\mathbf{q}_2)|^2}{|\mathbf{r}_1-\mathbf{r}_2|} d\tau_1 d\tau_2 \\ &- \frac{e^2}{2}\sum_{kk'}\int \frac{\varphi_k^*(\mathbf{q}_1)\varphi_k(\mathbf{q}_2)\varphi_{k'}^*(\mathbf{q}_2)\varphi_{k'}(\mathbf{q}_1)}{|\mathbf{r}_1-\mathbf{r}_2|} d\tau_1 d\tau_2. \end{aligned} \tag{2.21}$$

In comparison with the Hartree equation now we have an extra term. This term has no classical analogue and known as *exchange interaction*. Now following the similar method used earlier we obtain,

$$\begin{aligned} &\left[\frac{\hbar^2}{2m}\nabla_1^2 + V(\mathbf{r}_1) + e^2\sum_{k'}\int \frac{|\varphi_{k'}(\mathbf{q}_2)|^2}{|\mathbf{r}_1-\mathbf{r}_2|} d\tau_2\right]\varphi_k(\mathbf{q}_1) - e^2\sum_{k'}\int \frac{\varphi_{k'}^*(\mathbf{q}_2)\varphi_k(\mathbf{q}_2)}{|\mathbf{r}_1-\mathbf{r}_2|}\mathrm{d}\tau_2\varphi_{k'}(\mathbf{q}_1) \\ &= \sum_{k'}\lambda_{kk'}\varphi_{k'}(\mathbf{q}_1) \end{aligned} \tag{2.22}$$

This equation is known as the Hartree-Fock equation.

2.3 Density functional theory

The pioneering work of Thomas and Fermi attempted to describe the many-body interacting electronic problem in terms of the charge density *alone*. The Thomas-Fermi (TF) approximation considers interacting electrons moving in an external potential $v(r)$ and provided a one-to-one implicit relation between $v(r)$ and the electron density distribution $n(r)$:

$$\begin{aligned} n(r) &= \gamma[\mu - v_{eff}(r)]^{3/2}, \\ \text{where, } \gamma &= \frac{1}{3\pi^2}\left(\frac{2m}{\hbar^2}\right)^{3/2} \text{ and } \quad v_{eff} = v(r) + \int \frac{n(r')}{|r-r'|} dr. \end{aligned} \tag{2.23}$$

Here μ is a r-independent chemical potential. The TF is expressed in terms of electron density $n(r)$ and the Schrödinger equation is expressed in terms of wave function

$\Psi(r_1, ..., r_N)$ and there was no established clear and strict connection between them. This is quite useful in describing some qualitative features like total energies of atoms, however, it do not lead to any chemical bonding, which is the question of chemistry and material sciences.

2.3.1 The Hohenberg-Kohn formulation

The Hohenberg-Kohn theorem [40] describes the density $n(r)$ as the basic variable. This theorem states that the ground-state density $n(r)$ of a bound system of interacting electrons in an external potential $v(r)$ determines this potential uniquely (up to an uninteresting additive term).

Consider the ground states of two N-electron systems characterised by the two external potentials (differing by more than an additive constants) $v_1(r)$ and $v_2(r)$ with corresponding Hamiltonian:

$$\begin{aligned} \mathcal{H}_1 &= T + U + \sum_i v_i(r_i); \quad \mathcal{H}_2 = T + U + \sum_i v_2(r_i) \\ \text{where, T} &= -\frac{1}{2}\sum_i^N \nabla_i^2 \quad \text{and} \quad U = \frac{1}{2}\sum_{i\neq j} \frac{1}{|\mathbf{r}_i - \mathbf{r}_j|}, \end{aligned} \tag{2.24}$$

with the corresponding Schrödinger equation, $\mathcal{H}_1\Psi_1 = E_1\Psi_1$ and $\mathcal{H}_2\Psi_2 = E_2\Psi_2$ and we assume that the two wave function Ψ_1 and Ψ_2 yield that same density as,

$$n(r_i) = N \int \Psi^*(r_1, r_2, ..., r_N)\Psi(r_1, r_2, ..., r_N) dr_2 dr_3 .... dr_N. \tag{2.25}$$

Now,

$$\begin{aligned} E_1 &= \langle \Psi_1 | \mathcal{H}_1 | \Psi_1 \rangle \\ &< \langle \Psi_2 | \mathcal{H}_1 | \Psi_2 \rangle \\ &= \langle \Psi_2 | \mathcal{H}_2 | \Psi_2 \rangle + \langle \Psi_2 | \mathcal{H}_1 - \mathcal{H}_2 | \Psi_2 \rangle \\ &= E_2 + \int dr n(r) \left[v_1(r) - v_2(r) \right]. \end{aligned} \tag{2.26}$$

Now, similarly one could show that,

$$E_2 \leq E_1 \int dr n(r) \left[v_1(r) - v_2(r) \right]. \tag{2.27}$$

Summation of the above two inequalities leads to the contradiction

$$E_1 + E_2 < E_2 + E_1 \tag{2.28}$$

Hence the assumption of identical density arising from the two different external potentials is wrong. Thus a given $n(\mathbf{r})$ can only correspond to only one $v(\mathbf{r})$ and since $v(r)$ is fixed, the Hamiltonian and hence the wave functions are also fixed by density $n(r)$. Since the wave function is a functional of density, the energy functional $E_v[n]$ for a given external potential $v(r)$ is a unique functional of density. Later a more general proof of the Hohenberg-Kohn theorem, independent of ground-state degeneracy was given by Levy.

2.3.2 The Hohenberg-Kohn variational theorem

Since Ψ is a functional of density $n(\mathbf{r})$, the kinetic and interaction energies, therefore, also a functional of $n(\mathbf{r})$. Now an universanal functional can be defined,

$$F[n] = \langle \Psi | T + U | \Psi \rangle \,, \tag{2.29}$$

which is valid for any number of any number of particles and any external potential. Now, for a given external potential $v(\mathbf{r})$ the energy functional is,

$$E_v[n] = \int v(\mathbf{r}) n(\mathbf{r}) d\mathbf{r} + F[n]. \tag{2.30}$$

The Hohenberg-Kohn variational theorem states that for every trial density function $n_{tr}(\mathbf{r})$ that satisfies the conditions, $\int n_{tr}(\mathbf{r}) d\mathbf{r} = N$ and $\mathrm{n_{tr}}(\mathbf{r}) \geq 0$ for all $\mathbf{r}$, the following inequality holds: $E_0 \leq E_v[n_{tr}]$. Since $E_0 = E_v[n_0]$, where n_0 is the true ground-state electron density, the true ground-state electron density minimizes the energy functional $E_v[n_{tr}]$, just as the true normalized ground-state invention minimizes the eigenvalue in a Schrödinger equation.

Consider that n_{tr} satisfies the above states conditions, $\int n_{tr}(\mathbf{r}) d\mathbf{r} = N$ and $\mathrm{n_{tr}}(\mathbf{r}) \geq 0$ for all $\mathbf{r}$. The Hohenberg-Kohn theorem states that n_{tr} uniquely determines the external potential v_{tr} and this in turn determines the trial wave function Ψ_{tr}, that corresponds to n_{tr}. Now the energy corresponding to this wave function Ψ_{tr} is,

$$E \;=\; \langle \Psi_{tr} \, | \mathcal{H} \, | \Psi_{tr} \, \rangle$$

$$\begin{aligned} &= \left\langle \Psi_{tr} \left| T + U + \sum_i v_i(\mathbf{r}) \right| \Psi_{tr} \right\rangle \\ &\geq E_0 = E_v[n_0] \end{aligned} \tag{2.31}$$

Since the kinetic and interaction energies are functionals of the electron density and using the ground state wave function Ψ_0, we have,

$$\begin{aligned} T[n_{tr}] + U[n_{tr}] + \int n_{tr} v(\mathbf{r}) d\mathbf{r} &\geq E_v[n_0] \\ E_v[n_{tr}] &\geq E_v[n_0]. \end{aligned} \tag{2.32}$$

This proves that any trial electron density can not give rise a lower ground-state energy than the true ground-state electron density.

2.3.3 The Kohn-Sham equation

If we know the ground-state electron density $n_0(\mathbf{r})$, the Hohenberg-Kohn theorem tells us that in principle it is possible to calculate the ground-state properties from n_0 without having to find the wave function. However, Hohenberg-Kohn theorem does not refer how to calculate E_0 from n_0 or how to find n_0 without first finding the wave function.

Consider a reference system of N non interacting electrons that each experience the same external potential $v_s(\mathbf{r}_i)$, where $v_s(\mathbf{r}_i)$ is such to make the density of this reference system is equal to the exact ground state density of the real system, $n_0(\mathbf{r}) = n_s(\mathbf{r})$. The Hamiltonian of the reference system is,

$$\begin{aligned} H &= -\frac{1}{2} \sum_{i=1}^{N} \nabla_i^2 + \sum_{i=1}^{N} v_s(\mathbf{r}_i) \\ &= \sum_{i=1}^{N} h_i^{KS}, \end{aligned} \tag{2.33}$$

where h_i^{KS} is the one electron Kohn-Sham Hamiltonian, $h_i^{KS} = -\frac{1}{2}\nabla_i^2 + v_s(\mathbf{r}_i)$. The ground state wave function $\Psi_{s,0}$ of the reference system can be written using Slater determinant,

$$\Psi_{s,0} = \frac{1}{\sqrt{N!}} \det(\psi_1 \psi_2 .... \psi_N), \tag{2.34}$$

which satisfies $h_i^{KS} \psi_i = \epsilon_i \psi_i$.

Now let define a term ΔT as,

$$\Delta T[n] = T[n] - T_s[n], \tag{2.35}$$

which is the difference in the kinetic energy between the real and the reference system of non interacting electrons with density equal to the real system. Similarly, we define,

$$\Delta U[n] = U[n] - \frac{1}{2}\int\int \frac{n(\mathbf{r}_1)n(\mathbf{r}_2)}{|\mathbf{r}_1 - \mathbf{r}_2|} d\mathbf{r}_1 d\mathbf{r}_2. \tag{2.36}$$

Therefore, the energy functional becomes,

$$E_v[n] = \int n(\mathbf{r})v(\mathbf{r})d\mathbf{r} + T_s[n] + \frac{1}{2}\int\int \frac{n(\mathbf{r}_1)n(\mathbf{r}_2)}{|\mathbf{r}_1 - \mathbf{r}_2|} d\mathbf{r}_1 d\mathbf{r}_2 + \Delta T[n] + \Delta U[n] \tag{2.37}$$

Here the functionals $\Delta T[n]$ and $\Delta U[n]$ are unknown and together define the *exchange-correlation* energy functional:

$$E_{xc}[n] = \Delta T[n] + \Delta U[n]. \tag{2.38}$$

Therefore, the energy functional has the form,

$$E_0 = E_v[n] = \int n(\mathbf{r})v(\mathbf{r})d\mathbf{r} + T_s[n] + \frac{1}{2}\int\int \frac{n(\mathbf{r}_1)n(\mathbf{r}_2)}{|\mathbf{r}_1 - \mathbf{r}_2|} d\mathbf{r}_1 d\mathbf{r}_2 + E_{xc}[n] \tag{2.39}$$

The first three terms are easy to calculate if the electron density is known and have the main contribution to the ground state energy, whereas the last term, the exchange-correlation is relatively small and is not easy to calculate accurately. Now, before one could evaluate the energy functional $E_v[n]$, we need to calculate the ground state density first.

The electron density of an N-particle system whose wave function is given by, Equation 1.25 is therefore,

$$n_s = \sum_{i=1}^{N} |\psi_i|^2, \tag{2.40}$$

which we have assumed to be equal to the ground state density of the real system, $n_0 = n_s$.

The kinetic energy functional of the reference system can be expressed as,

$$T_s[n] = -\frac{1}{2}\left\langle \Psi_s \left| \sum_i \nabla_i^2 \right| \Psi_s \right\rangle = \sum_{i=1}^{N} \left\langle \psi_i \left| -\frac{1}{2}\nabla_i^2 \right| \psi_i \right\rangle. \tag{2.41}$$

Therefore,

$$E_0 = \int n(\mathbf{r})v(\mathbf{r})d\mathbf{r} - \frac{1}{2}\sum_{i=1}^{N}\left\langle \psi_i \left| \nabla_i^2 \right| \psi_i \right\rangle + \frac{1}{2}\int\int \frac{n(\mathbf{r}_1)n(\mathbf{r}_2)}{|\mathbf{r}_1 - \mathbf{r}_2|}d\mathbf{r}_1 d\mathbf{r}_2 + E_{xc}[n]. \tag{2.42}$$

Now, the Hohenberg-Kohn variational principle tells that we could find the ground state energy by varying electron density constraint to $\int n(\mathbf{r})d\mathbf{r} = N$ so as to minimize the energy functional $E_v[n]$. Equivalently, instead of varying electron density n, we can vary the Kohn-Sham orbitals ψ_i. Now it can readily be shown that the wave function ψ_i, which minimizes the above expression satisfy,

$$\left[-\frac{1}{2}\nabla^2 + v(\mathbf{r}) + \int \frac{n(\mathbf{r}')}{|\mathbf{r} - \mathbf{r}'|}d\mathbf{r}' + v_{xc}(\mathbf{r})\right]\psi_i = \epsilon_i \psi_i \tag{2.43}$$

This is know as Kohn-Sham equation [41]. The exchange-correlation potential v_{xc} is found as the functional derivative of the exchange-correlation energy:

$$v_{xc} = \frac{\delta E_{xc}[n(\mathbf{r})]}{\delta n(\mathbf{r})} \tag{2.44}$$

2.3.4 Exchange-correlation energy

While the Kohn-Sham equation exactly incorporate the kinetic energy functional $T_s[n]$, the exchange-correlation functional $E_{xc}[n]$ is still unknown. The search for an accurate $E_{xc}[n]$ has encountered tremendous difficulty and is the greatest challenge in the density functional theory. The exchange-correlation energy is given by,

$$E_{xc} = \Delta T[n] + \Delta U[n], \text{where,} \quad \mathrm{v_{xc}} = \frac{\delta \mathrm{E_{xc}[n(\mathbf{r})]}}{\delta \mathrm{n}(\mathbf{r})} \tag{2.45}$$

This exchange-correlation energy contains — (i) Kinetic correlation energy, which is the difference in the kinetic energy functional between the real and the noninteracting reference system. (ii) The exchange energy, which arises from the antisymmetric requirement. (iii) Coulombic correlation energy, which arises from the inter-electronic repulsion and (iv) A self-interaction correction.

2.3.5 The local density approximation (LDA)

Hohenberg and Kohn showed that if the density $n(\mathbf{r})$ varies extremely slow with $\mathbf{r}$ then the $E_{xc}[n]$ is accurately given by,

$$E_{xc}^{LDA}[n] = \int n(\mathbf{r})\mathcal{E}_{xc}^{LDA}(n(\mathbf{r}))d\mathbf{r}, \tag{2.46}$$

where $\mathcal{E}_{xc}^{LDA}[n]$ is the exchange plus correlation energy per electron in a homogeneous electron gas with electron density n. The exchange part reads as $\mathcal{E}_{x}^{LDA}[n] = -3/4\pi(3\pi^2 n)^1/3$. For the correlation part representations given by Perdew and Wang [42] and, previously by Perdew and Zunger [43] can be used. Both are parameterization of Ceperly and Alder's exact results for the uniform gas [44]. One can also use the earlier prescriptions by Hedin and Lundquist [45] and by Wigner [46]. These nonrelativistic LDA exchange-correlation functionals may be replaced with relativistic corrections to the exchange part as given by MacDonald and Vosko [47]. The functional derivative of E_{xc}^{LDA} gives the exchange-correlation potential within LDA,

$$\begin{aligned} v_{xc}^{LDA} &= \frac{\delta E_{xc}^{LDA}}{\delta n} \\ &= \mathcal{E}_{xc}\left(n(\mathbf{r})\right) + n(\mathbf{r})\frac{\partial \mathcal{E}_{xc}(n)}{\partial n}. \end{aligned} \tag{2.47}$$

2.3.6 The generalized gradient approximation (GGA)

In a generalized gradient approximation (GGA) the functional depends on the density and its gradient,

$$E_{xc}^{GGA}[n] = \int n(\mathbf{r})\mathcal{E}_{xc}^{GGA}(n(\mathbf{r}), |\nabla n(\mathbf{r})|)d\mathbf{r}. \tag{2.48}$$

Now one can use the GGA functionals by Perdew and Wang [42], by Perdew, Burke and Ernzerhof (PBE) [48] and Becke's formula [49] for the exchange part combined with Perdew's 1986 formula for correlation [50]. Substituting for the latter formula of Lee, Yang and Parr [51] provides the so-called BLYP GGA. The exchange-correlation potential in Cartesian coordinates is given by,

$$v_x c^{GGA}[n, \mathbf{r}] = \left[\frac{\partial}{\partial n} - \sum_{i=1}^{3} \nabla_i \frac{\partial}{\partial \nabla_i n}\right] n(\mathbf{r})\mathbf{E}_{xc}^{GGA}(n(\mathbf{r}), |\nabla n(\mathbf{r})|), \tag{2.49}$$

and depends on the first and second radial derivatives of the density. It is an open issue whether to perform one of these GGAs over another. Dependent on the application, they may yield somewhat differing result. However, the actual choice among these GGAs is usually less important than the difference between the LDA and the GGA themselves.

2.4 The Projector-Augmented-Wave formalism

The most widely used electronic structure methods can be divided into two classes. First one is the linear method [52] developed from the augmented-plane-wave method [29, 54] and Koringa-Kohn-Rostocar method [55, 56] and the second one is the norm-conserving pseudopotentials developed by Hamann, Schlüter and Chiang [57]. In that scheme, inside some core radius, the all electron (AE) wave function is replaced by a soft nodeless pseudo (PS) wave function, with the restriction to the PS wave function that within the chosen core radius the norm of the PS wave function have to be the same with the AE wave function and outside the core radius both the wave functions are just identical. However, the charge distribution and moments of AE wave function are well reproduced by the PS wave function only when the core radius is taken around the outer most maxima of AE wave function. Therefore, elements with strongly localized orbitals pseudopotentials require a large plane wave basis set. This was improved by Vanderbilt [58], where the norm-conservation constraint was relaxed and a localized atom centered augmentation charges were introduced to make up the charge deficit. But the success is partly hampered by rather difficult construction of the pseudopotential. Later Blöchl [59] has developed the projector-augmented- wave (PAW) method, which combines the linear augmented plane wave method with the plane wave pseudopotential approach, which finally turns computationally elegant, transferable and accurate method for electronic structure calculation. Further Kresse and Joubert [60] modified this PAW method and implemented in their existing Veina ab-initio pseudopotential package (VASP). Here in this section we will discuss briefly the idea of the method.

2.4.1 Wave functions

The exact Kohn-Sham density functional is given by,

$$E \;=\; \sum_n f_n \langle \Psi_n | -\frac{1}{2}\nabla^2 | \Psi_n \rangle \;+\; E_H[n+n_Z] \;+\; E_{xc}[n], \tag{2.50}$$

where $E_H[n+n_Z]$ is the hartree energy of the electronic charge density n and the point charge densities of the nuclei n_Z, $E_{xc}[n]$ is the electronic exchange-correlation energy and f_n are the orbital occupation number. $|\Psi_n\rangle$ is the all-electron wave function. This physically relevant wave functions $|\Psi_n\rangle$ in the Hilbert space exhibit strong oscillations and make numerical treatment difficult. Transformation of this wave functions $|\Psi_n\rangle$ into a new pseudo wave functions $|\tilde{\Psi}_n\rangle$ in the PS Hilbert space,

$$|\Psi_n\rangle \;=\; \tau |\tilde{\Psi}_n\rangle, \tag{2.51}$$

within the augmentation region Ω_R, then makes PS wave function $|\tilde{\Psi}_n\rangle$ computationally convenient.

Let us now choose a PS partial wave function $|\tilde{\phi}_i\rangle$, which is identical to the corresponding AE partial waves $|\psi_i\rangle$ outside the augmentation region and form a complete set within the augmentation region Ω_R. Within the augmentation region every PS wave function can be expanded into PS partial waves,

$$|\tilde{\Psi}\rangle \;=\; \sum_i c_i |\tilde{\phi}_i\rangle, \tag{2.52}$$

where the coefficients c_i are scalar products,

$$c_i \;=\; \langle \tilde{p}_i | \tilde{\Psi}_n \rangle, \tag{2.53}$$

with some fixed function $\langle \tilde{p}_i|$ of the PS wave function, which is called the projector function. By using the linear transformation [59],

$$\tau \;=\; 1 + \sum_i (|\phi_i\rangle - |\tilde{\phi}_i\rangle)\langle \tilde{p}_i|, \tag{2.54}$$

the corresponding AE wave function $|\Psi_n\rangle$ in the Eq. 1.2 is then,

$$|\Psi_n\rangle \;=\; |\tilde{\Psi}_n\rangle \;+\; \sum_i (|\psi_i\rangle - |\tilde{\psi}_i\rangle)\langle \tilde{p}_i | \tilde{\Psi}_n \rangle, \tag{2.55}$$

where i refers to the atomic site $\mathbf{R}$, the angular momentum quantum numbers $L = l, m$ and an additional index k for the reference energy ϵ_{kl} and, with $\tilde{p}_i$ being the projector functions, which within the augmentation region Ω_R satisfy the condition,

$$\langle \tilde{p}_i | \tilde{\phi}_j \rangle \;=\; \delta_{ij}. \tag{2.56}$$

The AE charge density at a given point $\mathbf{r}$ is the expectation value of the real-space projector operator $|r\rangle\langle r|$ and hence given by,

$$n(\mathbf{r}) \;=\; \tilde{n}(\mathbf{r}) + n^1(\mathbf{r}) - \tilde{n}^1(\mathbf{r}), \tag{2.57}$$

where $\tilde{n}(\mathbf{r})$ is the soft PS charge density calculated from the PS wave function

$$\tilde{n}(\mathbf{r}) \;=\; \sum_n f_n \langle \tilde{\Psi}_n | \mathbf{r} \rangle \langle \mathbf{r} | \tilde{\Psi}_n | \mathbf{r} \rangle, \tag{2.58}$$

and onsite charge densities are defined as,

$$n^1(\mathbf{r}) \;=\; \sum_{ij} \rho_{ij} \langle \phi_i | \mathbf{r} \rangle \langle \mathbf{r} | \phi_j \rangle, \tag{2.59}$$

and,

$$\tilde{n}^1(\mathbf{r}) \;=\; \sum_{ij} \rho_{ij} \langle \tilde{\phi}_i | \mathbf{r} \rangle \langle \mathbf{r} | \tilde{\phi}_j \rangle. \tag{2.60}$$

ρ_{ij} are the occupation of each augmentation channel (i, j) and are calculated from the PS wave functions applying the projector function,

$$\rho_{ij} \;=\; \sum_n f_n \langle \tilde{\Psi}_n | \tilde{p}_i \rangle \langle \tilde{p}_j | \tilde{\Psi}_n \rangle. \tag{2.61}$$

It should be pointed out here that for a complete set of projector functions the charge density $\tilde{n}^1$ is exactly same as $\tilde{n}$ within Ω_R.

2.4.2 The total energy functional

The total energy can be written as a sum of three terms,

$$E \;=\; \tilde{E} + E^1 - \tilde{E}^1, \tag{2.62}$$

where the first term,

$$\begin{aligned}\tilde{E} &= \sum_n f_n \langle \tilde{\Psi}_n | -\frac{1}{2}\nabla^2 | \tilde{\Psi}_n \rangle + E_{xc}[\tilde{n}+\hat{n}+\tilde{n}_c] + E_H[\tilde{n}+\hat{n}] \\ &+ \int v_H[\tilde{n}_{Zc}][\tilde{n}(\mathbf{r})+\hat{n}(\mathbf{r})]d\mathbf{r} + U(\mathbf{R}, Z_{ion}). \end{aligned} \tag{2.63}$$

$n_{Zc}(\tilde{n}_{Zc})$ is the sum of the point charge density of the nuclei $n_Z(\tilde{n}_z)$ and the frozen core charge density $n_c(\tilde{n}_c)$, i.e. $n_{Zc} = n_z + n_c$ and $\tilde{n}_{Zc} = \tilde{n}_z + \tilde{n}_c$ and $\hat{n}$ is the compensation charge, which is added to the soft charge densities $\tilde{n} + \tilde{n}_{Zc}$ and $\tilde{n}^1 + \tilde{n}_{Zc}$ to reproduce the correct multipole moments of the AE charge density $n^1 + n_{Zc}$ located in each augmentation region. As n_{Zc} and $\tilde{n}_{Zc}$ have same monopole $-Z_{ion}$ and vanishing multipoles, the compensation charge $\hat{n}$ is chosen so that $\tilde{n}^1 + \hat{n}$ has the same moments as AE valence charge density n^1 has, within each augmentation region. $U(\mathbf{R}, Z_{ion})$ is the electrostatic interaction potential between the cores.

The second term in the total energy is,

$$\begin{aligned}E^1 &= \sum_{ij} \rho_{ij} \langle \phi_i | -\frac{1}{2}\nabla^2 | \phi_j \rangle + \overline{E_{xc}[n^1+n_c]} + \overline{E_H[n^1]} \\ &+ \int_{\Omega_r} v_H[n_{n_{Zc}}] n^1(\mathbf{r}) d\mathbf{r}. \end{aligned} \tag{2.64}$$

and the final term is,

$$\begin{aligned}\tilde{E}^1 &= \sum_{ij} \rho_{ij} \langle \tilde{\phi}_i | -\frac{1}{2}\nabla^2 | \tilde{\phi}_j \rangle \; + \; \overline{E_{xc}[\tilde{n}^1+\hat{n}+\tilde{n}_c]} + \overline{E_H[\tilde{n}^1+\hat{n}]} \\ &+ \int_{\Omega_r} v_H[\tilde{n}_{Zc}][\tilde{n}^1(\mathbf{r})+\hat{n}(\mathbf{r})]d\mathbf{r}, \end{aligned} \tag{2.65}$$

In all these three energy terms, the electrostatic potential $v_H[n]$ and electrostatic energy $E_H[n]$ of charge density n is given by:

$$v_H[n](\mathbf{r}) = \int \frac{n(\mathbf{r}')}{|\mathbf{r}-\mathbf{r}'|} d\mathbf{r}', \tag{2.66}$$

$$E_H[n] = \frac{1}{2} \int d\mathbf{r} \int d\mathbf{r}' \frac{n(\mathbf{r}) n(\mathbf{r}')}{|\mathbf{r}-\mathbf{r}'|}. \tag{2.67}$$

In the total energy functional the smooth part $\tilde{E}$ is evaluated on a regular grids in Fourier or real space, and the two one-center contributions $E^1$and $\tilde{E}^1$ are evaluated on radial grids for each sphere individually.

2.4.3 Compensation charge density

The compensation charge density $\hat{n}$ is defined such that $\tilde{n}^1 + \hat{n}$ has exactly the same moments as the AE charge density n^1 has, within the augmentation region, which then requires,

$$\int_{\Omega_r} (n^1 - \tilde{n}^1 - \hat{n})|\mathbf{r} - \mathbf{R}|^l Y_L^*(\widehat{\mathbf{r} - \mathbf{R}}) d\mathbf{r} \;=\; 0. \tag{2.68}$$

The charge difference Q_{ij} between the AE and PS partial wave for each channel (i, j) within the augmentation region is defined by,

$$Q_{ij}(\mathbf{r}) \;=\; \phi_i^*(\mathbf{r})\phi_j(\mathbf{r}) - \tilde{\phi}_i^*(\mathbf{r})\tilde{\phi}_j(\mathbf{r}), \tag{2.69}$$

and their moments q_{ij}^L are,

$$q_{ij}^L \;=\; \int_{\Omega_r} Q_{ij}(\mathbf{r})|\mathbf{r} - \mathbf{R}|^l Y_L^*(\widehat{\mathbf{r} - \mathbf{R}}) d\mathbf{r}, \tag{2.70}$$

which has non zero values only for certain combinations of L, i and j. Then the compensation charge density can be rewritten as,

$$\hat{n} \;=\; \sum_{i,j,L} \rho_{ij} \hat{Q}_{ij}^L(\mathbf{r}), \tag{2.71}$$

where,

$$\hat{Q}_{ij}^L \;=\; q_{ij}^L g_l(|\mathbf{r} - \mathbf{R}|) Y_L(\widehat{\mathbf{r} - \mathbf{R}}), \tag{2.72}$$

where $g_l(r)$ are the functions for which the moment is equal to 1.

2.4.4 Operators

Let us consider some operator $\mathcal{O}$, so its expectation value $\langle \mathcal{O} \rangle = \sum_n f_n \langle \Psi_n | \mathcal{O} | \Psi_n \rangle$, where n is the band index and f_n is the occupation of the state. As in the PAW method we work with the PS wave function, we need to obtain observables as the expectation values of PS wave function. Applying the form of the transformation τ and using $\sum_i |\tilde{\phi}_i\rangle\langle\tilde{p}_i| = 1$ within the augmentation region Ω_R and $|\tilde{\phi}_i\rangle = |\phi_i\rangle$ outside the augmentation region, for quasilocal operators, the PS operator $\tilde{\mathcal{O}}$ has the following form[1]:

$$\tilde{\mathcal{O}} \quad = \quad \tau^\dagger \mathcal{O} \tau$$

[1]The kinetic energy operator $-1/2\nabla^2$ and the real space projector operators $|r\rangle\langle r|$ are quasi local operators. For truly nonlocal operators an extra term must be added to the $\tilde{\mathcal{O}}$ expression.

$$= \mathcal{O} + \sum_{ij} |\tilde{p}_i\rangle(\langle\phi_i|\mathcal{O}|\phi_j\rangle - \langle\tilde{\phi}_i|\mathcal{O}|\tilde{\phi}_j\rangle)\langle\tilde{p}_j|. \tag{2.73}$$

Overlap operator: The PS wave function obey orthogonality condition,

$$\langle\tilde{\Psi}_n|\mathcal{S}|\tilde{\Psi}_m\rangle = \delta_{nm}, \tag{2.74}$$

where $\mathcal{S}$ is the overlap operator in the PAW approach. The overlap matrix in the AE representation is given by the matrix elements of unitary operator. Therefore, $\mathcal{S}$ has the form given by,

$$\mathcal{S}[\{\mathbf{R}\}] = 1 + \sum_{i} |\tilde{p}_i\rangle[\langle\phi_i|\phi_j\rangle - \langle\tilde{\phi}_i|\tilde{\phi}_j\rangle]\langle\tilde{p}_j|. \tag{2.75}$$

Hamiltonian operator: The Hamiltonian operator is defined as the first derivative of the total energy functional with respect to the density operator, $\tilde{\rho} = \sum_n f_n|\tilde{\Psi}_n\rangle\langle\tilde{\Psi}_n|$,

$$H = \frac{dE}{d\tilde{\rho}}, \tag{2.76}$$

where the PS density operator $\tilde{\rho}$ depends on the PS charge density $\tilde{n}$ and on the occupancies of each augmentation channel ρ_{ij}. So the variation of the total energy functional can be rewritten as,

$$\frac{dE}{d\tilde{\rho}} = \frac{\partial E}{\partial\tilde{\rho}} + \int \frac{\delta E}{\delta\tilde{n}(\mathbf{r})}\frac{\partial\tilde{n}(\mathbf{r})}{\partial\tilde{\rho}}d\mathbf{r} + \sum_{i,j}\frac{\partial E}{\partial\rho_{ij}}\frac{\partial\rho_{ij}}{\partial\tilde{\rho}}. \tag{2.77}$$

The partial derivative of $\tilde{E}$ with respect to the PS density operator is the kinetic energy operator and the variation with respect to $\tilde{n}(\mathbf{r})$ leads to the usual one-electron potential $\tilde{v}_{eff}$,

$$\frac{\partial\tilde{E}}{\partial\tilde{\rho}} = -\frac{1}{2}\nabla^2, \tag{2.78}$$

and,

$$\frac{\delta\tilde{E}}{\delta\tilde{n}(\mathbf{r})} = \tilde{v}_{eff} = v_H[\tilde{n} + \hat{n} + \tilde{n}_{Zc}] + v_{xc}[\tilde{n} + \hat{n} + \tilde{n}_c]. \tag{2.79}$$

As in the smooth part of the total energy functional, $\tilde{E}$, the occupancies ρ_{ij} enter only through the compensation charge density $\hat{n}$, the variation of $\tilde{E}$ with respect to ρ_{ij} is given by,

$$\begin{aligned}\hat{D}_{ij} = \frac{\partial\tilde{E}}{\partial\rho_{ij}} &= \int\frac{\delta\tilde{E}}{\delta\hat{n}(\mathbf{r})}\frac{\partial\hat{n}(\mathbf{r})}{\partial\rho_{ij}}d\mathbf{r} \\ &= \sum_L\int\tilde{v}_{eff}(\mathbf{r})\hat{Q}_{ij}^L(\mathbf{r})d\mathbf{r}.\end{aligned} \tag{2.80}$$

In the remaining two terms E^1 and $\tilde{E}^1$ in the energy functional, ρ_{ij} enters directly via kinetic energy or through n^1, $\tilde{n}^1$ and $\hat{n}$. Now the variation of E^1 with the occupancies ρ_{ij} is given by,

$$D^1_{ij} \;=\; \frac{\partial E^1}{\partial \rho_{ij}} = \langle \phi_i | -\frac{1}{2}\nabla^2 + v^1_{eff} | \phi_j \rangle, \tag{2.81}$$

where,

$$v^1_{eff}[n^1] \;=\; v_H[n^1 + n_{Zc}] + v_{xc}[n^1 + n_c], \tag{2.82}$$

and the variation of $\tilde{E}^1$ is given by,

$$\tilde{D}^1_{ij} \;=\; \frac{\partial \tilde{E}^1}{\partial \rho_{ij}} = \langle \tilde{\phi}_i | -\frac{1}{2}\nabla^2 + \tilde{v}^1_{eff} | \tilde{\phi}_j \rangle + \sum_L \int_{\Omega_r} d\mathbf{r} \tilde{v}^1_{eff}(\mathbf{r}) \hat{Q}^L_{ij}(\mathbf{r}), \tag{2.83}$$

where,

$$\tilde{v}^1_{eff}[\tilde{n}^1] \;=\; v_H[\tilde{n}^1 + \hat{n} + \tilde{n}_{Zc}] + v_{xc}[\tilde{n}^1 + \hat{n} + \tilde{n}_c]. \tag{2.84}$$

The onsite terms D^1_{ij} and $\tilde{D}^1_{ij}$ are evaluated on radial grid within each augmentation region and they restore the correct shape of the AE wave function within the sphere. The final form of the Hamiltonian operator:

$$H[\rho, \{\mathbf{R}\}] \;=\; -\frac{1}{2}\nabla^2 + \tilde{v}_{eff} + \sum_{i,j} |\tilde{p}_i\rangle (\hat{D}_{ij} + D^1_{ij} - \tilde{D}^1_{ij}) \langle \tilde{p}_j |. \tag{2.85}$$

2.4.5 Forces in the PAW method

Forces are usually defined as the total derivative of the energy with respect to the ionic position $\mathbf{R}$,

$$\mathbf{F} \;=\; -\frac{dE}{d\mathbf{R}}. \tag{2.86}$$

The total derivative consists of two terms, first one is the forces on the ionic core and the second term is the correction due to the change of AE wave functions for fixed PS wave functions when ions are moved. This correction term comes because augmentation depends on the ionic positions and are known as Pulay force [61]. When calculating this Pulay correction one must consider the overlap between the wave functions due to the change in ionic position. According to Goedecker and Maschke [62], the total derivative can be written as,

$$\frac{dE}{d\mathbf{R}} \;=\; \frac{\partial U(\mathbf{R}, Z_{ion})}{\partial \mathbf{R}} + \sum_n f_n \left\langle \tilde{\Psi}_n \left| \frac{\partial (H[\rho, \{\mathbf{r}\}] - \epsilon_n \mathcal{S}[\{\mathbf{R}\}])}{\partial \mathbf{R}} \right| \tilde{\Psi}_n \right\rangle, \tag{2.87}$$

where the first term is the forces between the ionic cores and ϵ_n are the Kohn-Sham eigenvalues, and the PS wave functions assumed to satisfy the orthogonality condition $\langle\tilde{\Psi}_n|\mathcal{S}|\tilde{\Psi}_m\rangle = \delta_{nm}$ and the corresponding Kohn-Sham equation, reads $H|\tilde{\Psi}_n\rangle = \epsilon_n\mathcal{S}|\tilde{\Psi}_n\rangle$.

The first contribution, $\mathbf{F}^1$ to the second term of the total derivative comes from the change in the effective local potential $\tilde{v}_{eff}$ when the ions are moved and $\tilde{v}_{eff}$ depends explicitly on the ionic positions via $\hat{n}_{Zc}$,

$$\mathbf{F}^1 = -\int \left[\frac{\delta Tr[H\tilde{\rho}]}{\delta v_H[\tilde{n}_{Zc}](\mathbf{R})}\frac{\partial v_H[\tilde{n}_{Zc}](\mathbf{R})}{\partial \mathbf{R}}\right] d\mathbf{R}. \tag{2.88}$$

This equation can be further simplified to,

$$\begin{aligned}\mathbf{F}^1 &= -\int \left(\tilde{n}(\mathbf{r}) + \sum_{i,j,L}\hat{Q}^L_{ij}(\mathbf{r})\rho_{ij}\right)\frac{\partial v_H[\tilde{n}_{Zc}](\mathbf{r})}{\partial \mathbf{R}}d\mathbf{r} \\ &= -\int [\tilde{n}(\mathbf{r}) + \hat{n}(\mathbf{r})]\,\frac{\partial v_H[\tilde{n}_{Zc}](\mathbf{r})}{\partial \mathbf{R}}d\mathbf{r}.\end{aligned} \tag{2.89}$$

The second contribution arise from $\hat{D}_{ij}$ due to the changes in the compensation charge density $\hat{n}$, when ions are moved,

$$\mathbf{F}^2 = -\sum_{i,j,L}\int \tilde{v}_{eff}(\mathbf{r})\rho_{ij}q^L_{ij}\frac{\partial g_l(|\mathbf{r}-\mathbf{R}|)Y_L(\widehat{\mathbf{r}-\mathbf{R}})}{\partial \mathbf{R}}d\mathbf{r}. \tag{2.90}$$

These two terms, $\mathbf{F}^1$ and $\mathbf{F}^2$, together describe the electrostatic contributions to the force. The third term comes due to the change in the projector function $\tilde{p}_i$ as ions are moved,

$$\mathbf{F}^3 = -\sum_{n,i,j}(\hat{D}_{ij} + D^1_{ij} - \tilde{D}^1_{ij} - \epsilon_n q_{ij})f_n\left\langle\tilde{\Psi}_n\left|\frac{\partial|\tilde{p}_i\rangle\langle\tilde{p}_j|}{\partial \mathbf{R}}\right|\tilde{\Psi}_n\right\rangle, \tag{2.91}$$

where $q_{ij} = \langle\phi_i|\phi_j\rangle - \langle\tilde{\phi}_i|\tilde{\phi}_j\rangle$.

As the exchange-correlation potential depends on the nonlinear core corrections $\tilde{n}_c$ gives an additional contribution, which can be obtained from the total energy functional,

$$\mathbf{F}^{\text{nlcc}} = -\int v_{xc}[\tilde{n} + \hat{n} + \tilde{n}_c]\frac{\partial \tilde{n}_c(\mathbf{r})}{\partial \mathbf{R}}d\mathbf{r}. \tag{2.92}$$

All the differences between the PAW method and ultra-soft pseudopotential are automatically absorbed in the in the definition of $(\hat{D}_{ij} + D^1_{ij} - \tilde{D}^1_{ij})$. $D^1_{ij} - \tilde{D}^1_{ij}$ are constant for US-PP, where they are calculated once and forever whereas in PAW method they vary during the calculation of the electronic ground state.

Chapter 3

Tight-binding molecular dynamics study of copper clusters

In this chapter we shall use a minimal parameter tight binding molecular dynamics scheme (Section 2.1) to study copper clusters in the size range of n = 2-55. We shall present ground state geometries, binding energies, relative stabilities, HOMO-LUMO gap and ionization potentials. A detailed comparison will been made with our previous first-principles (full potential linearized muffin-tin orbital) calculations for small size range $\leq$ 9 along with available experimental results. Good agreement will allow us to use the present TBMD method for medium sized clusters with $n \geq 10$. In the size range $10 \leq n \leq 55$ most of the clusters adopt icosahedral structure which can be derived from the 13-atom icosahedron, the ploy-icosahedral 19-, 23-, and 26-atom clusters and the 55-atom icosahedron, by adding or removing atoms. However, a local geometrical change from icosahedral to decahedral structure is observed for n = 40-44 and return to the icosahedral growth pattern is found at n = 45 which continues. Electronic "magic numbers" (2, 8, 20, 34, 40) in this regime are correctly reproduced. Due to electron pairing in the HOMOs, even-odd alternation is found. A sudden loss of even-odd alternation in second difference of cluster binding energy, HOMO-LUMO gap energy and ionization potential is observed in the region $n \sim 40$ due to structural change there. Interplay between electronic and geometrical structure is found. [1]

[1] This chapter is based on the following papers:
(1) **Mukul Kabir**, Abhijit Mookerjee and A. K. Bhattacharya, *Structure and stability of Cu clusters: A tight-binding molecular dynamics study*, Physical Review A, **69**, 043203 (2004).
(2) **Mukul Kabir**, Abhijit Mookerjee and A. K. Bhattacharya, *Copper clusters: Electronic effect domi-*

3.1 Introduction

Metallic clusters play a central role in catalysis [63]-[66] and nanotechnology [67]-[69]. Clusters of coinage metals Cu, Ag and Au have been used in a wide range of demonstration [63]-[69]. The determination of structural and electronic properties and the growth pattern of coinage metal clusters are of much interest both experimentally [10]-[13],[70]-[76] and theoretically [77]-[81]. The electronic configuration of the coinage metals are characterized by a closed d shell and a single s valance electron [Cu: $Ar(3d)^{10}(4s)^1$, Ag: $Kr(4d)^{10}(5s)^1$, Au: $Xe(5d)^{10}(6s)^1$]. Due to the presence of single s electrons in the atomic outer shells, the noble metal clusters are expected to exhibit certain similarities to the alkali metal clusters. Electronic structure of alkali metal clusters are well described by the spherical shell model, which has successfully interpreted the "magic numbers" in Na_n and K_n clusters [1, 2]. A number of experimental features of noble metal clusters are also qualitatively well described in terms of simple s electron shell model. For instance, the mass abundance spectrum of Cu_n^-, Ag_n^- and Au_n^- clusters, which reflects the stability of clusters, can be explained by the one-electron shell model [10, 11]. But some experimental studies [70]-[73] indicate that the localized d electrons of the noble metals play a significant role for the geometrical and electronic structure through the hybridization with more extended valence s electron . Therefore, it is important to include the contribution of $3d$ electrons and the $s-d$ hybridization for Cu_n clusters.

Bare copper clusters in the gas phase have been studied experimentally by Taylor *et al.* [74] and Ho *et al.* [75] using photo-electron spectroscopy (PES). Knickelbein measured ionization potentials of neutral copper clusters and found evidence of electronic shell structure [13]. Very recently cationic copper clusters have been studied using threshold collision-induced dissociation (TCID) by Spasov *et al.* [76]. Copper clusters have been also investigated theoretically by various accurate quantum mechanical and

---

nates over geometrical effect, European Physical Journal D **31**, 477 (2004).

(3) **Mukul Kabir**, Abhijit Mookerjee, R. P. Datta, A. Banerjea and A. K. Bhattacharya, *Study of small metallic nanoparticles: An ab initio full-potential muffin-tin orbitals based molecular dynamics study of small Cu clusters*, Int. J. Mod. Physics B **17**, 2061 (2003).

(4) **Mukul Kabir**, Abhijit Mookerjee and A. K. Bhattacharya, *Tight-Binding molecular dynamics study of Copper clusters*, Nano-Scale Materials: From Science to Technology, Eds. S. N. Sahu, R. K. Choudhury and P. Jena (Nova, New York, 2006).

chemical approaches. Massobrio *et al.* [77] studied the structures and energetics of Cu_n ($n = 2, 3, 4, 6, 8, 10$) within the local density approximation of density functional theory (DF-LDA) by using the Car Parinello (CP) method. Calaminici *et al.* [78] used the linear combination of Gaussian-type orbitals density functional (LCGTO-DFT) approach to study Cu_n, Cu_n^- and Cu_n^+ clusters with $n \leq 5$. Akeby *et al.* [79] used the configuration interaction (CI) method with an effective core potential (ECP) for $n \leq 10$. We also have [80] studied the small Cu_n clusters for $n \leq 9$ by using full-potential muffin-tin orbitals (FP-LMTO) technique. Here in this chapter we will not discuss those FP-LMTO results explicitly, but would compare with the TB results.

Ideally, the sophisticated, quantum chemistry based, first-principles methods predict both the stable geometries and energetics to a very high degree of accuracy. The practical problem arises from the fact that for actual implementation these techniques are limited to small clusters only. None of the methods described above can be implemented for clusters much larger than ~ 10 atoms, because of prohibitive computational expense. The aim of this communication is to introduce an semi-empirical method, which nevertheless retains some of the electronic structure features of the problem. The empirical parameters are determined from first-principles calculations for small clusters, and corrections introduced for local environmental corrections in the larger clusters.

In recent years empirical tight-binding molecular dynamics (TB-MD) method has been developed as an alternative to *ab initio* methods. As compared with *ab initio* methods, the parameterized tight-binding Hamiltonian reduces the computational cost dramatically. The main problem with the empirical tight-binding methods has always been the lack of transferability of its empirical parameters. We shall describe here a technique that allows us to fit the parameters of the model from a fully *ab initio*, self-consistent local spin-density approximation (LSDA) based FP-LMTO calculation reported earlier by us [80] for the smaller clusters and then make correction for the new environment for clusters in order to ensure transferability (at least to a degree).

It should be mentioned here that Copper clusters have also been investigated by other empirical methods. D'Agostino carried molecular dynamics using a quasi-empirical potential derived from a tight-binding approach for nearly 1300 atoms [81]. More recently Darby *et al.* carried geometry optimization by genetic algorithm using Gupta potential

[82] for Cu_n, Au_n and their alloy clusters in the size range $n \leq 56$ [83]. These kinds of empirical atomistic potentials are found to be good to predict ground state geometries but can not predict electronic properties such as electronic shell closing effect for n =2, 8, 20, 40, ..., highest occupied-lowest unoccupied molecular level (HOMO-LUMO) gap energy and ionization potential. Our proposed TBMD scheme will allow us to extrapolate to the larger clusters to study both the ground state geometries as well as ground state energetics as a function of cluster size. Menon *et al.* have proposed a minimal parameter tight-binding molecular dynamics (TBMD) scheme for semiconductors [84]-[86] and extended the method for transition metal (Ni_n and Fe_n) clusters [87, 30]. Recently Zhao *et al.* has applied this method for silver clusters [88]. In the present work, we shall introduce a similar TB model for copper.

Using this TBMD method, we shall investigate the stable structures, cohesive energies, relative stabilities, HOMO-LUMO gaps and ionization potentials of Cu_n clusters in the size range $n \leq 55$. We shall indicate the comparison between the present results for small clusters, $n \leq 9$, with those of our previous FP-LMTO calculations and other *ab initio* and available experimental results. This is essential before we go over to the computationally expensive study of larger clusters.

3.2 Methodology

We have used TB molecular dynamics to study the copper clusters in the size range n = 2-55. The TBMD has extensively been described in the Section2.1 in great detail. The parameter r_d, the on site energies and the universal constants $\eta_{\lambda,\lambda',\mu}$ are taken from Harrison [31] and are given in the Table 3.1.

To prevent the p-orbital mixing, we set $E_s = E_d$ and E_p large enough. The choice of out TB parameters reproduces the band structure of the face-centered cubic bulk Cu crystal. In the present scheme we have four adjustable parameters, ϕ_0 in the equation 2.5 and a, b, c in the equation 2.6. The vale of ϕ_0 is fitted to reproduce the correct experimental bond length for the Cu dimer (2.22 Å[89]). In the present case we found a value 0.34 eV for ϕ_0. We found the vibrational frequency of Cu_2 is to be 226 cm^{-1}, which has reasonable agreement with the experimental value (265 cm^{-1}) [90]. The parameters,

Table 3.1: Parameter r_d, on site energies,E_s, E_p and E_d and the universal constants $\eta_{\lambda,\lambda',\mu}$ for Cu [31].

Parameter	Value	Parameter	Value
r_d	0.67 Å	E_s	-20.14 eV
E_p	100 eV	E_d	-20.14 eV
$\eta_{ss\sigma}$	-0.48	$\eta_{sp\sigma}$	1.84
$\eta_{pp\sigma}$	3.24	$\eta_{pp\pi}$	-0.81
$\eta_{sd\sigma}$	-3.16	$\eta_{pd\sigma}$	-2.95
$\eta_{pd\pi}$	1.36	$\eta_{dd\sigma}$	-16.20
$\eta_{dd\pi}$	8.75	$\eta_{dd\delta}$	0.00

a, b and c, are obtained by fitting the coordination dependent term to our FP-LMTO *ab initio* results [80] for the three different small clusters according to the equation

$$E_{bond} = E_{ab\ initio} - E_{el} - E_{rep}. \tag{3.1}$$

To determine the parameters a, b and c, we use the experimental binding energy (1.03 eV/atom [89]) of Cu_2 and binding energy of Cu_4 and Cu_6 from our previous *ab initio* FP-LMTO calculation. This gave $a = -0.0671$ eV, $b = 1.2375$ eV and $c = -3.042$ eV. In the present case we took the cutoff distance $r_c = 3.5$ Åand $\triangle = 0.1$ Å. These four parameters, once adjusted for small clusters to reproduce the known experimental or theoretical results, are then kept fixed in the subsequent calculations for clusters of arbitrary size.

3.3 Results

We have applied this TBMD scheme to Cu_n clusters for $n \leq 55$. Since the present scheme imposes no *a priori* symmetry restrictions, we can perform full optimization of cluster geometries. For small clusters ($n \leq 9$) we can able to perform a full configurational space search to determine the lowest-energy configuration. Here they serve as a test case for the calculation of larger clusters with $n \geq 10$. In Table 3.2 we present a detailed comparison of binding energy per atom, difference in binding energy $\triangle E$ and average bond length $\langle r \rangle$ for $n \leq 9$ with available experimental [76] and *ab initio* [77, 79, 80] results.

Table 3.2: Point group (PG) symmetry, cohesive energy per atom, difference in cohesive energy per atom $\triangle E$ and average bond length $\langle r \rangle$ of the ground state structure and different isomers for Cu_n clusters with $n \leq 9$ obtained from TB calculation and comparison with *ab initio* calculations [80, 79, 77]. $\triangle E = 0.00$ represents the most stable structure for a particular n. Cohesive energy corresponding to the ground state structure in FP-LMTO [80], DF-LDA [77] (in parentheses) calculations and the values from TCID experiment [76] are given. For Cu_7, $C_{3v}(I)$ is the bi-capped trigonal bi-prism and $C_{3v}(II)$ is the capped octahedron.

Cluster	PG	Binding Energy (eV/atom)			$\triangle E$ (eV/atom)			$\langle r \rangle$
		Present	Theory[1]	Experiment[2]	Present	Theory[3]	Theory[4]	(Å)
Cu_3	C_{2v}	1.43	1.60(1.63)	1.07±0.12	0.00		0.00	2.25
	D_{3h}	1.32			0.11	0.06		2.24
	$D_{\infty h}$	1.13			0.30	0.00		2.24
Cu_4	D_{2h}	2.00	2.00(2.09)	1.48±0.14	0.00	0.00	0.00	2.23
	D_{4h}	1.73			0.27	0.56		2.22
	T_d	1.46			0.54	0.89		2.24
Cu_5	C_{2v}	2.24	2.19	1.56±0.15	0.00	0.00		2.23
	D_{3h}	2.03			0.21	0.37		2.38
Cu_6	C_{5v}	2.54	2.40(2.49)	1.73±0.18	0.00	0.00	0.00	2.40
	C_{2v}	2.40			0.14		0.01	2.39
	O_h	1.98			0.56	0.87	0.04	2.41
Cu_7	D_{5h}	2.63	2.65	1.86±0.22	0.00	0.00		2.41
	$C_{3v}(I)$	2.50			0.13	0.32		2.63
	$C_{3v}(II)$	2.30			0.33			2.45
Cu_8	C_s	2.87	2.73(2.84)	2.00±0.23	0.00		0.20	2.41
	O_h	2.64			0.23			2.61
	D_{2d}	2.57			0.30		0.00	2.59
	T_d	2.51			0.36		0.15	2.39
Cu_9	C_2	2.87	2.80		0.00			2.44
	C_{2v}	2.84			0.03			2.59
	C_s	2.60			0.27			2.41

[1]From Kabir *et al.* (Ref. [80]) and Massobrio *et al.* (Ref. [77]).
[2]Calculated from Spasov *et al.* (Ref. [76]).
[3]From Akeby *et al.* (Ref. [79]).
[4]From Massobrio *et al.* (Ref. [77]).

We carried molecular dynamics starting from various different structures. A straightforward molecular dynamics will then lead to possibly a metastable structure. These are the isomers described in the following text. Of these isomers only one has the globally minimum energy. Since the present scheme imposes no *a priori* symmetry restrictions, we can perform full optimization of cluster geometries.

3.3.1 Ground state geometry and isomers

For the Cu_3 cluster we find the isosceles triangle with C_{2v} symmetry to be the most stable structure. In the present calculation the equilateral triangle (D_{3h} symmetry) and the linear structure ($D_{\infty h}$ symmetry) are the two isomers which are 0.11 eV/atom and 0.30 eV/atom lower in energy. Due to the Jahn-Teller distortion C_{2v} structure is energetically more favourable than the more symmetrical D_{3h} structure. This result is supported by the experimental study of Ho *et al.* [75], who found the C_{2v} and D_{3h} structures are nearly degenerate. Akeby *et al.* [79] reported an energy difference of 0.11 eV between the D_{3h} and $D_{\infty h}$ structures, which is 0.23 eV according to *ab initio* calculation [91]. In agreement with the present calculation Lammers *et al.* [92] also found the isosceles triangle (C_{2v}) to be the the most stable structure, which is 0.16 eV and 0.35 eV higher than the D_{3h} and $D_{\infty h}$ isomers respectively. Calaminici *et al.* [78] found the vertex angle to be 66.58^0, whereas it was 65^0 in our FP-LMTO calculation [80]. In the present TB calculation, we find it to be 61.3^0.

For the Cu_4 cluster our calculation predict the planer rhombus (D_{2h}) geometry to be the most stable with cohesive energy 2.00 eV/atom. We fond the two isomers, a perfect square (D_{4h} symmetry) and a tetrahedron (T_d symmetry), with cohesive energy 1.73 eV/atom and 1.46 eV/atom respectively. Experimental study [75] also favours the rhombic structure. Hückel calculations [93] suggest the rhombic geometry for the both Cu_4 and Cu_4^-. Our prediction is exactly supported by Akeby *et al.* [79] and Calaminici *et al.* [78], who also predicted the sequence D_{2h}-D_{4h}-T_d of decreasing stability. Our FP-LMTO calculation [80] was in agreement with the present TB sequence, whereas Lammers *et al.* [92] found a different sequence, T_d-D_{2h}-D_{4h}. The larger angle of the rhombus predicted 123^0 by Calaminici *et al.* [78] agrees well with the present calculation 119.8^0, which was

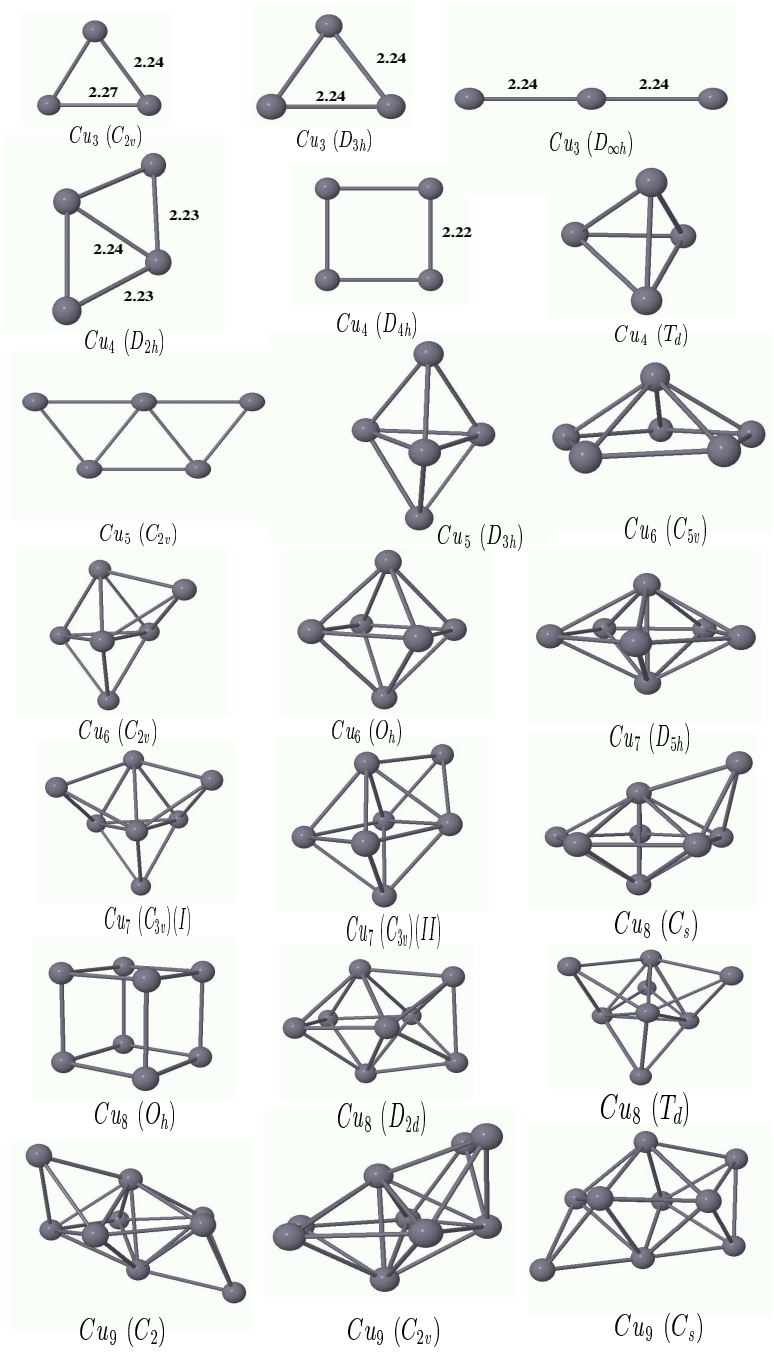

Figure 3.1: Ground state structure and isomers of Cu_n clusters for $n = 3 - 9$. Point group symmetries are given in the parentheses.

120^0 in our previous *ab initio* calculation [80].

In the case of the pentamer, Cu_5, three different structures were examined, viz., the square pyramid (C_{4v} symmetry), the trigonal bi-pyramid (D_{3h} symmetry) and the trapezoid (C_{2v} symmetry). Among these three different structures, we found the the planer trapezoidal C_{2v} structure to be the most stable, which is $\triangle E = 0.21$ eV/atom higher than the D_{3h} structure. In our simulation, the square pyramid C_{4v} was found to be unstable, relaxing to a D_{3h} structure. In the photo-electron spectroscopy [75] of Cu_n^-, Ag_n^- and Au_n^-, Ho *et al.* tentatively assign the trapezoidal planer geometry to the ground state of both the anion and neutral of the coinage metal pentamers. Present result doesn't agree with our previous *ab initio* calculation, where we found the D_{3h} structure to be the most stable but agrees with Calaminici *et al.* [78] and Akeby *et al.* [79], both of them found the C_{2v} structure to be most stable structure with the sequence C_{2v}-D_{3h}-C_{4v} of decreasing stability. Lammers *et al.* found an opposite sequence C_{4v}-D_{3h}-C_{2v}.

For the Cu_6 cluster we investigated three different structures, the octahedron (O_h symmetry), the capped trigonal bi-pyramid (C_{2v} symmetry) and the flat pentagonal pyramid (C_{5v} symmetry). Among these three structures, we found the flat pentagonal pyramid C_{5v} to be the most stable with cohesive energy 2.54 eV/atom. We found the two isomers, the capped trigonal bi-pyramid C_{2v} and the octahedron O_h, are $\triangle E = 0.14$ eV/atom and $\triangle E = 0.56$ eV/atom lower respectively. Massobrio *et al.* [77] and Akeby *et al.* [79] also found the C_{5v} structure as the ground state. This result does not agree with our previous *ab initio* calculation, where we found the C_{2v} structure as ground state. Lammers *at al.* [92] predict the O_h structure to be the most stable structure compared to other random structures.

In the case of Cu_7 cluster we considered three different structures, the pentagonal bi-pyramid (D_{5h} symmetry), the bi-capped trigonal bi-pyramid ($C_{3v}(I)$ symmetry) and the capped octahedron ($C_{3v}(II)$ symmetry), as our initial starting configurations. We found the pentagonal bi-pyramid with D_{5h} symmetry to be the most stable, which is energetically more favourable than the bi-capped trigonal pyramid and capped octahedron isomers by an energy $\triangle E = 0.13$ eV/atom and $\triangle E = 0.33$ eV/atom respectively. This result agrees well with Akeby *et al.* [79] and with the *ab initio* [80] calculation.

For the Cu_8 cluster, we examined four different structures, viz., the capped pentagonal bi-pyramid (C_s symmetry), the tri-capped trigonal bi-pyramid (T_d symmetry), the bi-

capped octahedron (D_{2d} symmetry) and the cube (O_h symmetry). In our simulation, we found the capped pentagonal bi-pyramid (C_s) to be the most stable with cohesive energy 2.87 eV/atom. We found the three isomers, O_h, D_{2d} and T_d, are lower in energy by $\triangle E = 0.23, 0.30$ and 0.36 eV/atom respectively. This result agrees with our *ab initio* calculation [80], where we found the C_s structure to be the most stable but with a different sequence C_s-D_{2d}-O_h with decreasing order of stability. In that study we have not studied the T_d structure. Massobrio *et al.* [77] found the D_{2d} structure to be the most stable structure followed by T_d and C_s structure.

For the Cu_9 cluster, we examined three different structures, the tri-capped octahedron (C_s symmetry), the bi-capped pentagonal bi-pyramid (BPB) with capping atoms on the adjacent faces (C_{2v} symmetry) and the BPB with capping atoms on the non adjacent faces (C_2 symmetry). Among these three structures, the BPB with capping atom on the non adjacent faces was found to be most stable with binding energy 2.87 eV/atom. This C_2 structure is nearly degenerate with the C_{2v} structure by an energy difference $\triangle E = 0.03$ eV/atom, whereas the C_s structure is less stable by an energy difference $\triangle E = 0.27$ eV/atom from the C_2 structure. Zhao *et al.* [88] found a BPB with C_{2v} symmetry to be the ground state for Ag_9 cluster. In our *ab initio* calculation [80], we found the tri-capped octahedron to be the ground state.

The present results and detailed comparisons with various experimental [75, 76] and *ab initio* [77]-[80],[91]-[93] results available, we find reasonable agreement among this TBMD scheme and the *ab initio* calculations for small clusters with $n \leq 9$ [80], which allow us to continue the use of this TBMD scheme for larger clusters with $n \geq 10$. For larger clusters ($10 \leq n \leq 55$), due to increasing degrees of freedom with cluster size, a full configurational search is not possible with the available computational resources. Instead, led by the experimental and theoretical results on small clusters, we examined structures of various symmetries for each size. Most stable structures for $n = 10 - 55$ atom clusters are given in Fig.3.2.

In this regime, the structures predicted by this TB model are mainly based on icosahedron. The most stable structure of Cu_7 is a pentagonal bi-pyramid (D_{5h} symmetry; see Table3.2), which is the building block for the larger clusters with $n \geq 10$. For Cu_{10}, we found a tri-capped pentagonal bi-pyramid to be the most stable structure. Ground

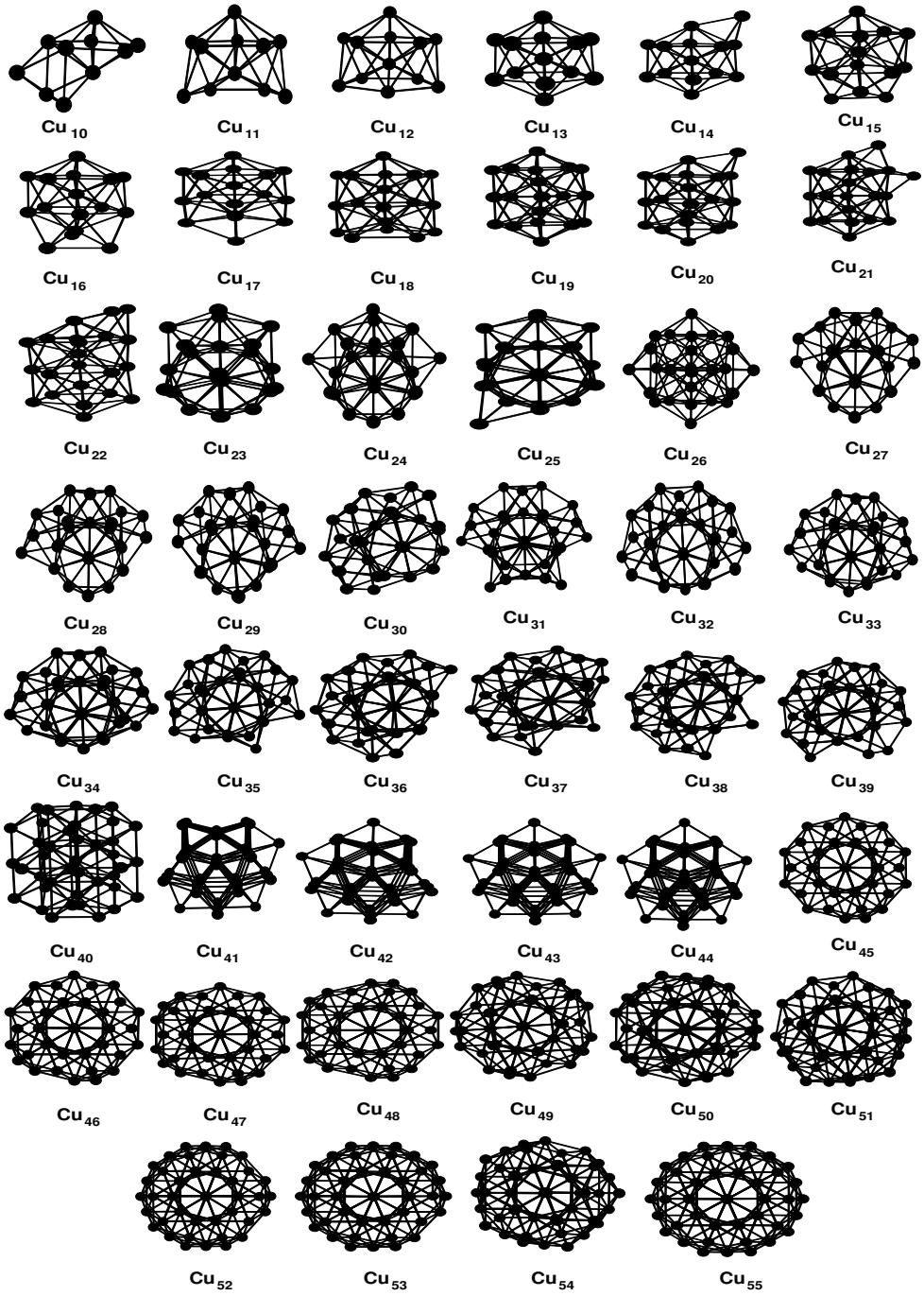

Figure 3.2: Most stable structures for copper clusters with $n = 10 - 55$ atoms. Most of the clusters adopt icosahedral structures except for $n = 40 - 44$, where the structures are decahedral.

state structures of Cu_{11} and Cu_{12} are the uncompleted icosahedron with lack of one and two atoms respectively and a Jahn-Teller distorted *first* complete icosahedron is formed at Cu_{13}. For Cu_{13}, the face-centered cubic like cub-octahedron is less stable than the icosahedron by an energy 0.05 eV per atom. In agreement Lammers and Borstal, on the basis of tight-binding linear muffin-tin orbital calculations, was also found the icosahedron to be the ground state of Cu_{13}, though the difference in energy between the icosahedron and the cub-octahedron was calculated to be only 0.2 eV/atom [92]. The ground state structures for Cu_{14}, Cu_{15}, Cu_{16}, and Cu_{17} are the 13- atom icosahedron plus one, two, three and four atoms respectively. A double icosahedron is formed for Cu_{19} (D_{5h} symmetry). This structure has two internal atoms, 12 six-coordinate atoms at either end and five eight-coordinate atoms around the waist of the cluster. Based on the structure for Cu_{19}, the stable Cu_{18} cluster is a double icosahedron minus one of the six-coordinate atoms located at either end (C_{5v} symmetry). Icosahedral growth continues for $20 \leq n \leq 55$ atom clusters. Poly-icosahedral structure in the form of a " triple icosahedron" (D_{3h} symmetry; the structure can be viewed as three inter-penetrating double icosahedra) is the most stable structure for Cu_{23} cluster. The next poly-icosahedral is found for Cu_{26} cluster. Finally, the *second* complete icosahedron is formed for Cu_{55} which is more stable than the closed cub-octahedral structure by an energy difference 6.27 eV. This can be explained in terms of their surface energy. The surface energy of the icosahedral structure is lower than that of the cub-octahedral structure, because the atoms on the surface of the icosahedron are five-coordinate compared to the four-coordinate atoms on the surface of the cub-octahedron. In our calculation, exception to the icosahedral growth is found at around Cu_{40}. The situation regarding geometrical structure in this size range is more complex. The structures for $n = 40 - 44$ atom clusters are oblate, decahedron like geometries. Return to the icosahedral structure is found at $n = 45$. In the size range $n = 40 - 44$, the structural sequence is decahedron-icosahedron-cub-octahedron in decreasing order of stability, whereas in the region $n = 45 - 55$, the structures retain icosahedron-decahedron-cub-octahedron sequence.

This results are in agreement with the experimental study of Winter and co-workers [12], where they found a bare copper cluster mass spectrum recorded with ArF laser ionization shows a sudden decrease in the ion signal at Cu_{42}^{+}, and from this observation

they argued that a change in geometrical structure might occur there, though they have not concluded about the nature of this geometrical change. They also found a dramatic decrease in water binding energy for Cu_{50} and Cu_{51}, and concluded that this may represent a return to the icosahedral structure as the *second* complete icosahedron is approached for Cu_{55}.

Our prediction agrees with the earlier work by D'Agostino [81], who performed molecular dynamics using a tight-binding many-body potential and found that icosahedral structures are prevalent for clusters containing less than about 1500 atoms. Valkealahti and Manninen [94], using effective medium theory, also found icosahedral structures are energetically more favourable than the cub-octahedral structures for sizes up to $n \sim 2500$ is consistent with our result: Fig.3.4 shows cub-octahedral structures are least stable among the three structures, icosahedron, decahedron and cub-octahedron. By contrast, Christensen and Jacobsen [95] predicted more face-centered cubic-like structures in the size range $n = 3-29$, in their Monte Carlo simulation using an effective medium potential. But they correctly reproduced the "magic numbers" in that regime [95, 96].

These results can be compared with the genetic algorithm study on copper clusters by Darby *et al.* [83], using Gupta potential. In agreement with the present study, Darby *et al.* found that most of the clusters in this regime adopt structures based on icosahedron. They also found exceptions to the icosahedral growth at around Cu_{40}, where the structures adopt decahedron like geometries (exact numbers are not available in the Ref. [83]). But the present study disagree with the genetic algorithm study in two points. Firstly, for 25 atom cluster, they found a more disordered structure, while the present study predict it to be an icosahedron based structure which can be derived by removing one surface atom from the 26-atom poly-icosahedron. Finally, they found an face-centered cubic-like truncated octahedral structure for Cu_{38}. Instead, the present study predict the icosahedron based structure to be the ground state, where this structure is energetically more favourable than the truncated octahedral structure by an energy $\triangle E = 0.17$ eV/atom. Although the genetic algorithm search for global minima is more efficient technique than molecular dynamics, use of the empirical atomistic potential is the main reason [97] for this kind of disagreement between Darby *et al.* and the present study.

3.3.2 Binding energies and relative stabilities

The computed size dependence of the binding energy per atom for Cu_n clusters with $n = 2-55$ is depicted in Fig.3.3 (upper panel). Among all the isomeric geometries examined for a certain cluster size n, the highest cohesive energy has been considered for the Fig.3.3. The overall shape of the curve matches the anticipated trend: binding energy grows monotonically with increasing the cluster size. Inset of the Fig.3.3 (upper panel) shows the comparison of our calculated binding energy with the *ab initio* [77, 80] and experimental [76] results. Experimentally the binding energies of the neutral clusters were derived from the dissociation energy data of anionic clusters from the TCID experiment [76] and using electron affinities from the PES experiment [75]. The inset figure shows that our calculated binding energies are in good agreement with those from DF-LDA [77] and our previous FP-LMTO [80] calculations. However, our binding energies are systematically overestimated, by an energy 0.53 ± 0.12 to 0.79 ± 0.22 eV, than the experimental binding energies. The LDA based *ab initio* calculations always over-estimate binding energies. This is a characteristic of the LDA. In the present study, TB parameters have been fitted to the *ab initio* LDA calculations for very small calculations [80]. It is not surprising therefore that the binding energies are over-estimated. In fact, the present results agree well with other LDA based calculations [77, 80], all of which overestimate the binding energy.

In the Fig.3.4, we compared binding energy per atom for cub-octahedral, decahedral and icosahedral structures for the clusters containing $n = 30 - 55$ atoms. Fig.3.4 shows most the clusters in this size range have icosahedral structures. However, a local structural change occurred for $n = 40 - 44$, where the structures adopt decahedral structure rather than icosahedral one. Return to the icosahedral growth pattern is found at $n = 45$ and continues up to 55-atom cluster. From the Fig.3.4 it is clear that among cub-octahedral, decahedral and icosahedral structures, cub-octahedral structures are least stable than the other two.

The second difference in the binding energy may be calculated as

$$\triangle_2 E(n) = E(n+1) + E(n-1) - 2E(n), \tag{3.2}$$

where $E(n)$ represents the total energy for an n-atom cluster. $\triangle_2 E(n)$ represents the

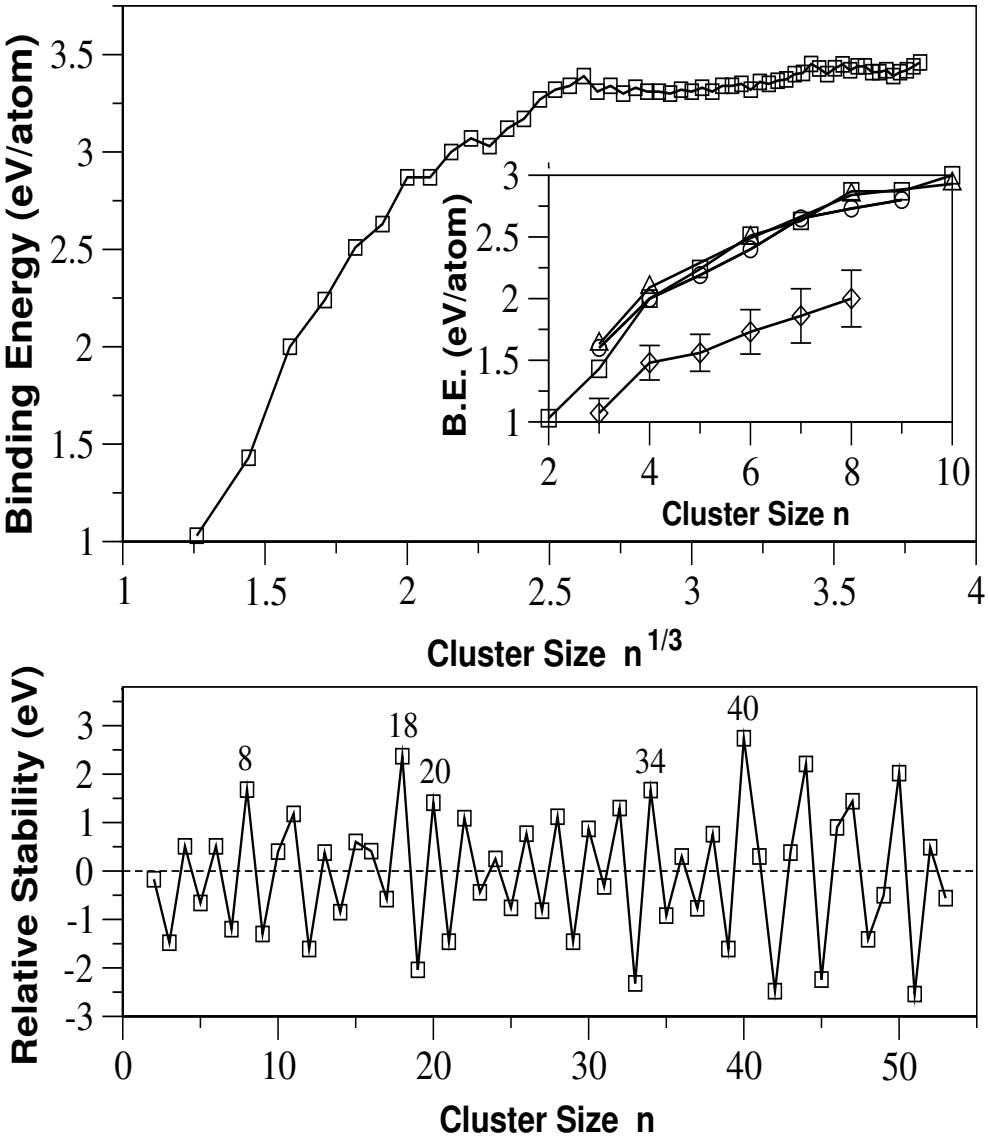

Figure 3.3: (Upper panel) Binding energy per atom as a function of cluster size $n^{1/3}$. Inset of the upper panel represents a comparison of binding energy per atom as a function of cluster size n, among the present TBMD (square), FP-LMTO (circle), DF-LDA (triangle) calculations and experimental (diamond) values. (Lower panel) Variation of relative stability $\triangle_2 E$ with cluster size n. Shell closing effect at $n = 8, 18, 20, 34, 40$ and even-odd alternation up to $n \sim 40$ are found. However, due to geometrical effect this even-odd alternation is disturbed at $n = 11, 13$ and 15.

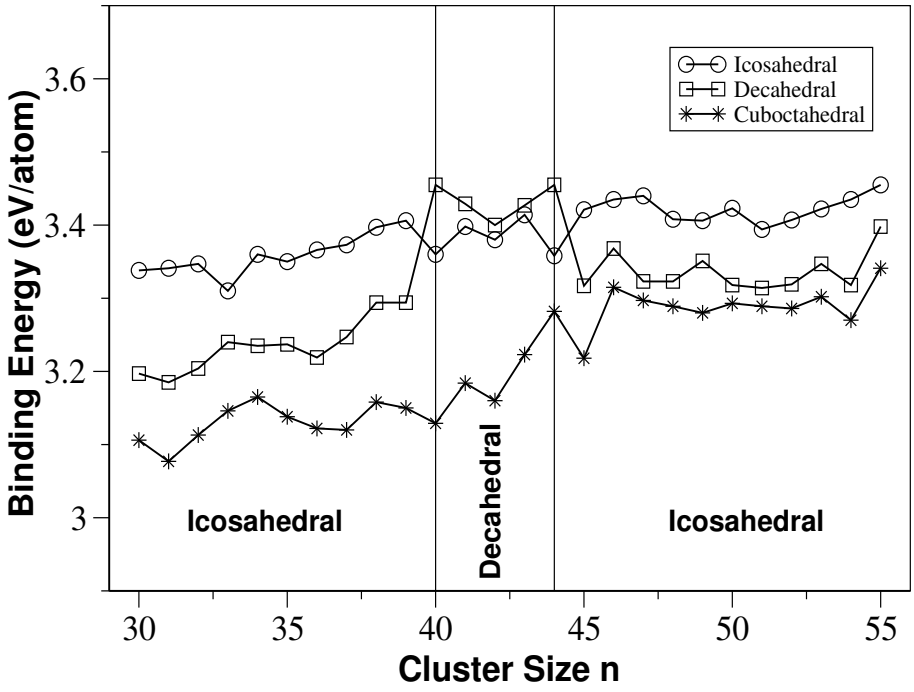

Figure 3.4: Comparison of binding energies per atom as a function of cluster size n among cub-octahedral, decahedral and icosahedral structures. For the whole region most of the clusters prefer icosahedral structure. However, a local geometrical change from icosahedral to decahedral structure is found for $n = 40 - 44$.

relative stability of an n-atom cluster with respect to its neighbors and can be directly compared to the experimental relative abundance : the peaks in $\triangle_2 E(n)$ coincide with the discontinuities in the mass spectra. These are plotted in the lower panel of Fig.3.3. We found three major characteristics in the Fig.3.3 (lower panel). Firstly, even-odd (even $>$ odd) oscillation is found. This can be explained in terms of electron pairing in HOMOs. Even (odd) clusters have an even (odd) number of electrons and the HOMO is doubly (singly) occupied. The electron in a doubly occupied HOMO will feel a stronger effective core potential because the electron screening is weaker for the electrons in the same orbital than for inner shell electrons. Thus the binding energy of the valence electron with an even cluster is larger than of an odd one. This even-odd alternation is prominent up to

$n \sim 40$. Secondly, due to electronic shell or sub-shell closing, we found particular high peak for $n = 8, 18, 20, 34$ and 40. Unfortunately, the present study does not show any evidence of electronic shell closing for Cu_2 in $\triangle_2 E(n)$. Finally, the even-odd alternation is reversed for $n = 10 - 16$ with maxima at Cu_{11}, Cu_{13} and Cu_{15}, which manifests the geometrical effect and therefore there is no peak at $n = 14$ due to electronic sub-shell closing. Simultaneous appearance of these three features in $\triangle_2 E(n)$ demonstrates the interplay between electronic and geometrical structure, which is in agreement with the experimental study of Winter *et al.* [12]. They found both jellium-like electronic behaviour and icosahedral structure in copper clusters. In an experimental study of mass spectra of ionized copper clusters [10, 11], substantial discontinuities in mass spectra at $n = 3, 9, 21, 35, 41$ for cationic and $n = 7, 19, 33, 39$ for anionic clusters as well as dramatic even-odd alternation are found. From the sudden loss in the even-odd alternation at Cu_{42} in the KrCl spectrum, Winter *et al.* argued about the possible geometrical change there. Therefore, we conclude in the section that sudden loss in the $\triangle_2 E$ vs n plot (lower panel of Fig.3.3) is due the structural change in that regime.

Such kind of electronic effects can not be reproduced by empirical atomistic potentials. Darby *et al.* [83], using the Gupta potential, found significant peaks at $n = 7$, 13, 19, 23 and 55 due to icosahedral (or poly-icosahedral) geometries. In the present study, we have found a peak at $n = 13$, but not at the other sizes found by them. However, the stable structures predicted by us are the same : the lowest energy structure of Cu_7 is a pentagonal bi-pyramid (D_{5h} symmetry) ; for $n = 13$ and 55, the structure are the *first* and *second* closed icosahedral geometries respectively. Poly-icosahedral structures are found for $n = 19$ (double icosahedron) and $n = 23$ (triple icosahedron) atom clusters. As the reason, the present study shows significant high peaks at Cu_8, Cu_{18} and Cu_{20} due to electronic shell closing effect and average peaks at Cu_{22} and Cu_{24} due to electron pairing effect. At these sizes, the electronic effects dominates over the geometrical effects and consequently the above peaks cannot observed by Darby *et al* .

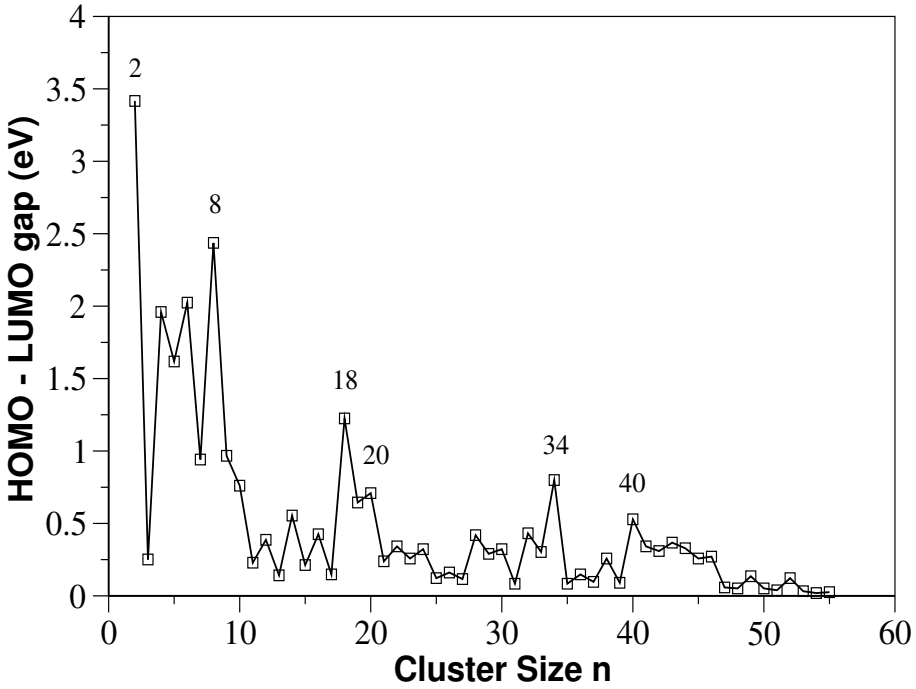

Figure 3.5: Highest occupied - lowest unoccupied molecular orbital (HOMO-LUMO) gap energy vs cluster size n. Electronic shell closer at $n = 2$, 8, 18, 20, 34, 40 and even-odd alternation are observed. However, sudden loss in even-odd alternation is found around $n \sim 40$ due to the structural change there.

3.3.3 HOMO-LUMO gap energies

Besides the second difference of the cluster binding energy, a sensitive quantity to probe the stability is the highest occupied-lowest unoccupied molecular level (HOMO-LUMO) gap energy. In the case of magic clusters shell or sub-shell closer manifests themselves in particularly large HOMO-LUMO gap, which was previously demonstrated experimentally [75, 16]. Calculated HOMO-LUMO gap energies are plotted in the Fig.3.5, where we observed even-odd alternation due to electron pairing effect and particularly large gap for $n = 2$, 8, 18, 20, 34 and 40 due to electronic shell and sub-shell closing. However, sudden loss of even-odd alternation is found around $n \sim 40$ due to the change in the geometrical structure in that region. Winter *et al.* [12] also found a sudden loss in even-odd alternation

in the KrCl spectrum at Cu_{42} and concluded this may coincide with any possible change in the geometrical structure there. In fact, Katakuse *et al.* [10, 11] observed identical behaviour in the mass spectra of sputtered copped and silver cluster ions : a dramatic loss of even-odd alternation at $n = 42$, signifying a sudden change to a geometrical structure in which stability, and abundance, is less sensitive to electron pairing. Therefore, the sudden loss in the Fig.3.5 again confirms the structural change there. So, the present study correctly predicts the "magic numbers" in this regime correctly and confirms the experimental prediction : a geometrical change (icosahedron $\rightarrow$ decahedron) is occurring around $n \sim 40$.

3.3.4 Ionization potentials

Within the present TB scheme, we can get a 'qualitative' description of the ionization potentials with cluster size according to Koopmans' theorem. This limitation arises mainly

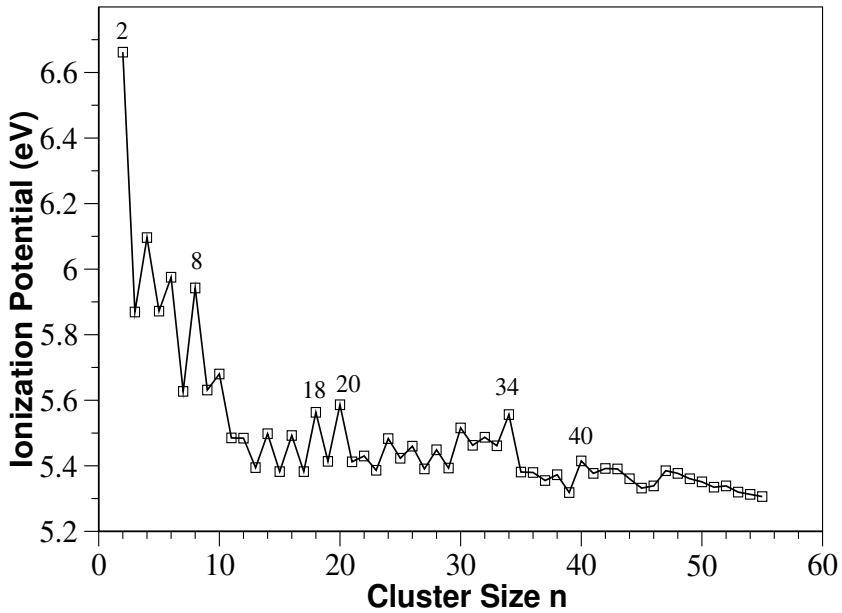

Figure 3.6: Ionization potential vs cluster size n. Electronic shell closing effect and prominent even-odd alternation up to $n \sim 40$ are observed.

from the choice of the Slater-Koster (SK) TB parameters and the extent of their transferability [98], which may be improved by the proposed scaling scheme of Cohen, Mehl and Papaconstantopoulos [99] . However, our aim is to get only a qualitative description of ionization potential with cluster size. Calculated ionization potentials are plotted in the Fig.3.6. In fact, we observed same pattern as it was in HOMO-LUMO gap energy *vs* cluster size : peaks at $n = 2$, 8, 18, 20, 34, 40 and even-odd alternation due to the same reasons discussed in the Sec. 3.3.2. and Sec. 3.3.3. Sudden loss in even-odd alternation around $n \sim 40$ is again confirmed from the Fig.3.6, which is due to the geometrical change there.

3.4 Conclusion

Using tight-binding model we calculated ground state geometries, binding energies, second differences in binding energy, HOMO-LUMO gap energies and ionization potentials for copper clusters in the size range $2 \leq n \leq 55$. We have fitted the parameters of the present TB scheme from our previous *ab initio* calculations [80]. For small clusters $n \leq 9$, present results show good agreement with experimental [75, 76] and theoretical [77, 78, 79, 80, 91, 92, 93] results, which allow us to go over the larger size range, $10 \leq n \leq 55$.

In the size range $10 \leq n \leq 55$ most of the clusters adopt icosahedral geometry which can be derived from the 13- atom icosahedron, the poly-icosahedral 19-, 23-, and 26-atom clusters and 55-atom icosahedron, by adding or removing atoms. However, exceptions to the icosahedral growth is found around $n \sim 40$. A local geometrical transition is found for $n = 40 - 44$- atom clusters. This is in agreement with the prediction of the two experimental studies by Katakuse *et al.* [10, 11] and Winter *et al.* [12], where they predicted that a local geometrical transition may occur at $n = 42$, though their results are not decisive about the nature of this geometrical change. Present results show that around $n \sim 40$ structures are changing from icosahedral to decahedral structure, where the structural sequence is decahedron-icosahedron-cub-octahedron in the decreasing order of stability. Return to the icosahedral growth is found at $n = 45$, with the sequence icosahedron-decahedron-cub-octahedron in the decreasing order of stability.

As we have fitted the parameters of the present TBMD scheme from LDA based

ab initio calculations [80], calculated binding energies are in good agreement with the LDA based *ab initio* calculations but overestimates the same calculated from the TCID experiment [76]. In the present scheme, the "magic numbers" (n = 2, 8, 18, 20, 34 and 40) due to electronic shell and sub-shell closing are correctly reproduced in the studied regime. Second difference of binding energy, HOMO-LUMO gap energy and ionization potential show even-odd oscillatory behaviour because of electron pairing in HOMOs in agreement with experiment. However, a sudden loss in even-odd alternation is found around $n \sim 40$ in the variation of second difference in binding energy, HOMO-LUMO gap energy and ionization potential with cluster size. This is in agreement with the experimental studies [10, 11, 12]. We conclude this is due to the geometrical change (icosahedron $\rightarrow$ decahedron) around there. Present results show that electronic structure can coexist with a fixed atomic packing.

Due to lower computational expense this TBMD scheme, with parameters fitted to first-principle calculation for the smaller clusters and with an environment correction, is a very efficient technique to study larger clusters, particularly with $n \geq 10$.

Chapter 4

Structure, electronic and magnetic transition in manganese clusters: An *ab initio* study

In this chapter, we shall discuss the electronic and magnetic properties of manganese clusters (n = 2 - 20). To investigate this we have used the density functional approach within a pseudo-potential method. Here we have used projector augmented wave (PAW) formalism to construct the pseudo-potential. All these methods are briefly outlined in the chapter 2. We observed a new kind of icosahedral structural growth in this size range. A ferromagnetic to ferrimagnetic transition takes place at $n = 5$ and the ferrimagnetic state continues to be the ground state for the entire size range discussed here. Presence of multiple isomers with different atomic spin orientation is important to note. Intrinsic magnetic orderings are in well agreement with the recent Stern-Gerlach experiments. Furthermore, finite size systems are very good for studying the dependency of orbital localization on coordination, which has been discuss in this chapter. No non-metal to metal transition has been observed in this size range, which was previously argued form the observed discontinuity in the reaction rate with molecular hydrogen. Before we proceed, it is very important to point out that we have assumed only collinear alignment of spins throughout this chapter. However, a spin canting or non-collinear spin ordering is possible in small magnetic clusters, which we will discuss in the following chapter[1].

[1]This chapter is based on the following chapters:
(1) **Mukul Kabir**, Abhijit Mookerjee and D.G. Kanhere, *Structure, electronic properties and magnetic transition in manganese clusters*, Physical Review B **73**, 224439 (2006).
(2) **Mukul Kabir**, Abhijit Mookerjee and D. G. Kanhere, *Magnetism in pure and doped manganese clusters: A review*, Atomic and Molecular Clusters: New Research (Nova, New York, 2006).

4.1 Introduction

The search for magnetic behavior in the transition metal clusters is motivated largely by the desire to understand how magnetic properties change in the reduced dimension. This is a question of considerable technological importance. Several unexpected magnetic orderings have already been reported in the reduced dimension. This ranges from the prediction of net magnetic moment in clusters of nonmagnetic (Rh [17]) or antiferromagnetic (Cr [25] and Mn [26, 27]) bulk materials to the enhancement in magnetic moment in clusters of ferromagnetic metals (Fe [18] and Co [19]-[23]). These have been discussed in the chapter 1.

Manganese clusters are particularly interesting among all $3d$ transition metal elements due to the $4s^2$, $3d^5$ electronic configuration in Mn atoms. Because of the filled $4s$ and half-filled $3d$ shells and the large energy gap $\sim$ 8 eV between these levels and as well as due to the high $4s^2 3d^5 \rightarrow 4s^1 3d^6$ promotion energy of 2.14 eV [4], Mn atoms do not bind strongly. As a result, Mn_2 is a weakly bound van der Waals dimer with reported bond dissociation energy ranging from 0.1 $\pm$ 0.1 to 0.56 $\pm$ 0.26 eV depending upon the different method of analysis [3]-[7]. This weak Mn− Mn bonding has been demonstrated through the photo-dissociation experiments for Mn_n^+ ($n \leq 7$) cluster cations [7, 100]. Consequently, the bulk α-Mn, which has a very complex lattice structure with 58 atoms in the unit cell, has the lowest binding energy among all the $3d$ transition metal elements.

Magnetic properties of manganese clusters are rather unusual. According to Hund's rule, the half-filled localized $3d$ electrons give rise to large atomic magnetic moment of 5 μ_B. An early electron spin resonance (ESR) study suggested a magnetic moment of 5 μ_B/atom for very small Mn clusters [101]. However, Stern-Gerlach (SG) molecular beam experiments on Mn_{5-99} clusters by Knickelbein recently revealed the net magnetic moments ranging from 0.4 to 1.7 μ_B/atom [26, 27] (see Fig.4.1). This differs both from the ferromagnetic (FM) small clusters and from the antiferromagnetic (AFM) bulk α-Mn. This experimental results can be explained either way that the individual atomic moments are small and ordered ferro-magnetically or the individual atomic moments remain large

(3) **Mukul Kabir**, Abhijit Mookerjee and D. G. Kanhere, *Magnetism in pure and doped manganese clusters*, Vol-4 pp 1018-1021 (Brill Academic Publishers, The Netherlands, 2005).

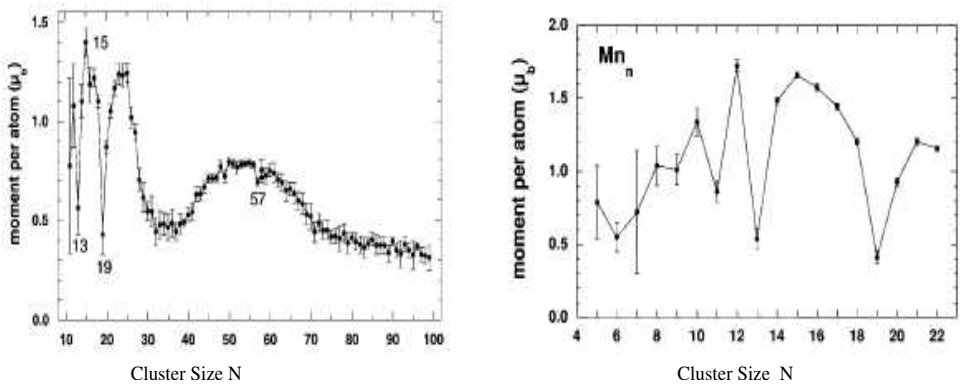

Figure 4.1: Plot of experimental magnetic moment as a function of clusters size N. This has been measured through the Stern-Gerlach cluster beam experiment by Knickelbein [26, 27]

.

but their orientation flips from site to site i.e., they are coupled ferri-magnetically. In the SG experiment, it is important to note the relative decrease in the magnetic moment for Mn_{13} and Mn_{19}, as well as the relatively very large experimental uncertainty in the measured magnetic moment for Mn_7 [26, 27]. In the present work, we will show that the local minima for Mn_{13} and Mn_{19} arise due to their 'closed' icosahedral structures, whereas, the large experimental uncertainty ($\pm$ 58 % of the measured value) in the magnetic moment of Mn_7 is plausibly due to the production of different magnetic isomers (in addition with statistical fluctuation) in the subsequent measurements.

Earlier all electron (AE) studies [102]-[104] found Mn$-$Mn FM ordering for Mn_n ($n >$ 4) clusters, which, in turn, is not consistent with the SG experiment. However, Nayak *et al.* first predicted ferrimagnetic ground state for Mn_{13} with a total magnetic moment of 33 μ_B [105]. In consistent with the SG experiments, very recent AE studies by Parvanova *et al.* [106, 107] (n =2-9, 12 and 13) and Jones *et al.* [108] (n = 5 and 6) reported ferrimagnetic ordering in Mn_n clusters. Briere *et al.* [109] used ultra-soft pseudo-potentials (US-PP) to study the intermediate size Mn_n clusters (n = 13, 15, 19 and 23) and found icosahedral structural growth with an exception for Mn_{15}. However, their predicted magnetic moments differ widely from the experimental values. This might be attributed to the reason that the US-PP may not be appropriate in describing the transition metals

with large magnetic moments. This will be discussed briefly later in the section 7.2. Our main motivation of this work is particularly driven by the SG experiments [26, 27]. Here we shall investigate − (i) The structural and magnetic evolution of Mn_n clusters, n=2-20. (ii) The sudden drop in the magnetic moment at n=13 and 19 and the very large experimental uncertainty in the measured magnetic moment for Mn_7, and (iii) The possible presence of isomers with different magnetic structures in the SG experimental molecular beam.

It has also been found by Parks *et al.* that the Mn_n clusters show a downward discontinuity in their reaction rate with molecular hydrogen at $n = 16$, and this was attributed to non-metal to metal transition in Mn_{16} [110]. But if this is indeed true then there should be a downward decrease in the ionization potential too. However, no such abrupt decrease has been seen in the measured ionization potential [111]. In this chapter, we discuss both the spin gaps to investigate this issue.

4.2 Computational Details

The calculations are performed using density functional theory (DFT), within the pseudopotential plane wave method. We have used projector augmented wave (PAW) method [59, 60] and Perdew-Bruke-Ernzerhof (PBE) exchange-correlation functional [48] for spin-polarized generalized gradient correction (GGA) as implemented in the Vienna *ab-initio* Simulation Package (VASP) [112]. The $3d$ and $4s$ electrons are treated as valence electrons and the wave functions are expanded in the plane wave basis set with the kinetic energy cut-off 337.3 eV. Reciprocal space integrations are carried out at the Γ point. Symmetry unrestricted geometry and spin optimizations are performed using conjugate gradient and quasi-Newtonian methods until all the force components are less than a threshold value 0.005 eV/Å. Simple cubic super-cells are used with the periodic boundary conditions, where two neighboring clusters are kept separated by at least 12 Å vacuum space. For each size, several initial geometrical structures have been considered. To get the ground state magnetic moment we have explicitly considered *all possible* spin configurations for each geometrical structure. For transition metals with large magnetic moments, the PAW method seems to be more appropriate (as good as the AE calculations) than the US-PP

approach [60]. The US-PP overestimates the magnetization energies and this overestimation is even more large for GGA calculations than local spin density approximation (LSDA). This is due to the fact that the GGA functionals are more sensitive to the shape of the wave functions than the LSDA functionals. However, the difference between these two methods, US-PP and PAW, are solely related to the pseudization of the augmentation charges in the US-PP approach, which can be removed by choosing very accurate pseudized augmentation function, which is then computationally expensive.

The binding energy per atom is calculated as,

$$E_b(\mathrm{Mn}_n) \;=\; \frac{1}{n}\left[E(\mathrm{Mn}_n) \;-\; n\;E(\mathrm{Mn})\right], \tag{4.1}$$

n being the size of the cluster. The local magnetic moment $\mathcal{M}$, at each site can be calculated as,

$$\mathcal{M} \;=\; \int_0^R \;\Big[\;\rho^{\uparrow}(\mathbf{r}) \;-\; \rho^{\downarrow}(\mathbf{r})\Big]\;\, d\mathbf{r}, \tag{4.2}$$

where $\rho^{\uparrow}(\mathbf{r})$ and $\rho^{\downarrow}(\mathbf{r})$ are spin-up and spin-down charge densities, respectively and R is the radius of the sphere centering the atom. For a particular cluster, R is taken such that no two spheres overlap i.e., R is equal to the half of the shortest bond length in that cluster.

4.3 Results and discussions

4.3.1 Small Ferromagnetic Clusters (Mn_2 - Mn_4)

Theory and experimental reports are in contradiction for the Mn_2 dimer. More than 30 years ago, Nesbet [113] calculated binding energy, bond length and magnetic moment of the dimer at the restricted Hartree-Fock (RHF) level and predicted an antiferromagnetic (AFM) ground state with bond length 2.88 Å. Later on, unrestricted Hartree-Fock calculation was done by Shillady *et al.* [114] and found a ferromagnetic (FM) ground state with total spin 10 μ_B and bond length 3.50 Å. The experiments based on resonant Raman spectroscopy [115] and ESR (Electron Spin Resonance) [116] predicted an AFM ground state with a bond length 3.4 Å. However, all DFT calculations [80, 104, 103, 117] within different levels of approximation and using different exchange-correlation functionals, pre-

dict a FM ground state with much smaller bond length, ~ 2.60 Å than the experimental bond length. A comparison among different levels of theory is given in the Table 4.1.

Table 4.1: Summary of binding energy (E_b), bond length (R_e) and magnetic moment (μ) of Mn_2 reported by various authors.

Authors	Method	E_b (eV)	R_e (Å)	μ (μ_B)
Nesbet [113]	RHF + Heisenberg exchange	0.79	2.88	0
Wolf and Schmidtke [118]	RHF		1.52	0
Shillady *et al.* [114]	UHF	0.08	3.50	10
Fujima and Yamaguchi [119]	LSDA	0.70	3.40	0
Harris and Jones [120]	LSDA	1.25	2.70	10
Salahub and Baykara [121]	LSDA	0.86	2.52	0
Nayak *et al.* [103]	All-electron + GGA (BPW91)	0.91	2.60	10
Parvanova *et al.* [117]	All-electron + GGA (PBE)	0.98	2.60	10
Kabir *et al.* [80]	Pseudopotential + GGA (PBE)	1.06	2.58	10
Pederson *et al.* [104]	All-electron + GGA	0.99	2.61	10
Experiment	ESR in rare-gas matrix [116]	0.1 ± 0.1	3.4	0

Due to the filled $4s$ and half-filled $3d$ electronic configuration, as well as high (2.14 eV) $4s^2\ 3d^5 \rightarrow 4s\ 3d^6$ promotion energy Mn atoms do not bind strongly as two Mn atoms come closer to form Mn_2 dimer, and as a result Mn_2 is very weakly bond van der Walls dimer, which is also evident from the low experimental value, 0.01 ± 0.1 — 0.56 ± 0.26 eV. However, no experimental results available in the gas-phase and all the experiments are done in the gas matrix, and therefore, it is quite possible that the Mn atoms interact with the matrix, which could stretch R_e and could lead to the AFM ground state.

From the Table 4.2, we see that R_e decreases monotonically as the net moment decreases. It is simply because the reduction of the atomic spacing leads to comparatively stronger overlap of the atomic orbitals which reduces the magnetic moment.

The case of Mn_3 is extremely interesting as it could have either FM or a frustrated AFM structure. We have studied triangular and linear structures. An equilateral triangular FM state with total moment 15 μ_B is found to be the ground state with bond lengths 2.74 Å and binding energy 0.82 eV/atom. The frustrated AFM state with total moment 5

Table 4.2: The binding energy and equilibrium bond length of Mn_2 dimer for all possible spins.

spin	Binding energy (eV)	Bond length
0 (AFM)	0.51	2.57
2	0.44	1.53
4	unbound	1.73
6	unbound	1.94
8	0.47	2.24
10	1.06	2.58

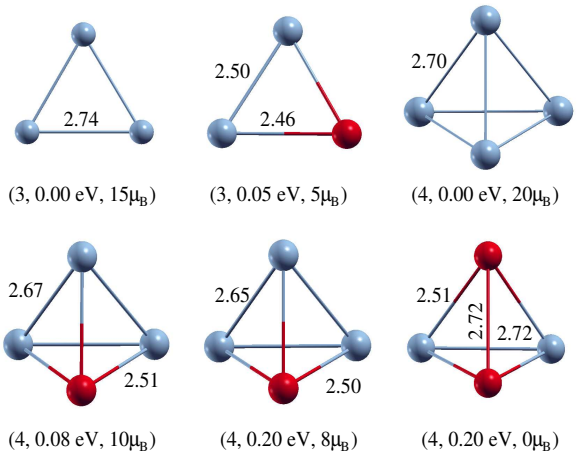

Figure 4.2: Atomic spin ordering of the ground state and low-lying isomers for Mn_3 and Mn_4 clusters. Numbers in the parenthesis represent number of atoms in the cluster, relative energy to the ground state and total magnetic moment, respectively. Bond lengths are given in Å. Blue (Gray) color represents up or positive and red (dark gray) represents down or negative magnetic moment. We will follow the same convention throughout.

μ_B is found to be nearly degenerate with the FM ground state (lies only 0.05 eV higher in energy). This has an isosceles triangular structure with one long and two short bond lengths of 2.50 and 2.45 Å, respectively (Fig.4.2). The resonance Raman spectra studies by Bier *et al.* [115] suggest the ground state to be Jahn-Teller distorted D_{3h} structure with an odd integer magnetic moment.

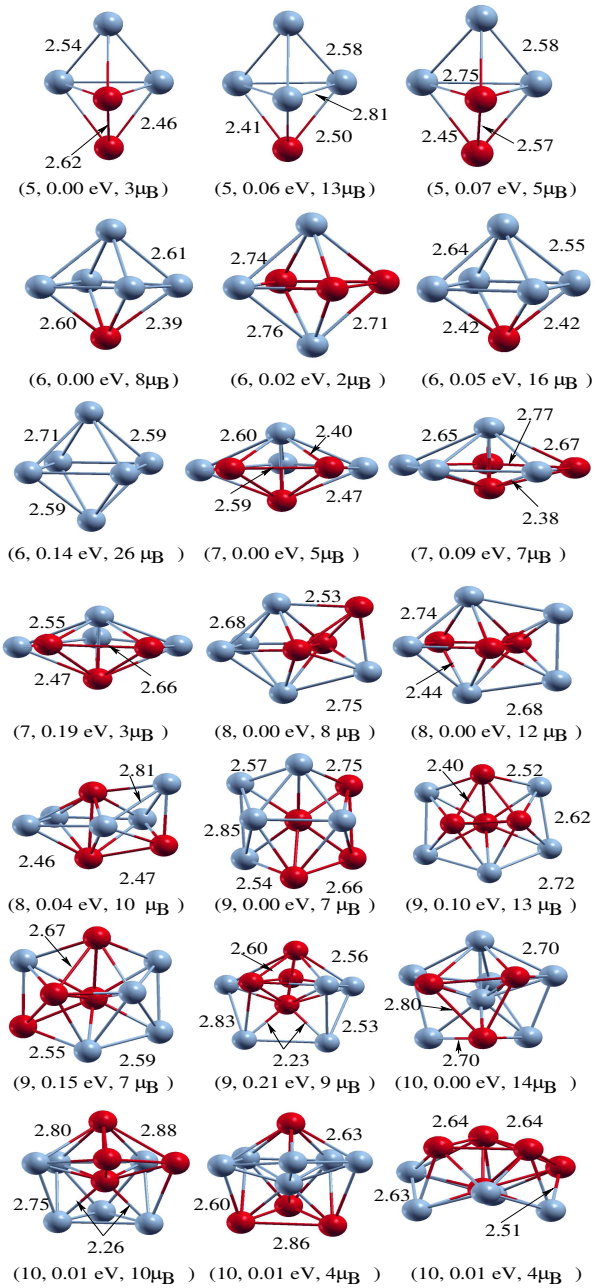

Figure 4.3: Atomic spin ordering of the ground and isomeric geometries for n = 5-10. Same ordering has been followed as in the Table 4.3.

For the Mn_4 cluster, we examined three different conformations: square, rhombus and tetrahedron. A perfect tetrahedral structure with bond lengths 2.7 Å and binding energy

1.18 eV/atom is the ground state, where Mn−Mn coupling is FM with total moment 20 μ_B (Fig.4.2). Three isomers are found and all of them are tetrahedral. A ferrimagnetic state with total moment 10 μ_B is only 0.08 eV higher in energy. Another ferrimagnetic state with total moment 8 μ_B is found to be degenerate with the AF state with no net moment and they are 0.20 eV higher in energy. In all these optimal structures the distances between two similar spins ($d_{\uparrow\uparrow}$ or $d_{\downarrow\downarrow}$) are larger than those of between two opposite spins ($d_{\uparrow\downarrow}$). Our results are consistent with the previous AE calculations [102]-[107]. Ludwig *et al.* [122] have studied Mn_4 in solid silicon and observed a 21-line hyperfine pattern that not only establishes the four atoms to be equivalent, but also the total moment to be 20 μ_B. However, the present results can not directly be compared with this experiment because of possible Si(matrix)-Mn interaction and there is no available report of magnetic ordering for Mn_4 in its gas phase.

4.3.2 Mn_5 - Mn_{10}

As the number of atoms in the cluster (n) increases the determination of the structural and magnetic ground state becomes a very delicate task as the number of local minima in the corresponding potential energy surface increases exponentially with n. Therefore, more than one geometric and/or magnetic structures of comparable stability are possible. In the Fig.4.3 we depict the atomic and magnetic structures for the ground state as well as for the closely lying isomers for the size range n = 5-10. As it is mentioned earlier, to hit the ground state more reliably, we have studied *all possible* spin multiplicities for several geometric structures for a particular cluster size n. Calculated binding energies, relative energies, magnetic moments and two spin gaps are given in the Table 4.3, Table 4.4 and Table 4.5 for the entire size range n = 2-20.

For the Mn_5 cluster, a square pyramid and a triangular bi-pyramid (TBP) were studied. Transition in the magnetic order, from FM to ferrimagnetic, is found. A ferrimagnetic TBP is found to be the ground state with total spin 3 μ_B. The next two isomers are also ferrimagnetic in nature with total spins 13 μ_B and 5 μ_B. Both of these structures also have TBP structure and lie 0.06 and 0.07 eV, respectively, higher in energy. The next lowest energy arrangement is FM and also has a TBP structure with total spin 23 μ_B

Table 4.3: Binding energy, relative energy to the GS ($\triangle E = E - E_{GS}$), magnetic moment (with a comparison to the SG experiment [26, 27]) and different spin gaps, $\triangle_1$ and $\triangle_2$, for Mn_n ($n = 3$—10) clusters.

Cluster	E_b (eV/atom)	$\triangle E$ (eV)	Magnetic Moment (μ_B/atom)		Spin Gaps (eV)	
			Theory	SG Exp. [26, 27]	δ_1	δ_2
Mn_3	0.82	0.00	5.00	–	0.73	1.27
	0.81	0.05	1.67		0.63	0.58
Mn_4	1.18	0.00	5.00	–	0.66	2.35
	1.16	0.08	2.50		0.45	0.85
	1.13	0.20	0.00		0.41	0.41
	1.13	0.20	2.00		1.12	0.21
Mn_5	1.41	0.00	0.60	0.79 ± 0.25	1.03	0.30
	1.40	0.06	2.60		0.97	0.37
	1.40	0.07	1.00		0.16	0.65
	1.37	0.19	4.60		0.55	0.77
Mn_6	1.57	0.00	1.33	0.55 ± 0.10	0.48	0.35
	1.56	0.02	0.33		0.40	0.31
	1.56	0.05	2.67		0.86	0.32
	1.54	0.14	4.33		0.98	1.16
Mn_7	1.73	0.00	0.71	0.72 ± 0.42	0.45	0.65
	1.71	0.09	1.00		0.56	0.23
	1.70	0.19	0.43		0.51	0.13
Mn_8	1.77	0.00	1.00	1.04 ± 0.14	0.61	0.20
	1.77	0.00	1.50		0.40	0.41
	1.77	0.04	1.25		0.35	0.25
Mn_9	1.87	0.00	0.78	1.01 ± 0.10	0.49	0.36
	1.86	0.10	1.44		0.24	0.60
	1.85	0.15	0.78		0.30	0.34
	1.84	0.21	1.00		0.24	0.36
Mn_{10}	1.94	0.00	1.40	1.34 ± 0.09	0.27	0.44
	1.94	0.01	1.00		0.69	0.13
	1.94	0.01	0.40		0.36	0.41
	1.94	0.01	0.40		0.37	0.20

and lies 0.19 eV higher in energy. Our results are in agreement with the very recent AE calculations [106] -[108]. However, previously the FM ground state was predicted by both Nayak *et al.* [102, 103] and Pederson *et al.* [104]. In the recent SG experiment [27], magnetic moment was found to be 0.79±0.25 μ_B/atom, which is very close to our predicted value 0.60 μ_B/atom for the ground state.

We have investigated both the octahedral and the capped trigonal bi-pyramid for Mn_6 cluster. A ferrimagnetic octahedral structure with total spin 8 μ_B is found to be the ground state with binding energy 1.57 eV/atom. Another octahedral ferrimagnetic isomer with total moment 2 μ_B is nearly degenerate (0.02 eV higher in energy). The next isomer is also a ferrimagnetic octahedra, which possess a total moment of 16 μ_B and lies 0.05 eV higher. The next favorable isomer is FM and has a total moment 26 μ_B and is 0.14 eV higher than the ground state. In an earlier calculation, Pederson *et al.* [104] predicted a FM octahedral structure with moment 4.33 μ_B/atom to be the ground state. However, in agreement with the recent AE-DFT calculations [106]-[108], present calculation predicts the same ground state and isomers. Experimentally measured magnetic moment 0.55 ± 0.10 μ_B/atom [27] lies between that of our predicted ground state, 1.33 μ_B/atom and the first isomer, 0.33 μ_B/atom, which are almost degenerate. It is possible that in the SG experimental beam, multiple isomers were produced such that the measured value is almost an average of the ground state and the first isomer.

We have considered pentagonal bi-pyramid (PBP), capped octahedron and bi-capped trigonal pyramid as the possible candidates for the ground state of Mn_7. The most stable configuration is a PBP structure with ferrimagnetic spin ordering, which has a total moment 5 μ_B. The next two closest isomers also have ferrimagnetic arrangements with 7 μ_B and 3 μ_B total moments and they lie 0.09 eV and 0.20 eV higher than the ground state, respectively. Our ground state magnetic moment agrees with the earlier calculations [106, 107, 123], though we predict isomers with different spin arrangements. However, Pederson *et al.* predicted a FM ground state [104]. Present ground state magnetic moment per atom exactly matches with the experimental value, 0.72 ± 0.42 μ_B/atom [27]. We would like to note the rather large uncertainty here. We argue that the plausible presence of these isomers, with total moments 7 μ_B and 3 μ_B along with the ground state (5 μ_B), in the SG beam might lead to this high uncertainty in the measured

value.

Motivated by our study on Cu_8 [124, 125], (which have been discussed in the chapter 3), we investigated three different geometries for Mn_8, viz, capped pentagonal bi-pyramid (CPBP), bi-capped octahedron (BCO) and tri-capped trigonal bi-pyramid (TCTBP). The BCO structure with total moments 8 μ_B and 12 μ_B are found to be degenerate ground state. Another BCO structure with total moment 10 μ_B lies only 0.03 eV higher in energy. The SG cluster beam experiment has reported a magnetic moment of 1.04 ± 0.14 μ_B/atom [27], which is nearly an average of our predicted values. Therefore, our present DFT study together with the experiment in turn indicate the possible presence of these three isomers in the experimental beam with almost equal statistical weight. The optimal CPBP and TCTBP structures have total moments 14 μ_B and 12 μ_B, respectively and they lie 0.31 and 0.4 eV higher than the ground state. Parvanova *et. al.* [107] found CPBP structure to be the most stable, however, their predicted magnetic moment is very small, 4 μ_B, compared to both of our value and the SG experiment. Pederson *et. al.* [104] predicted a FM BCO structure with moment 32 μ_B as the ground state. The optimal FM structure for all the three geometrical structures have total moment 32 μ_B and lie 1.01, 0.63 and 1.17 eV higher in energy compare to their respective optimal ferrimagnetic structure, respectively for BCO, CPBP and TCTBP structures.

For the Mn_9 cluster, as initial configuration we took three stable isomers found for Cu_9 [124, 125] and a capped and a centered anti-prism structure. The optimal structure is a centered anti-prism structure with total moment 7 μ_B, which is in very good agreement with the experimental value 1.01 ± 0.10 μ_B/atom [27]. The local magnetic moment $\mathcal{M}$ (as calculated form the equation 4.2) shows strong environment dependency due to the anisotropy in bonding. The $\mathcal{M}$ of the highly coordinated central atom is very small, -0.22 μ_B, whereas those of the surface atoms are quite high and lie between 3.45 and 3.75 μ_B. Parvanova *et al.* [107] have found a similar structure but with different spin configuration with total moment 9 μ_B to be the optimal structure. The next two isomers have the same geometry and have 13 and 7 μ_B total magnetic moment (Fig.4.3 and Table 4.3). The next isomer is a bi-capped pentagonal bi-pyramid, which lies 0.21 eV higher with a total moment of 9 μ_B. The optimal capped anti-prism structure lies 0.23 eV higher and has a total moment of 7 μ_B. Note that, all these structures have 5 spin-up ($N_\uparrow$) atoms and 4

Table 4.4: Binding energy, relative energy to the GS ($\triangle E = E - E_{GS}$), magnetic moment (with a comparison to the SG experiment [26, 27]) and different spin gaps, $\triangle_1$ and $\triangle_2$, for Mn_n ($n = 11$—15) clusters.

Cluster	E_b (eV/atom)	$\triangle E$ (eV)	Magnetic Moment (μ_B/atom)		Spin Gaps (eV)	
			Theory	SG Exp. [26, 27]	δ_1	δ_2
Mn_{11}	1.99	0.00	0.82	0.86 ± 0.07	0.26	0.29
	1.98	0.11	0.46		0.34	0.20
	1.98	0.15	0.64		0.10	0.45
Mn_{12}	2.08	0.00	1.33	1.72 ± 0.04	0.48	0.26
	2.08	0.05	0.33		0.40	0.30
	2.07	0.11	1.50		0.05	0.45
Mn_{13}	2.17	0.00	0.23	0.54 ± 0.06	0.34	0.38
	2.16	0.08	0.54		0.36	0.20
Mn_{14}	2.17	0.00	1.29	1.48 ± 0.03	0.23	0.24
	2.17	0.02	1.43		0.24	0.31
	2.17	0.05	1.57		0.25	0.32
Mn_{15}	2.23	0.00	0.87	1.66 ± 0.02	0.36	0.27
	2.23	0.03	0.33		0.16	0.29
	2.23	0.06	0.47		0.20	0.23
	2.23	0.06	0.87		0.27	0.36
	2.23	0.06	1.00		0.25	0.45
	2.21	0.28	0.47		0.39	0.35

spin-down ($N_\downarrow$) atoms.

Different tri-capped pentagonal bi-pyramidal structures along with different tetra capped octahedral structures were tried as initial structures for Mn_{10}. Four isomers exist with almost the same energy. They lie within ~ 0.01 eV energy (see Table 4.3 and Fig. 4.3). All of these have a pentagonal ring and could be derived by removing 3 atoms from a 13-atom icosahedra. Ground state has a total magnetic moment 14 μ_B, which is very close to the SG experimental value, 1.34 ± 0.09 μ_B/atom [27].

Table 4.5: Binding energy, relative energy to the GS ($\triangle E = E - E_{GS}$), magnetic moment (with a comparison to the SG experiment [26, 27]) and different spin gaps, $\triangle_1$ and $\triangle_2$, for Mn_n (n = 16—20) clusters.

Cluster	E_b (eV/atom)	$\triangle E$ (eV)	Magnetic Moment (μ_B/atom)		Spin Gaps (eV)	
			Theory	SG Exp. [26, 27]	δ_1	δ_2
Mn_{16}	2.27	0.00	1.25	1.58 ± 0.02	0.33	0.22
	2.27	0.02	1.38		0.19	0.52
	2.27	0.06	0.63		0.28	0.35
	2.27	0.10	0.50		0.30	0.20
Mn_{17}	2.33	0.00	1.59	1.44 ± 0.02	0.25	0.37
	2.32	0.08	1.47		0.25	0.09
	2.32	0.09	1.71		0.14	0.70
Mn_{18}	2.35	0.00	1.67	1.20 ± 0.02	0.36	0.30
	2.35	0.02	1.56		0.34	0.33
	2.35	0.02	1.44		0.35	0.25
	2.35	0.06	1.78		0.18	0.55
Mn_{19}	2.37	0.00	1.10	0.41 ± 0.04	0.19	0.22
	2.37	0.01	1.00		0.24	0.16
	2.37	0.08	0.47		0.22	0.15
Mn_{20}	2.37	0.00	1.40	0.93 ± 0.03	0.39	0.19
	2.37	0.00	1.50		0.21	0.20
	2.37	0.05	1.60		0.12	0.35
	2.37	0.07	0.80		0.30	0.21

4.3.3 Intermediate size clusters: Mn_{11} - Mn_{20}

All the intermediate sized clusters with n = 11-20 are found to adopt an icosahedral growth pattern. The ground state structures and the few isomers along with their corresponding spin arrangements are shown in the Fig.4.4. An icosahedral structure without one apex atom is found to be the ground state for the Mn_{12} cluster. This structure has $N_\uparrow = 8$ and $N_\downarrow = 4$ spin configuration with a total moment of 16 μ_B. This value is close to the experimentally measured value of 1.72 ± 0.04 μ_B/atom [26, 27]. Recently Parvanova *et*

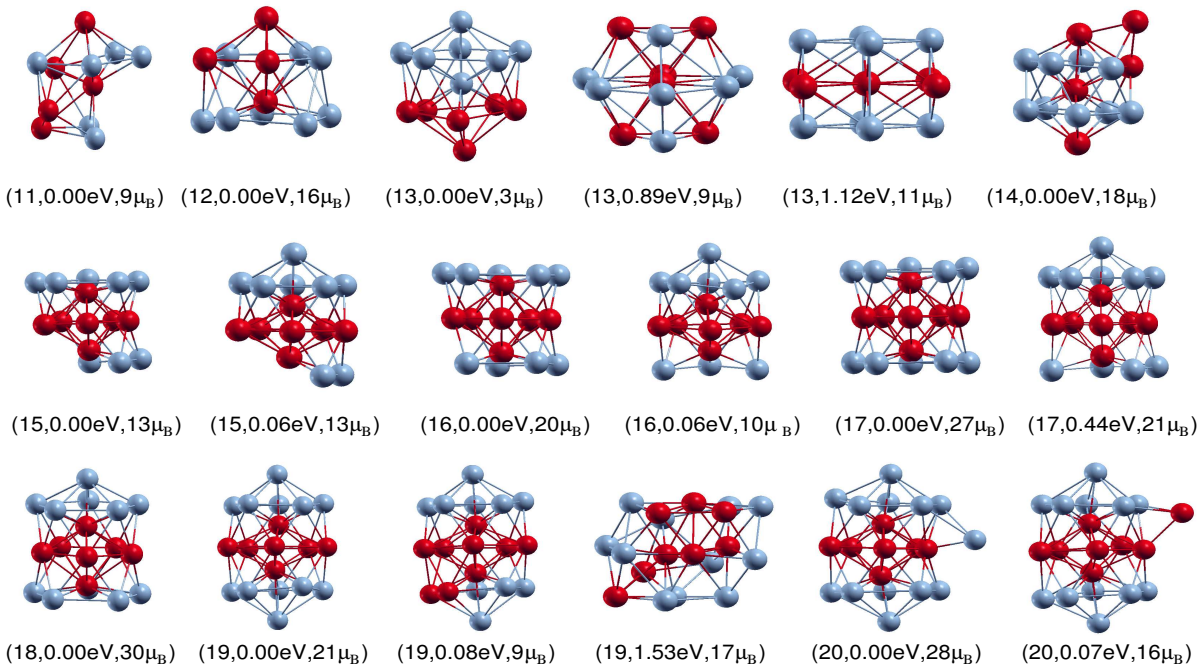

Figure 4.4: The ground state and a few higher energy structures for the size range $n = 11 - 20$. Note the grouping of the same kind of spins.

al. predicted the same geometrical structure but with comparatively smaller, 1 μ_B/atom, magnetic moment [107]. We have found two closely lying isomers, which have the same geometrical structure with total moments 4 μ_B and 18 μ_B (Table 4.4). Another possible icosahedral structure without the central atom lies much higher in energy.

The obvious candidates for the Mn_{13} cluster are the icosahedral, hexagonal close packed (HCP) and cub-octahedral structures. The variation of total energy as a function of the total magnetic moment is plotted in the Fig.4.5 for all these three conformations. The icosahedral structure is found to be the ground state with $N_\uparrow = 7$ spin structure. The two pentagonal rings are AFM coupled for this structure (Fig.4.4). Consequently, the magnetic moment is found to be small, 0.23 μ_B/atom. This predicted magnetic moment is much smaller than those of its neighboring Mn_{12} and Mn_{14} clusters (Fig.4.7), what has been indeed predicted by the SG experiment [26, 27]. Although, the present value is much lower than the experimental value of 0.54 $\pm$ 0.06 μ_B/atom [27]. However, we have found another icosahedral isomer with magnetic moment exactly the same with the

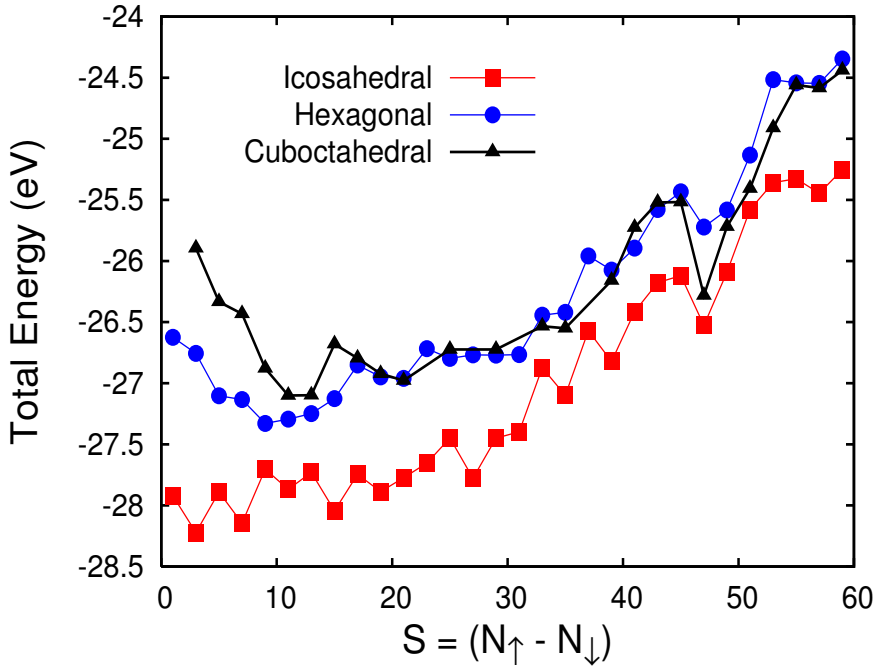

Figure 4.5: Plot of the total energy as a function of total magnetic moment $S(= N_\uparrow - N_\downarrow)$ for icosahedral, hexagonal closed pack and cub-octahedral conformations for Mn_{13} cluster.

experimental value, which lies only 0.08 eV higher in energy (Table 4.4). This structure also has $N_\uparrow = 7$. Recently, Parvanova *et al.* predicted similar magnetic ordering [107]. The optimal HCP and cub-octahedral structures (Fig.4.4) have relatively higher magnetic moments 9 μ_B ($N_\uparrow = 7$) and 11 μ_B ($N_\uparrow = 8$) , respectively, and they lie much higher in energy, 0.89 eV and 1.12 eV, respectively. Nayak *et al.* first predicted a ferrimagnetic state for Mn_{13}. However, their predicted magnetic moment is quite high (33 μ_B): all the surface atoms are anti-ferromagnetically coupled with the central atom [105].

The ground state of Mn_{14} is the first complete icosahedra with a single atom capping. This structure has $N_\uparrow = 9$, with a magnetic moment 1.29 μ_B/atom. In this structure the magnetic coupling between the two pentagonal rings is FM, which was coupled anti-ferromagnetically in the case of Mn_{13} and consequently, it has small magnetic moment. The next two isomers lie very close to the ground state: they lie only 0.02 eV and 0.05 eV higher and have 1.43 and 1.57 μ_B/atom magnetic moment, respectively. These two

isomers (not shown in Fig.4.4) have the same $N_\uparrow = 9$ spin structure, but with their different positional arrangement. The experimentally predicted magnetic moment, 1.48 $\pm$ 0.03 μ_B/atom, is an average of the ground state and the two isomers (Table 4.4), which again indicates that these isomers might be produced along with the ground state in the SG experiment.

The discrepancy between the present theoretical and experimental magnetic moment is rather large for Mn_{15}. The present value is 0.87 μ_B/atom, whereas the corresponding experimental value is 1.66 $\pm$ 0.02 μ_B/atom. We have also found several isomers (Table 4.4), but none of them are close to the experimental value. The ground state and all the closely lying isomers within $\sim$ 0.1 eV energy spacing are of derived icosahedral structure. The two competing icosahedral structures with 5,1,5,1,3 and 1,5,1,5,1,2 staking (i.e. without or with the apex atom) are possible (Fig.4.4). The first kind of structure is found to be the ground state, whereas the optimal structure for the second kind lies 0.06 eV higher with a magnetic moment 13 μ_B (Fig.4.4). Another structure of the second kind is found to be degenerate with this isomer, which has a magnetic moment 7 μ_B (Table 4.4). However, using US-PP Briere *et al.* found a body-centered cubic structure to be the ground state with much smaller magnetic moment, 0.20 μ_B/atom [109]. In the present case this body-centered cubic kind of structure lies 0.28 eV higher (Table 4.4).

The same structural trend is observed in the case of Mn_{16}, the two different competing geometries have been found to be the possible candidates for the Mn_{16} cluster. Both of these structures can be derived from the 19-atom double icosahedra, which has a 1,5,1,5,1,5,1-atomic staking. The ground state has a magnetic moment 1.25 μ_B/atom with $N_\uparrow = 9$ spin structure. This structure has 5,1,5,1,4-atomic staking: both the apex atoms and one atom from the lower pentagonal ring are missing from the double icosahedra. The next isomer has the same atomic arrangement and is almost degenerate, which lies only 0.02 eV higher. This has 1.38 μ_B/atom magnetic moment and the same ($N_\uparrow = 9$) spin ordering. For both of these structures the central pentagonal ring is anti-ferromagnetically coupled with the upper and lower (incomplete) pentagonal ring. The experimentally predicted value, 1.58 $\pm$ 0.02 μ_B, [26, 27] is very close to these predicted values and confirms the corresponding ground state to be really of this 'strange' staking. The next two isomers have a different icosahedral geometry and have comparatively smaller magnetic

moment, 0.63 (Fig. 4.4) and 0.50 μ_B/atom. They lie 0.06 and 0.1 eV higher, respectively. Both of them have 1,5,1,5,1,3 staking, i.e. the 13-atom icosahedra is complete. The two complete pentagonal rings are anti-ferromagnetically coupled. All these structures have same number of $N_\uparrow$ and $N_\downarrow$ but have two different class of atomic arrangements, which is consequently the reason for their large difference in the magnetic moment.

The Mn_{17} cluster follows the same structural trend seen in both Mn_{15} and Mn_{16}. The ground state is a double icosahedra without both the apex atoms, i.e. it has 5,1,5,1,5 staking. The spin structure is $N_\uparrow = 10$ and the central pentagonal ring is AFM coupled with the other rings. This structure has a magnetic moment of 1.59 μ_B/atom, which is in excellent agreement with the experiment, 1.44 $\pm$ 0.02 μ_B/atom [27]. The next two isomers also have the same conformation as well as the same spin structure. For this size the structure of the second kind i.e. the icosahedral structure with one apex atom (Fig.4.4) lies rather higher in energy. To our knowledge, there is no available report for any other elements where this kind of staking has been observed to be the ground state for $Mn_{15} - Mn_{17}$ clusters.

The Mn_{18} is the 19-atom double icosahedra without one apex atom. The predicted magnetic moment is 1.67 μ_B/atom, whereas the experimental value is slightly smaller, 1.20 $\pm$ 0.02 μ_B/atom [27]. Next two isomers are nearly degenerate and have 1.56 and 1.44 μ_B/atom magnetic moment (Table 4.5). For all these structures the integrated magnetization densities $\mathcal{M}$ for the central pentagonal bi-pyramid are negative (Fig. 4.4).

The double icosahedral conformation is found to be the ground state for Mn_{19}. The predicted magnetic moment is 1.10 μ_B/atom (Fig. 4.4), which is smaller than those of its neighboring clusters, what has been predicted by the experiment [26, 27]. Another magnetic structure has been found to be degenerate with 1 μ_B/atom magnetic moment (not shown in Fig. 4.4). Both of the structures have $N_\downarrow = 7$ and the central pentagonal ring is AFM coupled with the other two rings. However, the predicted magnetic moment is larger than the experimentally measured value, 0.41 $\pm$ 0.04 μ_B/atom [27]. In our case a magnetic structure with a magnetic moment 0.47 μ_B/atom ($N_\downarrow = 9$), which is very close to the experimentally measured value, lies only 0.08 eV higher in energy (Fig 4.4). The optimal FCC structure lies much higher, 1.53 eV, in energy, which is shown in Fig. 4.4.

Two degenerate ground states have been found with 1.40 and 1.50 μ_B/atom magnetic

moment for Mn_{20} cluster. Both the structures have $N_{\downarrow} = 7$ (Fig. 4.4) spin configuration and the conformation can be seen as a singly capped 19-atom double icosahedra. The central pentagonal ring is anti-ferromagnetically coupled with the other two rings. The predicted ground state magnetic moment is larger than the experimental value, 0.93 $\pm$ 0.03 μ_B/atom [27]. However, a different spin structure ($N_{\downarrow} = 8$) with magnetic moment 0.80 μ_B/atom, which is close to the experimentally predicted value, lies only 0.07 eV higher (Fig. 4.4).

In the intermediate size range, the grouping of like spin atoms i.e spin segregation occurs (Fig. 4.4). For a particular sized cluster, we find that the ferromagnetically aligned atoms have longer average bond lengths than those of the anti-ferromagnetically aligned ones. This is because of the Pauli repulsion.

4.3.4 Binding Energies

The size dependence of the ground state binding energy for Mn_n clusters (n =2-20) is shown in Fig. 4.6. Due to the lack of hybridization between the half-filled $3d$ and filled $4s$ states and due to high $4s^2 3d^5 \rightarrow 4s^1 3d^6$ promotion energy, the Mn_2 dimer is a weakly bound dimer, which is a characteristic of van der Waals bonding [3]-[6]. As the number of atoms in the cluster increases, the binding energy increases monotonically due to the increase in the $s - d$ hybridization. However, it remains weak as compared to the other transition metal clusters in the same size range. This weak bonding has been demonstrated through the photo-dissociation experiments for Mn_n^+ ($n \leq 7$) cluster cations [7, 100]. However, the situation is improved [126] when an As-atom is doped to the Mn_n clusters, the binding energies of the resultant Mn_nAs clusters increase substantially due to their hybridized $s - d$ electrons bond with the p electrons of As. This would be discussed in detail in the chapter 6. Similar enhancement in bonding has also been seen due to the single nitrogen doping [127].

Upon extrapolation of the linear fit to the binding energy per atom data to $1/n \rightarrow 0$ (Fig.4.6(a)), we obtained the binding energy for an infinitely large cluster as 2.80 eV, which is very close to the experimental AF bulk α-Mn (2.92 eV). It is important here to note the kinks observed at $n = 7$ and 13 in the binding energy curve (Fig.4.6). These kinks

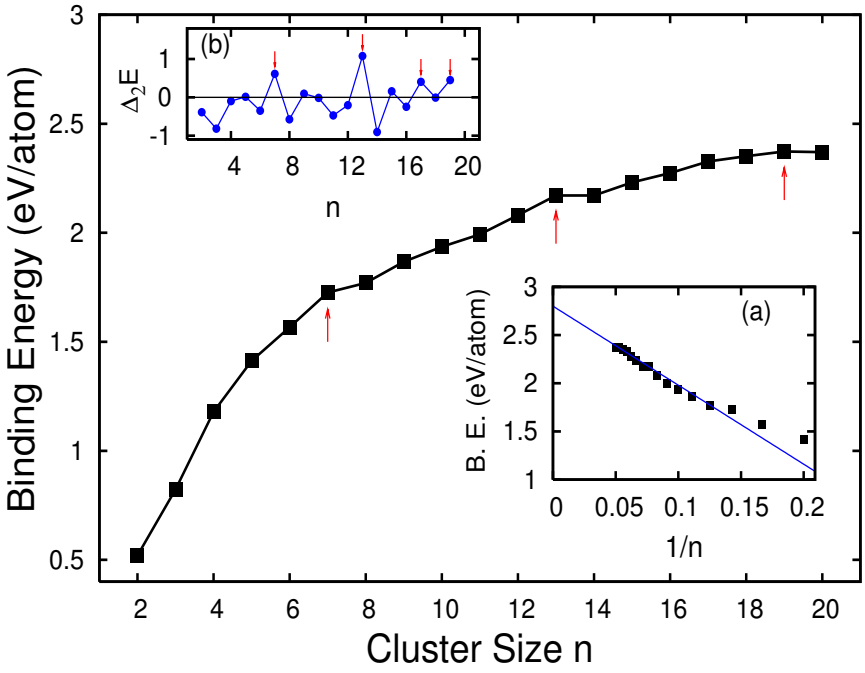

Figure 4.6: Plot of binding energy per atom as a function of cluster size n for the entire size range $2 \leq n \leq 20$. (a) Plot of the same as a function of $1/n$ for the ferrimagnetic clusters, $5 \leq n \leq 20$ and a linear fit (B.E. $= -8.20\frac{1}{n} + 2.80$) to the data. (b) Plot of second difference, $\Delta_2 E$ in energy, which represents the relative stability.

represent enhanced stability rendered by their 'closed' geometric structures: Mn_7 is PBP and Mn_{13} is the first complete icosahedra. If this argument is valid then there should also be a kink at $n = 19$, due to the fact it has double icosahedral structure. But we do not see any prominent kink in the binding energy curve. So, it will be interesting to investigate the second difference in the binding energy, $\Delta_2 E(n) = E(n+1) + E(n-1) - 2E(n)$, where $E(n)$ represents the total energy of an $n-$atom cluster. As $\Delta_2 E(n)$ represents stability of the corresponding cluster compared to its neighbors, the effect will be prominent. $\Delta_2 E$ is plotted in the Fig.4.6(b), where we see a peak for Mn_{19} too along with $n = 7$ and 13. However, in addition, without any a priory reason, we observe another peak at $n = 17$, which does not have 'closed' structure (a double icosahedra without two apex atoms).

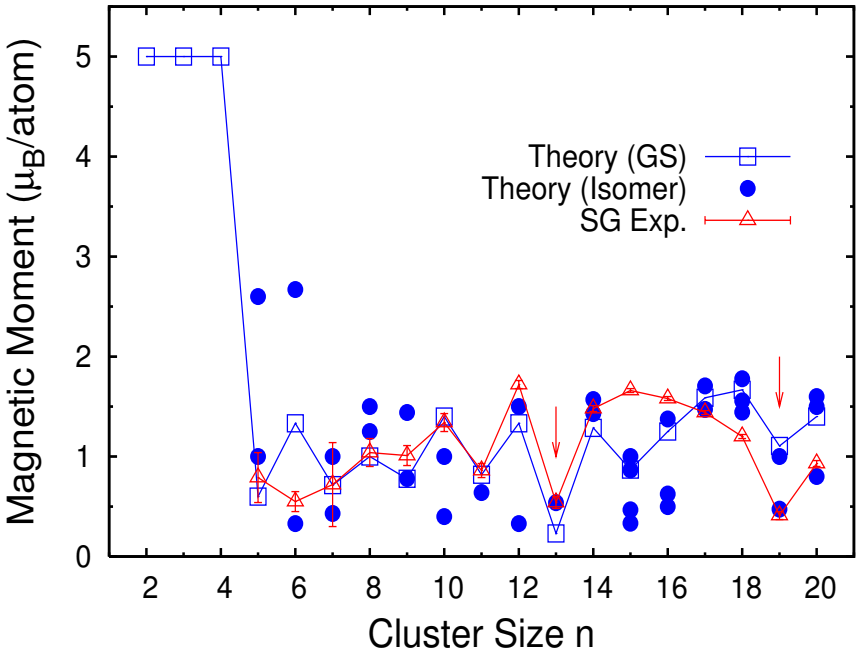

Figure 4.7: Size dependent variation of magnetic moment. For the size range 5 $\leq n \leq$ 20, it shows excellent agreement with the SG experiment. Isomers which lie very close to the corresponding GS energy are also shown.

4.3.5 Transition in magnetic ordering

For very small clusters, $n \leq$4, the magnetic coupling is found to be FM with magnetic moments 5 μ_B/atom, which is the Hund's rule value for an isolated Mn atom. Although we see that for Mn_3 cluster the FM solution is nearly degenerate with the frustrated AFM solution. The size dependence of the magnetic moment per atom is plotted in the Fig.4.7. We see the transition in the magnetic coupling (from FM to ferrimagnetic) takes place at $n = 5$ and the ferrimagnetic states continue to be the ground state for the entire size range n =5-20. Fig.4.7 shows a very good agreement between experimentally measured and our predicted magnetic moments. It was seen in the SG experiment that the experimental uncertainty in measuring the magnetic moment decreases with the cluster size. However, this is not the case for Mn_7, for which the measured uncertainty is quite large (0.72$\pm$0.42 μ_B, $\pm$58% of the measured value) as compared to the neighboing sizes. This large uncertainty might arise from the presence of isomers with different magnetic

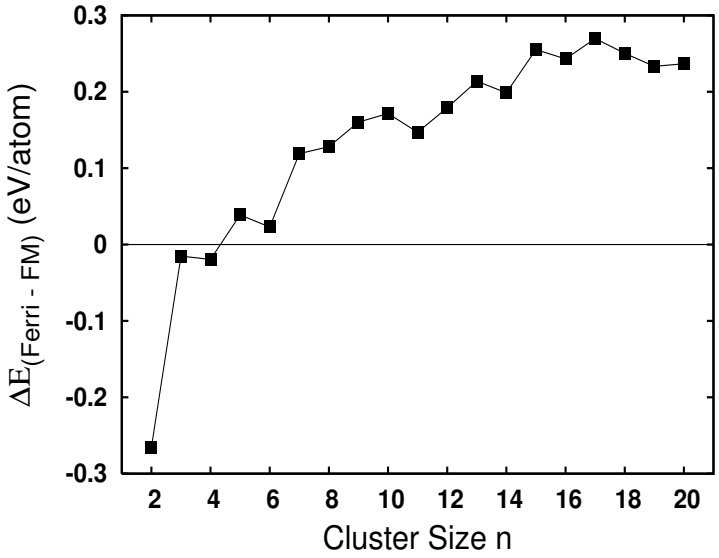

Figure 4.8: Plot of $\triangle E_{(\mathrm{Ferri-FM})}$ as a function of cluster size n.

moments in the SG beam for subsequent measurements. However, in addition with the statistical fluctuation, the above explanation only stands for a plausible reason as for all other sizes we did find many isomers with different magnetic moments (see Table 4.3 and Fig.4.7), but the corresponding experimental uncertainty is not that large. One another striking feature observed in the experiment is the sudden decrease in the magnetic moment at n=13 and 19, compared to their neighbors. Our calculation reproduces this feature. This is attributed to their 'closed' icosahedral structures: first complete icosahedra for Mn_{13} and a double icosahedra for Mn_{19}. The other geometries studied viz. hexagonal closed packed and cub-octahedral structures for Mn_{13} and a face-centered cubic structure for Mn_{19} lie much higher in energy, 0.89 eV (9 μ_B), 1.12 eV (11 μ_B) and 1.53 eV (17 μ_B), respectively, than their corresponding ground state.

In the Fig.4.7 we have depicted the magnetic moments of the very closely lying isomers with their ground state (see Table 4.3, Table 4.4, and Table 4.5) and while comparing those with the experimentally observed values, we come to the conclusion that for a particular size of cluster, the isomers with different magnetic moments are likely to be present in the SG cluster beam with a statistical weight and essentially, the measured moment is the weighted average of those isomers. We calculate the energy difference between the

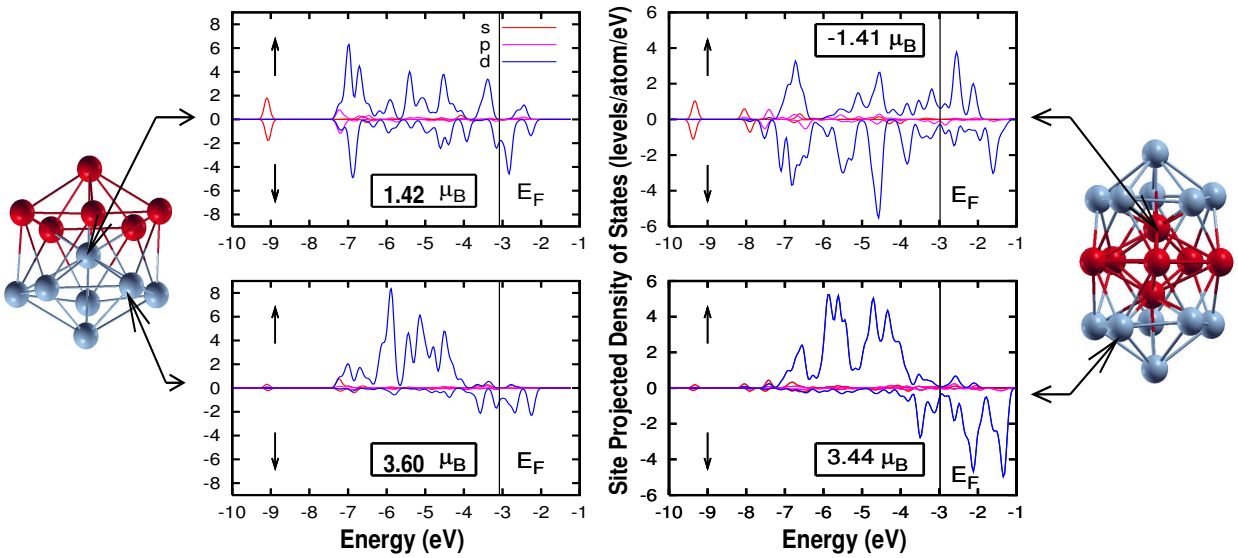

Figure 4.9: The *s*-, *p*- and *d*-projected density of states for the central and surface atoms for Mn_{13} and Mn_{19} in their ground state. Gaussian broadening of half-width 0.1 eV has been used. Integrated magnetization density $\mathcal{M}$ for each atom is given in the box.

optimal FM and optimal ferrimagnetic solutions, $\triangle E_{(\text{Ferri}-\text{FM})} = E(\text{Ferri}) - E(\text{FM})$, and plot them as a function of cluster size n in the Fig.4.8. For both Mn_3 and Mn_4 the FM solutions are slightly lower in energy than those of their respective optimal ferrimagnetic solutions, whereas the optimal FM solutions are slightly higher than the corresponding ferrimagnetic ground states for Mn_5 and Mn_6. Thereafter, as the cluster size increases, this energy difference, $\triangle E_{(\text{Ferri}-\text{FM})}$, increases almost monotonically indicating that the optimal FM solutions become more and more unlikely. All these optimal FM states have $\sim 4\ \mu_B$/atom magnetic moments.

4.3.6 Coordination and the *d*-electron localization

The angular momentum projected local density of states (LDOS) show interesting site dependency. The *s*-, *p*- and *d*-projected LDOS for the central and surface atoms are plotted in the Fig.4.9 for the Mn_{13} and Mn_{19} clusters. We see only *d*-projected LDOS are significant and are of great interest here. The *d*-projected LDOS of both Mn_{13} and Mn_{19}

for the central atoms are broad for both majority and minority spin states, which are also reflected through their small values of the integrated spin densities $\mathcal{M}$ (1.42 and -1.41 μ_B for Mn_{13} and Mn_{19}, respectively). The broadening occurs due to the high coordination of the central atom. On the other hand, the *d*-projected LDOS of the surface atoms are rather localized and the majority spins are nearly fully occupied, which is in agreement with the relatively large local magnetic moments of the surface atoms (3.60 and 3.44 μ_B for Mn_{13} and Mn_{19} , respectively).

4.3.7 Spin gaps: Nonmetal − metal transition?

A spin arrangement in any magnetic clusters is magnetically stable only if both the spin gaps,

$$\begin{aligned} \delta_1 &= -\left[\epsilon_{\text{HOMO}}^{\text{majority}} - \epsilon_{\text{LUMO}}^{\text{minority}}\right] \\ \delta_2 &= -\left[\epsilon_{\text{HOMO}}^{\text{minority}} - \epsilon_{\text{LUMO}}^{\text{majority}}\right], \end{aligned} \tag{4.3}$$

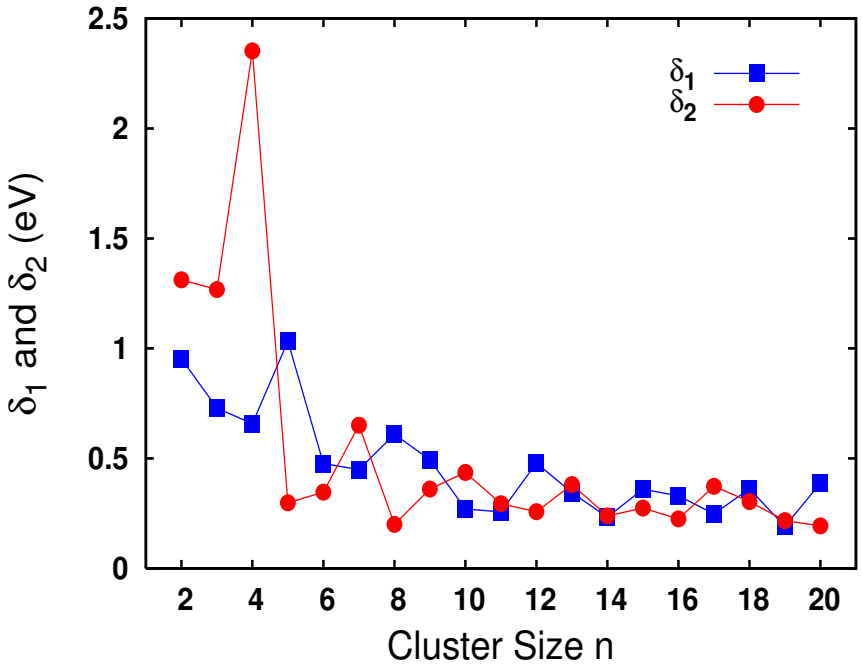

Figure 4.10: Plot of spin gaps as a function of cluster size n. See Table 4.3, Table 4.4 and Table 4.5 for the numerical values.

are positive, i.e. the lowest unoccupied molecular orbital (LUMO) of the majority spin lies above the highest occupied molecular orbital (HOMO) of the minority spin and vice versa. We find these two spin gaps to be positive for all the clusters (Table 4.3, Table 4.4 and Table 4.5) discussed here and are plotted in the Fig.4.10. The δ_1 and δ_2 have local structures, but generally decreases slowly as the coordination increases with cluster size. Parks *et al.* found that the Mn_n clusters with $n \leq 15$ are not reactive toward molecular hydrogen, whereas they form stable hydrides at and above $n = 16$, and the reaction rate varies considerably with the cluster size [110]. They argued it to be attributed from the non-metal to metal transition at $n = 16$. If this is indeed the reason, it is likely that the ionization potential would show a significant decrease at Mn_{16}, similar to what has been observed for free mercury clusters [128]. Therefore, we expect closing up of the spin gaps at $n = 16$. However, Koretsky *et al.* observed no sudden decrease in the measured ionization potential [111] and we do not find any spin gap closing at Mn_{16} either. The spin gaps have reasonable value, $\delta_1 = 0.33$ eV and $\delta_2 = 0.22$ eV for Mn_{16} cluster (Fig.4.10 and Table 4.5). This abrupt change in the reaction rate with H_2 at Mn_{16} is not due to any structural change either, as we find all the medium sized clusters adopt icosahedral growth pattern and the reason for the observed change in the reaction rate remains unknown.

4.4 Summary and Conclusions

We have systematically investigated the structural, electronic and magnetic properties of Mn_n (n = 2-20) clusters from the first-principles density functional theory. An extensive search have been made to locate the global minima. Due to the intrinsic $4s^2\ 3d^5$ electronic structure and high $4s^2 3d^5 \rightarrow 4s^1 3d^6$ promotion energy Mn-atoms do not bind strongly when they come closer to form a cluster. However, binding energy increases with the cluster size as the coordination number increases and reaches a value 2.37 eV/atom for Mn_{20}, which is 81 % of the bulk value. A magnetic transition from FM to ferrimagnetic ordering takes place at $n = 5$ and thereafter the energy difference between the optimal ferrimagnetic and optimal FM structure increases with the cluster size, which indicates that the optimal FM states become more and more unfavorable with increasing cluster size . However, different ferrimagnetic states are possible within a small ~ 0.1 eV energy

difference and their plausible presence in the experimental SG beam along with the ground state has been argued. The predicted magnetic moments are in agreement with the SG experiment. The sudden decrease in the magnetic moment at $n = 13$ and 19 is due to their 'closed' icosahedral structure. It should be pointed out here that in the present calculation we assumed only collinear alignment of spins. However, spin canting or non-collinear magnetic ordering is possible in small magnetic clusters as it occurs more easily in a low symmetry magnetic system [126]. Icosahedral growth pattern is observed for the intermediate size range. However, to our knowledge, a different kind of icosahedral packing have been observed for $Mn_{15} - Mn_{17}$ clusters. In any particular cluster, the average bond length between anti-ferromagnetically aligned atoms are 3−8 % shorter than that of the ferromagnetically alligned, which can be explained in terms of the Pauli repulsion. Spin segregation has been observed in the intermediate size range. The $d-$electron localization strongly depends on coordination: localization decreases with the coordination number. There is no signature of non-metal to metal transition at n =16, which has been predicted [110] through the downward discontinuity observed in the reaction rate with H_2.

Chapter 5

Non-collinear magnetism in pure Mn_n clusters

In the previous chapter, we have discussed Mn_n clusters with the assumption that all the atomic moments align collinearly i.e parallel or anti-parallel to each other. However, spin canting or non-collinearity of the atomic moments may occur in low symmetry systems such as surfaces and clusters. In this chapter we shall show that small Mn_n clusters have non-collinear magnetic orderings, which implies that we have to generalize our ideas of the previous chapter and include the study of non-collinear magnetism in clusters [1]

5.1 Introduction

Non-collinear magnetic ordering exists in a variety of systems. For examples, the complex orderings in topologically frustrated anti-ferromagnets, spiral spin density wave states and spin-spiral states. These types of orderings are called inter-atomic non-collinear magnetism as it is the different atomic moments which are non-collinear. More generally, non-collinear configurations occur more easily in a low symmetry or disordered magnetic systems [129, 130]. Thus small clusters which have less symmetry constraints than the bulk are likely candidates for non-collinear structures. Face-centered cubic Fe has a spin-spiral ground state [131, 132] and body-centered cubic Cr has a spin density wave ground [133]. Small Fe and Cr clusters ($n \leq 5$) were found to have non-collinear magnetic

[1] This chapter is based on the following papers :
(1) **Mukul Kabir**, D.G. Kanhere and A. Mookerjee, *Large magnetic moments and anomalous exchange coupling in As-doped Mn Clusters*, Phys. Rev. B **73**, 075210 (2006).
(2) **Mukul Kabir**, D. G. Kanhere and A. Mookerjee, *Emergence of non-collinear magnetic ordering in small magnetic cluster*, Submitted to Phys. Rev. B (2006).

structure [134, 135, 136].

In the previous chapter we had discussed that from the structural and magnetic point of view, manganese is one of the most complex of all metals and has attracted a considerable attention. Mn atom has an electronic configuration $4s^2 3d^5$ and according to Hund's rule a high magnetic moment of 5 μ_B due to the half-filled $3d$ sub-shell. Moreover, it has high $4s^2 3d^5 \rightarrow 4s^1 3d^6$ promotion energy and consequently, Mn-atoms do not bind strongly when they are brought together to form a cluster or a crystal. The most stable polymorph, α-Mn, has an exotic crystal structure containing 58 atoms in a cubic unit cell. This α-Mn exhibits a complex antiferromagnetic order below the Néel temperature of 95 K and is nonmagnetic at room temperature [137]. This magnetic transition of α-Mn is coupled to a tetragonal distortion. Recent density functional calculations found non-collinear magnetic ground state of α-Mn [138] and the other polymorph of Mn, known as β-Mn, also has a stable non-collinear configuration even though the ground state is weakly ferrimagnetic [139]. These results are in good agreement with the neutron scattering [140], magnetic torque [141] and nuclear magnetic resonance [142] experiments, where the experimental results are interpreted in terms of non-collinear antiferromagnetic structure.

Thus small Mn clusters which have less symmetry constraints are likely candidates for the occurrence of non-collinear magnetic structure. However, all the theoretical calculations so far have been made under the collinear spin assumption [106]-[109],[126]. Among all of them, most extensive study has been done by Kabir *et al.*, where the structural and magnetic properties of Mn_n clusters in the size range n = 2-20 have been investigated from the density functional theory (DFT) calculations [126], which have been discussed in the previous chapter extensively. It was found that Mn_2, Mn_3 and Mn_4 exhibit ferromagnetic ordering, whereas a magnetic transition to the ferrimagnetic ordering takes place at n =5 and continues to be the ground state for clusters with n >5. The predicted magnetic moments are in well agreement with the Stern-Gerlach (SG) clusters beam experiment [26, 27]. Morisato *et al.* studied Mn_5 and Mn_6 clusters and found Mn_6 to be the smallest cluster to exhibit non-collinear ground state [143]. However, using local spin density approximation Longo *et al.* found all the clusters in the size range n = 3-7, have non-collinear ground state [144]. Recently, non-collinear magnetic ordering has also been found in small Mn-clusters supported on a Cu(111) surface [145]. However in this study

cluster geometries have been assumed to be planer and they were placed on a regular face-centered cubic Cu lattice with experimental lattice parameters. No structural relaxation for both the surface and the cluster has been considered.

5.2 Methodology

In the generalized, non-collinear DFT approach [146]-[149], the wave functions are described by two-component spinors, $\Psi(\mathbf{r}) \equiv (\Psi^{\alpha}(\mathbf{r}), \Psi^{\beta}(\mathbf{r}))$, where α and β are the spin indeces. The density matrix is defined as,

$$\rho_{\alpha\beta} = \sum_i f_i \Psi_i^{\alpha}(\mathbf{r}) \Psi_i^{\beta *}(\mathbf{r}), \tag{5.1}$$

where f_i is the occupation number of the single-particle state.
The charge $n(\mathbf{r})$ and magnetization $\vec{m}(\mathbf{r})$ parts of the density matrix can be extracted by expanding in terms of the Pauli spin matrices $\underline{\sigma}_k$ $(k = x, y, z)$,

$$\underline{\rho}(\mathbf{r}) = \frac{1}{2}\left[n(\mathbf{r})\underline{I} + \sum_k m_k(\mathbf{r})\underline{\sigma}_k \right], \tag{5.2}$$

where m_k are the Cartesian components of $\vec{m}(\mathbf{r})$. The exchange-correlation potential, $\underline{v}_{xc} = v_0(\mathbf{r})\underline{I} + \vec{\xi}(\mathbf{r}) \cdot \vec{\underline{\sigma}}$, contains nonmagnetic and magnetic parts. The nonmagnetic part v_0 and $|\vec{\xi}|$ are given as a function of n and $|\vec{m}|$ in the same way that is done in the case of collinear magnetism, but here in addition $\vec{\xi}(\mathbf{r})$ is always parallel to $\vec{m}(\mathbf{r})$. In this scheme, the individual eigenstates can have different spin quantization directions and furthermore, the spin quantization axis of the each state can vary with position.

Calculations have been performed using DFT within the pseudo-potential plane wave method. The projector augmented wave method [59, 60] has been used and for the spin-polarized gradient approximation to the exchange-correlation energy we used the Perdew-Burke-Ernzerhof functional [48], as implemented in the Vienna *ab-initio* Simulation Package [112]. The $3d$, $4s$ electrons of the Mn-atom are treated as valence states. The spinor wave functions are expanded in a plane wave basis set with the kinetic energy cutoff 337.3 eV. Reciprocal space integrations are carried out at the Γ-point. We adopted periodic boundary conditions and described the cluster within a large simple cubic super-cell such that the periodic images are separated by at least 12 Å vacuum region.

This essentially ensures the interactions between the periodic images to become negligible. Symmetry unrestricted optimizations were performed using quasi-Newtonian and conjugate gradient methods until all the force components are less than 0.005 eV/Å. For a particular sized Mn_n cluster, several different initial structures were studied to ensure that the globally optimized geometry does not correspond to the local minima, and to be extensive, both non-collinear and collinear magnetic structures have separately been considered. Moreover, we explicitly considered all possible spin multiplicities for the collinear case.

For a collinear spin cluster all the spins are parallel (0^0) or anti-parallel (180^0) to each other. However, the angle between any two moments could be anything in between 0^0 and 180^0 for a non-collinear case and the deviation from 0^0 or 180^0 is called "degree of non-collinearity". The average degree of non-collinearity for a particular cluster can be defined as,

$$\theta = \frac{\sum_{i,(<j)} |\Theta - \theta_{ij}|}{\sum_{k}^{N-1}(N-k)}, \tag{5.3}$$

where ij runs for all independent spin pairs and $\sum_{k}^{N-1}(N-k)$ is the total number of such independent spin(atom) pairs with N being the number of atoms in the cluster. Θ is either 0^0 or 180^0 and θ_{ij} is the angle between i-th and j-th moment.

5.3 Results

5.3.1 Pure Mn_n clusters: Collinear vs non-collinear ordering

In the previous, we have extensively discussed the magnetic ordering of pure Mn_n ($n \leq 20$) clusters within the collinear spin assumption [126]. Above a certain cluster size (n=5), the magnetic ordering was found to be ferrimagnetic and the calculated magnetic moments were in agreement with the Stern-Gerlach experiment [26, 27]. However, the validity of the collinear spin assumption should be checked rigorously because, in principle, the complex ferrimagnetic ordering and magnetic 'frustration' [150] could finally lead to the non-collinear ordering in Mn clusters. Type of magnetic ordering along with the total magnetic moment, relative energy difference are given in the Table 5.1 and Table 5.3 and the optimal non-collinear structures are shown in Fig. 5.1 and Fig. 5.2 for pure Mn_n

Table 5.1: Type of magnetic ordering, average degree of non-collinearity (θ), total magnetic moment ($M_{\rm tot}$) and the relative energy difference (ΔE = E - $E_{\rm GS}$) for pure Mn_n clusters for n =2—8.

Cluster	Magnetism	θ (^{0})	$M_{\rm tot}$ (μ_B)	$\triangle$E (meV)
Mn_2	collinear	-	10	0
Mn_3	collinear	-	15	0
	non-collinear	42	8.54	35
	non-collinear	38.89	8.27	36
	non-collinear	44	8.77	38
	collinear	-	5	46
	non-collinear	55.5	3.63	325
Mn_4	collinear	-	20	0
	non-collinear	4.98	19.96	31
	collinear	-	10	78
Mn_5	collinear	-	3	0
	non-collinear	12.05	4.43	18
	non-collinear	51.94	12.46	60
	collinear	-	13	60
	collinear	-	5	79
Mn_6	non-collinear	48.8	12.83	0
	non-collinear	9.26	8.48	96
	collinear	-	8	123
	collinear	-	2	140
Mn_7	collinear	-	5	0
	collinear	-	7	91
	collinear	-	3	192
	non-collinear	0.63	5.00	232
	non-collinear	48.12	2.86	241
Mn_8	non-collinear	22.85	6.83	0
	collinear	-	8	170
	collinear	-	12	170
	collinear	-	10	200

clusters.

Table 5.2: Magnetic moments (μ_B) and angles (θ_{ij} in degree) between the moments for the non-collinear ground state of Mn_6 (Fig.1h).

i/j	1	2	3	4	5	6	Moment
1	-	156	2	146	77	75	3.62
2	156	-	154	9	79	80	3.64
3	2	154	-	145	75	74	3.62
4	146	9	145	-	70	71	3.63
5	77	79	75	70	-	1	3.80
6	75	80	74	71	1	-	3.80

The case of triangular Mn_3 is interesting. If the triangle is equilateral and the magnetic ordering is antiferromagnetic then the third atom doesn't know how to align and, consequently, is in the 'frustrated' state. Then the Mn_3 cluster could remove its frustration either by reducing its geometrical symmetry or by adopting non-collinear magnetic order or by both of these. The ground state is collinear ferromagnetic with 5 μ_B/atom magnetic moment and has equilateral triangular geometry. The optimal non-collinear structure is the next isomer, which lies 35 meV higher in energy. This structure has high non-collinearity and a total magnetic moment of 8.54 μ_B (Fig. 5.1a). The geometrical structure is a isosceles triangle. We also find several non-collinear (Fig. 5.1b-d) and collinear magnetic states which lie close in energy. However, triangular Mn_3 cluster prefers non-collinear structure when it is placed on a Cu(111) surface, where each moments lie parallel to the Cu(111) surface and make an equal angle of 120^0 to its neighbor [145]. For this case, it has also been pointed out that the intra cluster exchange parameter is much stronger than that of inter cluster as the magnetic ordering is not affected if cluster-cluster distance becomes very small.

A collinear ferromagnetic ground state with total magnetic moment of 20 μ_B is found to be the ground state. The optimal non-collinear lies only 31 meV higher and have comparable magnetic moment. In comparison, Longo *et al.* [144] found a non-collinear ground state with a low magnetic moment, 4.5 μ_B, to be the ground state. It has to be noted, however, that they have used local spin density approximation for the exchange-correlation.

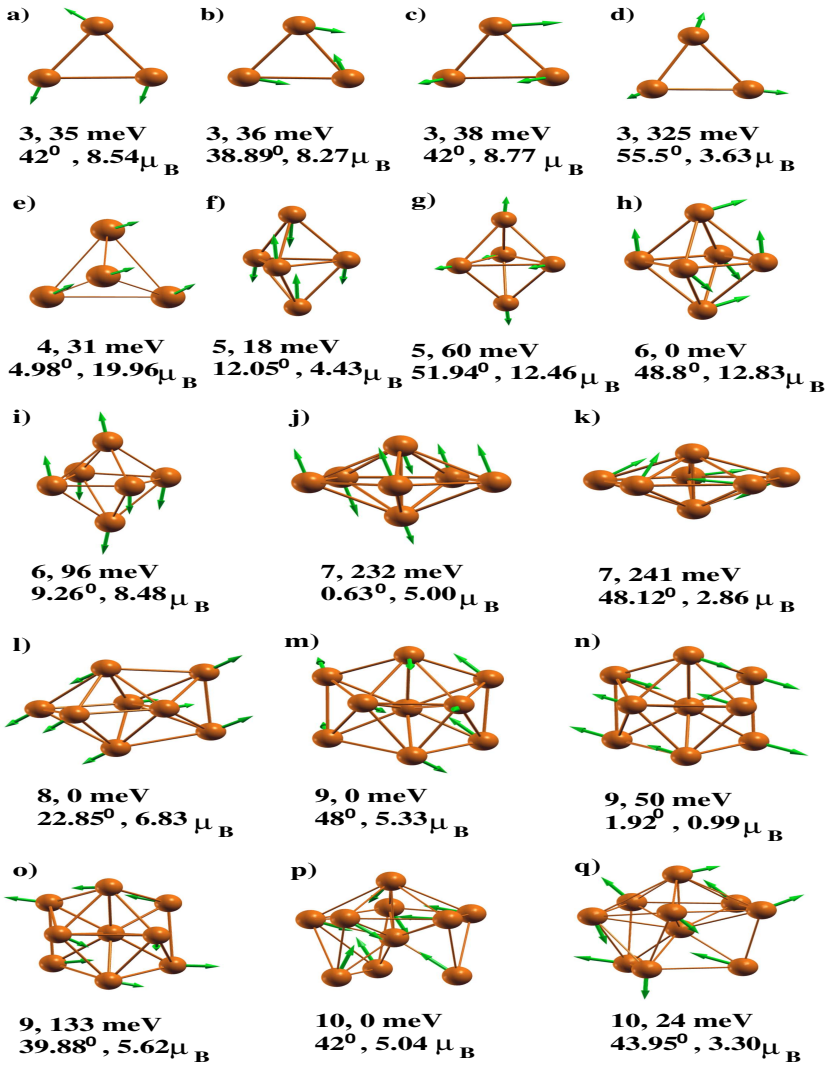

Figure 5.1: Optimal non-collinear structures for Mn_n clusters in the size range n =3-10. The first line gives the number of atoms n in the cluster and the energy relative to the corresponding ground state, ΔE, (meV), whereas, the second line represents the average degree of non-collinearity (θ in degree) and the corresponding total magnetic moment (μ_B). The optimal collinear structures are not shown here rather we refer to Ref. [126].

The Mn_5 cluster has been investigated by numerous authors but most of them have restricted themselves to the collinear spin assumption [106]- [108],[126]. However, few attempts have been made to allow non-collinear magnetic ordering[143]-[151]. We find

Table 5.3: Same as the Table 5.1 for Mn_9, Mn_{10}, Mn_{13}, Mn_{15} and Mn_{19} clusters.

Cluster	Magnetism	θ (^{0})	$M_{\rm tot}$ (μ_B)	$\triangle$E (meV)
Mn_9	non-collinear	48	5.33	0
	non-collinear	1.92	0.99	50
	non-collinear	39.88	5.62	133
	collinear	-	7	181
Mn_{10}	non-collinear	42	5.04	0
	non-collinear	43.95	3.30	24
	collinear	-	14	81
Mn_{13}	non-collinear	2.56	3.15	0
	collinear	-	3	0
	non-collinear	6.85	3.80	11
	collinear	-	7	77
	non-collinear	5.06	3.37	269
	non-collinear	30.37	11.57	304
Mn_{15}	collinear	-	13	0
	non-collinear	0.90	13.00	26
	collinear	-	5	33
	non-collinear	4.70	12.91	49
	non-collinear	8.03	26.85	343
Mn_{19}	collinear	-	21	0
	non-collinear	4.55	20.89	5
	collinear	-	19	9
	collinear	-	9	74

that the collinear ferrimagnetic ground state lies slightly lower (18 meV) in energy than the optimal non-collinear state. The average degree of non-collinearity found for this structure is 12^0. The next non-collinear (12.46 μ_B, $\theta \sim 52^0$) and a ferrimagnetic collinear structures are degenerate and are followed by another collinear ferrimagnetic state [126].

The Mn_6 cluster is found to be the smallest cluster to have non-collinear magnetic order in the ground state. This structure is highly non-collinear ($\theta \sim 49^0$) and has distorted octahedral structure, which posses 12.83 μ_B magnetic moment. Present result agrees with

Morisato *et al.* [143], who found a non-collinear state with 12.24 μ_B moment as ground state. The angles θ_{ij} between the atomic moments are given in the Table 5.2. The next isomer is non-collinear with a total moment of 8.48 μ_B, which lies 96 meV higher. These two non-collinear states are followed by four collinear structures with moments 8, 2, 16 and 26 μ_B [126].

The ground state for Mn_7 is collinear with total magnetic moment 5 μ_B. This structure is followed by two collinear isomers with a total 7 and 3 μ_B moment. As discussed in our previous report [126], this is the possible reason for large experimental uncertainty observed, 0.72 ± 0.42 μ_B/atom [26]. The optimal non-collinear structure lies much higher (232 meV) in energy and this structure has equal magnetic moment with the collinear ground state. However, a non-collinear state has been reported to be the ground state in an earlier report [144].

The present results up to the size range ($n \leq 7$) discussed above agree well with Morisato *et al.* [143]. They have adopted the same level of theory used in the present report to study Mn_5 and Mn_6 and found the Mn_6 cluster to be the smallest cluster which show non-collinear magnetic ordering. On the other hand, Longo *et al.* [144] studied Mn_3-Mn_7 clusters within a somewhat different approximation level. They have used local spin density approximation for the exchange-correlation energy and found the magnetic ordering to be all non-collinear for all the clusters studied.

As it has been discussed in the Ref. [126], we have considered many different initial structures for Mn_8. However, when we allow non-collinearity among the moments, we find a non-collinear bi-capped octahedral structure with magnetic moment 6.83 μ_B to be the ground state. This non-collinear state is followed by two degenerate collinear magnetic structures and they lie 170 meV higher in energy. The moment of the non-collinear ground state of 0.85 μ_B/atom is very close to the experimental value of 1.04 ± 0.14 μ_B/atom [27].

A non-collinear centered anti-prism with total moment 5.33 μ_B is the ground state for 9-atom manganese cluster. This structure has high non-collinearity, $\theta \sim 48^0$. We find another less non-collinear ($\theta = 1.92^0$) structure with very tiny total magnetic moment is the first isomer, which lies 50 meV higher in energy. The next isomer is also non-collinear in nature with comparable magnetic moment with the ground state. This structure lies 133 meV higher in energy. The optimal collinear structure lies 181 meV higher in energy

and has a total 7 μ_B magnetic moment.

In the previous chapter, within the collinear assumption, we have seen that there exists four collinear magnetic structures within very small energy width $\sim$ 10 meV for Mn_{10} cluster. However, there we have treated the atomic moments collinearly. In the present case, we find that a non-collinear magnetic structure with magnetic moment 5.04 μ_B is lower in energy by 81 meV than the previously found optimal collinear structure. This structure is highly non-collinear with θ to be 42^0. All these structures, whatever collinear or non-collinear, have a pentagonal ring and can be seen as incomplete icosahedra.

In the previous chapter, for the Mn_{13} cluster, we have investigated icosahedral, cub-octahedral and a hexagonal closed packed structures within the collinear spin assumption and found an icosahedral structure to be the ground state, which had a total magnetic moment of 3 μ_B [126]. The optimal hexagonal closed-packed and cub-octahedral structures were found to have higher magnetic moments, 9 and 11 μ_B respectively, and they lie much higher in energy, 0.89 and 1.12 eV, respectively. Here we investigated only the icosahedral structure and found a non-collinear magnetic structure with 3.15 μ_B moment to be degenerate with the previously found collinear structure. The average θ is found to be small (2.5^0) for this structure. The optimal non-collinear structures are shown in Fig. 5.2a-d. Another non-collinear structure is nearly degenerate (11 meV) with θ to be 6.8^0. This structure has comparable magnetic moment. Another two non-collinear structures (Fig. 5.2c-d) are found and they lie 269 and 304 meV higher, respectively and the average deviation is 5 and 30.31^0, respectively.

Two different competing icosahedral structures, 5,1,5,1,3 and 1,5,1,5,1,2 staking, were found to have five isomers within $\sim$ 60 meV energy for Mn_{15} within the collinear atomic spin moment assumption [126]. The ground state had a magnetic moment of 0.87 μ_B/atom, whereas the experimentally measured value is rather high, 1.66 $\pm$ 0.02 μ_B/atom. No isomer with comparable magnetic moment was found [126]. At this point it would be interesting to investigate if this large discrepancy between the experimental and theoretically predicted magnetic moment originated from collinear spin assumption. However, the discrepancy does not improve when we relax the collinear spin assumption and treat the moments non-collinearly (Table 5.3). Two non-collinear structures (Fig. 5.2e,f) lie very close in energy with the previously found collinear ground state. These two structures

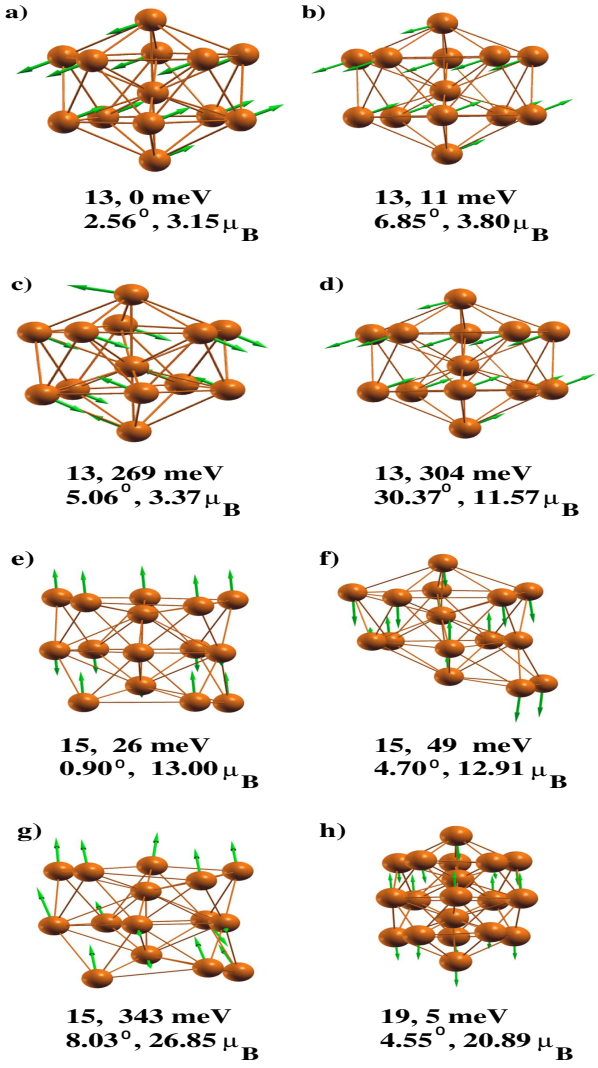

Figure 5.2: Optimal non-collinear magnetic ordering for Mn_{13}, Mn_{15} and Mn_{19}.

are of first and second kind of icosahedra with $\theta = 0.9^0$ and 4.7^0, respectively. However, a structure of the first kind is found with magnetic moment (1.79 μ_B/atom), which is close to the experimental value (1.66 $\pm$ 0.02 μ_B/atom [26, 27]), but this structure lies well above (343 meV) the ground state and is highly non-collinear (Fig. 5.2g).

It has experimentally been found that the magnetic moment of Mn_{19} cluster is relatively smaller than that of its neighboring clusters [26, 27]. Within the collinear moment approximations, a double icosahedral structure was found to be the ground state, which

had a total moment of 21 μ_B [126]. This is somewhat larger than the experimentally predicted value [26, 27]. Another collinear magnetic structure with magnetic moment (9 μ_B) close to the experimental value lies only 75 meV higher. In the present study, which allows non-collinear arrangement of magnetic moments, we found the optimal non-collinear structure to be nearly equi-energetic (Table 5.3) with low degree of non-collinearity. This structure has nearly equal magnetic moment with the optimal collinear structure.

5.3.2 Binding energy and magnetic moment

Binding energies of the optimal collinear and non-collinear magnetic structures have been shown in Fig. 5.3 for pure Mn_n and As@Mn_n clusters. It has been understood [126] that due to the lack of hybridization between the filled $4s$ states and the half-filled $3d$ states and due to high (2.14 eV) $4s^2\ 3d^5 \rightarrow 4s\ 3d^6$ promotion energy, Mn atoms do not

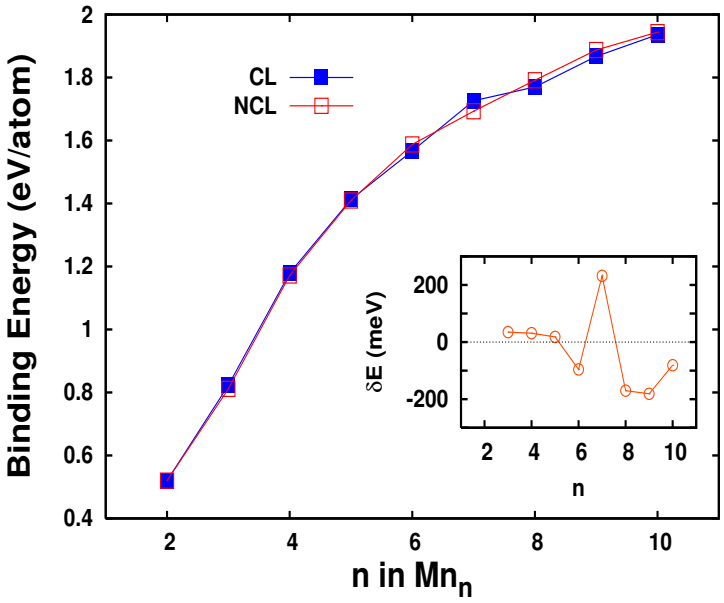

Figure 5.3: Plot of binding energy for optimal collinear and non-collinear configurations as a function of Mn atoms (n) in pure Mn_n. Binding energy is defined as, $BE(Mn_n) = -[\ E(Mn_n) - n\ E(Mn)]/n$ where $E(Mn_n)$ is the total energies of pure Mn_n cluster. Inset shows the total energy difference between the optimal collinear (CL) and non-collinear (NCL) configurations, δE, as a function of n.

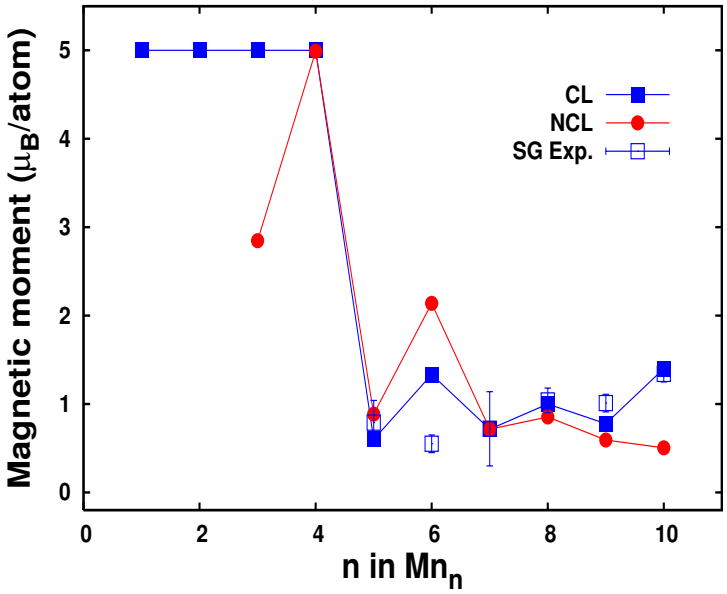

Figure 5.4: Magnetic moments of optimal collinear and non-collinear states are plotted as a a function of cluster size n.

bind strongly when they form clusters or crystals. This is manifested through their low binding energy, which is the lowest among all other $3d$- transition metal clusters. This is also experimentally evidenced through recent photo-dissociation experiments for cationic clusters [7, 100]. Since the mixing between the valence d and s states increases with increasing size, the binding energy increases with increasing cluster size.

The total energy difference, δE, between the optimal collinear and non-collinear structure is defined as,

$$\delta E = -[E_{\rm CL}(n) - E_{\rm NCL}(n)] \tag{5.4}$$

and plotted in the inset of Fig. 5.3. By definition if δE is positive(negative) the corresponding ground state is collinear(non-collinear). In the previous chapter, we discussed Mn_2, Mn_3 and Mn_4 have ferro-magnetically coupled atomic spins, and they are collinear. Here we find that the Mn_5 has collinear ground state, which is nearly degenerate with non-collinear magnetic structure. The collinear states are found to be lower in energy than the corresponding optimal non-collinear states up to five Mn-atoms in the cluster and in the size range $n \geq 6$ the non-collinear states start to be ground state. However,

it should be noted here that for the entire size range there exists several collinear and/or non-collinear isomers which are close in energy with the corresponding ground state (see Table 5.1 and 5.3). This establishes the importance to treat the moments non-collinearly.

The total magnetic moment of pure Mn_n clusters for the optimal collinear and non-collinear states are plotted in the Fig. 5.4. The results are compared with the experimentally predicted values. Clusters in the size range $n \leq 4$ have collinear ground state and the Mn-Mn coupling is ferromagnetic. These clusters have a 5 μ_B/atom magnetic moment which is the Hund's rule value for isolated Mn-atom. The magnetic moment per atom decreases drastically at and after $n = 5$ and the magnetic ground states start to be non-collinear for $n \geq 6$. The large moments of pure Mn_n clusters arise from the localized $3d$ electrons at Mn-atoms.

5.4 Conclusion

In the previous chapter we have studied Mn_n clusters under the collinear atomic moment assumption. The present chapter presents a systematic investigation of emergence of non-collinear magnetism in pure Mn_n clusters within the gradient-corrected DFT approach. No considerable structural change has been found due to non-collinear treatment of atomic moments. The ground state of both pure Mn_n clusters for $n \leq 5$ is collinear and emergence of non-collinear ground states is seen for $n \geq 6$. However, there exists many collinear and non-collinear isomers. Although the results presented here are specific to the Mn_n clusters, they also contain more general picture: non-collinear magnetic ordering is possible in small magnetic clusters.

Chapter 6

Unconstrained density-functional study of bonding and magnetic structure of As doped Mn_n clusters

In the previous chapter we have shown that small Mn_n clusters may adopt non-collinear magnetic ordering. In this chapter we shall use the same density-functional approach, unconstrained to allow for non-collinear ordering, and study how magnetic ordering is perturbed by doping the cluster with a single nonmagnetic As atom. We shall see how the dopant As-atom enhances bonding and how it affects Mn-Mn exchange couplings.[1].

6.1 Introduction

Emergence of finite magnetic moments $\sim 1\ \mu_B$/atom in manganese clusters (Mn_{5-99}), which in its bulk α phase is antiferromagnetic below a Néel temperature of 95 K and is nonmagnetic at room temperatures, has been demonstrated through Stern-Gerlach (SG) deflection measurement [26, 27]. In the previous two chapters, we have discussed density functional calculations of pure Mn_n clusters in the size range n=2–20, and the results are in good agreement with the SG experiment. The reason for this finite magnetic moment in small Mn_n clusters is readily understood to derive from the reduced atomic coordination

[1]This chapter is based on the following papers :
(1) **Mukul Kabir**, D. G. Kanhere and A. Mookerjee, *Large magnetic moments and anomalous exchange coupling in As-doped Mn clusters*, Phys. Rev. B **73**, 075210 (2006).
(2) **Mukul Kabir**, D. G. Kanhere and A. Mookerjee, *Emergence of non-collinear magnetic ordering in small magnetic clusters*, (Submitted to Phys. Rev. B).
(3) **Mukul Kabir**, A. Mookerjee and D. G. Kanhere, *Magnetism in pure and doped manganese clusters*, Vol-4 pp 1018-1021 (Brill Academic Publishers, The Netherlands, 2005).

resulting in strong d-electron localization.

It will be particularly interesting to see what happens to the electronic and magnetic properties if we dope a Mn_n cluster with a single nonmagnetic atom, for example, As, to form an As@Mn_n cluster. This study would be interesting since the Mn *clustering* in ferromagnetic $Ga_{1-x}Mn_xAs$ and $In_{1-x}Mn_xAs$ samples has attracted considerable attention. The real dilute magnetic semiconductor alloys may exhibit some clustering which comes from the attractive interaction between magnetic ions [152] (Mn in the present case) and, indeed, there are experimental evidences for a tendency to cluster formation [153, 154, 155]. Generally, the Mn dopant substitutes the Ga site and serves dual roles − provides local magnetic moment and acts as acceptor providing itinerant holes, which mediate ferromagnetic order. However, in reality, low substrate temperatures ($\sim$ 200-300 ^{0}C) and strong segregation tendency (of magnetic ions into semiconductor host) leads to high defect concentrations, the most important being Mn interstitials, Mn_I [156], which are double donors that compensates holes provided by substitutional Mn_{Ga}. The increase in Curie temperature (T_C) might, therefore, related to a removal of these Mn_I defects. Different kinds of defects have been reported: clustering [157, 152, 158] and random distribution [159, 158] of Mn as well as Mn_I [160] and As anti-sites [161, 162, 163] and there is increasing consensus that ordering increases T_c, while it decreases with clustering [158]. In recent years, Curie temperature in the $Ga_{1-x}Mn_xAs$ has risen steadily, reaching $\sim$ 170 K for $x \sim$ 0.08, when grown in layered structure and annealed at low temperature [164, 165, 166]. However, local spin-density approximation with mean-field predicts a rather high T_c for $Ga_{1-x}Mn_xAs$ (typically 350-400 K for $x \sim 0.08$) [152, 167, 168, 169, 170, 171]. This large discrepancy with experiment is attributed to uncontrolled approximations in treating the effective Heisenberg model describing interactions between localized magnetic impurities [159, 172, 173]. However, recently predicted T_c, assuming disorder [174, 173] and percolation [159] effect, are in good agreement with the experiment.

In this chapter, we address the possibility of Mn clustering around As and the consequent nature of Mn-Mn magnetic coupling? We have, indeed, found that the binding energy of Mn_xAs clusters are substantially enhanced by single As doping by having their hybridized $s-d$ electrons bond with p electrons of As. This *stabilization* is also accompanied by the *ferromagnetic* Mn-Mn coupling for Mn_2As and Mn_4As clusters. Another in-

teresting motivation of the present study is motivated from the face that the non-collinear ferromagnetism is common in (III,Mn)V semiconductor [161, 175, 176, 177, 178]. Experimental study by Potashnik *et al.* [161, 175] indicated that the Curie temperature, the ground state saturation magnetization $M(T = 0)$ and the shape of the $M(T)$ curve all depend upon the temperature and annealing. This can be explained only if the non-collinearity in the localized Mn magnetic moments is considered in the ground state [176, 177, 178]. From this point of view, it will be interesting to observe whether the small As@Mn$_n$ clusters do show non-collinearity or not. Indeed, in the previous chapter, we have seen that pure Mn$_n$ clusters do show non-collinear magnetism. Therefore, it is interesting to investigate how the collinearity and non-collinearity of atomic moments are affected by single As-atom doping. Finally, we show that the Mn-Mn exchange interactions ($J's$) are anomalous and behave quite differently from Ruderman-Kittel-Kasuya-Yosida (RKKY)-like theory.

6.2 Computational Method

Calculations have been carried out using the density functional based projector augmented-wave method [59, 60]. For exchange-correlation functional we have used the one suggested by Perdew-Burke-Ernzerhof[48] for the spin-polarized generalized gradient approximation, as implemented in the VASP package [112]. The wave functions are expanded in a plane wave basis set with the kinetic energy cutoff 337.3 eV and calculations have been performed at the Γ-point only. The $4s$, $4p$ orbitals for As were treated as valence states. Symmetry unrestricted geometry optimizations were performed using quasi-Newtonian and conjugate gradient methods until all the force components are less than 0.005 eV/Å. Simple cubic super-cells are used with neighboring clusters separated by at least 12 Åvacuum regions. Both collinear (CL) and non-collinear (NCL) magnetic structures have separately been considered. Several initial structures were studied to ensure that the globally optimized geometry does not correspond to the local minima, as well as we explicitly considered all possible spin multiplicities for CL case.

6.3 Results and discussion

6.3.1 Structure

The Table 6.1 and Table 6.2 give the magnetic orderings of As@Mn_n clusters and they are depicted in the Fig. 6.1 for the size range n =1-10. The Mn-As dimer has much higher BE of 1.12 eV/atom and much shorter bond length (2.21 Å) than those of Mn_2 dimer. We have repeated our calculations of Mn-As dimer including the Mn $3p$ as valence electrons and obtained an optimized bond length of 2.22 Å and BE of 1.08 eV/atom, with the same total magnetic moment, which confirms that the inner $3p$ electrons contributes insignificantly to the bonding.

The Mn-Mn coupling is found to be ferromagnetic (Fig. 6.1a) for As@Mn_2 cluster, which has a total magnetic moment of 9 μ_B. The Mn-Mn distance in this collinear As@Mn_2 is same with the pure Mn_2 dimer. However, this collinear ground state is nearly degenerate with a non-collinear magnetic structure (Fig. 6.1b). Another collinear structure with antiferromagnetic Mn-Mn coupling (Fig. 6.1c) is found to be the next isomer which lies 110 meV higher than that of the ground state.

The pure Mn_3 cluster was found to be ferromagnetic with large 5 μ_B magnetic moment and is collinear in nature. The single As-atom doping reduces its magnetic moment considerably to a total of 4 μ_B for As@Mn_3 cluster in its ground state. This structure is also collinear in nature, which is shown in Fig. 6.1d. However, likewise in the pure case, there exists several isomers with different magnetic nature (Table 6.1 and Fig. 6.1e,f). The next three isomers are all non-collinear and they lie close in energy, 5, 8 and 43 meV higher, respectively.

The optimal collinear structure with 20 μ_B magnetic moment was found to have 31 meV less energy than the optimal non-collinear structure for the pure tetramer. The average bond length of As@Mn_4 (2.59 Å) is much larger than that of the pure Mn_4 (2.70 Å) cluster. The optimal non-collinear structure (Fig. 6.1h) is nearly degenerate with the collinear ferromagnetic ground state (Fig. 6.1g) for As@Mn_4 cluster. The next isomer is also non-collinear in nature and all these three structures have comparable magnetic moments.

Table 6.1: Magnetic ordering, average degree of non-collinearity [179] (θ), total magnetic moment ($M_{\rm tot}$) and relative energy difference (ΔE) for As@Mn$_n$ clusters for n =1—8.

Cluster	Magnetism	θ (^{0})	$M_{\rm tot}$ (μ_B)	ΔE (meV)
As-Mn	collinear	-	4	0
As@Mn$_2$	collinear	-	9	0
	non-collinear	3.64	9.00	2
	collinear	-	1	110
As@Mn$_3$	collinear	-	4	0
	non-collinear	2.05	3.99	5
	non-collinear	4.79	3.97	8
	non-collinear	54.46	0.81	43
As@Mn$_4$	collinear	-	17	0
	non-collinear	20.64	16.09	6
	non-collinear	17.63	16.33	18
As@Mn$_5$	collinear	-	2	0
	non-collinear	7.51	2.00	7
	non-collinear	43.73	9.29	62
	non-collinear	44.26	10.08	68
As@Mn$_6$	non-collinear	6.99	1.28	0
	collinear	-	9	159
	non-collinear	0.91	9.00	168
	non-collinear	24.04	7.59	196
As@Mn$_7$	collinear	-	6	0
	non-collinear	18.88	4.93	16
	collinear	-	14	26
	non-collinear	48.77	6.28	66
	non-collinear	7.59	21.83	104
	non-collinear	44.59	8.62	108
As@Mn$_8$	non-collinear	0.67	3.00	0
	non-collinear	37.56	12.53	7
	collinear	-	7	17
	non-collinear	23.45	10.84	46
	collinear	-	3	120

Table 6.2: Same as Table 6.1 for $As@Mn_9$ and $As@Mn_{10}$ clusters.

Cluster	Magnetism	θ (^{0})	M_{tot} (μ_B)	ΔE (meV)
$As@Mn_9$	non-collinear	43.24	0.10	0
	collinear	-	10	247
	non-collinear	8.01	3.88	353
$As@Mn_{10}$	non-collinear	44.22	3.09	0
	non-collinear	22.52	1.37	36
	collinear	-	13	90

The ground state of the $As@Mn_5$ is also collinear (Fig. 6.1i), which is nearly degenerate with the optimal non-collinear structure (Fig. 6.1j). Both of these structures have equal magnetic moments, which are particularly small. The next two isomers are non-collinear with high non-collinearity and have comparatively large magnetic moments.

Similar to the pure Mn_6 cluster, the ground state of $As@Mn_6$ is the smallest cluster which show non-collinear magnetism (Fig. 6.1l). This non-collinear structure lies 159 meV lower than the next isomer, which is collinear (Fig. 6.1m). This non-collinear ground state has small magnetic moment (1.28 μ_B) compared to the collinear (9 μ_B) configuration. The non-collinear ground state has a As-capped Mn-octahedral geometry, whereas the next (collinear) isomer is a pentagonal bi-pyramid, where the As-atom sits in the pentagonal ring. Another non-collinear structure lies 196 meV higher which has large non-collinearity (24.04^0) and comparable magnetic moment with the collinear structure.

The ground state of the $As@Mn_7$ cluster is collinear (Fig. 6.1n) with a total magnetic moment of 6 μ_B. The next isomer is non-collinear in nature with 4.94 μ_B magnetic moment (Fig. 6.1o), which lies sightly higher (16 meV) in energy. However, for pure Mn_7 cluster, the energy difference between the collinear ground state and the optimal non-collinear state is large, 232 meV, i.e. the single As doping reduces the energy difference between the collinear ground state and the optimal non-collinear state. Moreover, there exists several collinear and non-collinear structures (Table 6.1) which are close in energy.

The ground state of the $As@Mn_8$ cluster is found to be non-collinear. However, the degree of non-collinearity is very small (Fig. 6.1q). The next isomer is also non-collinear

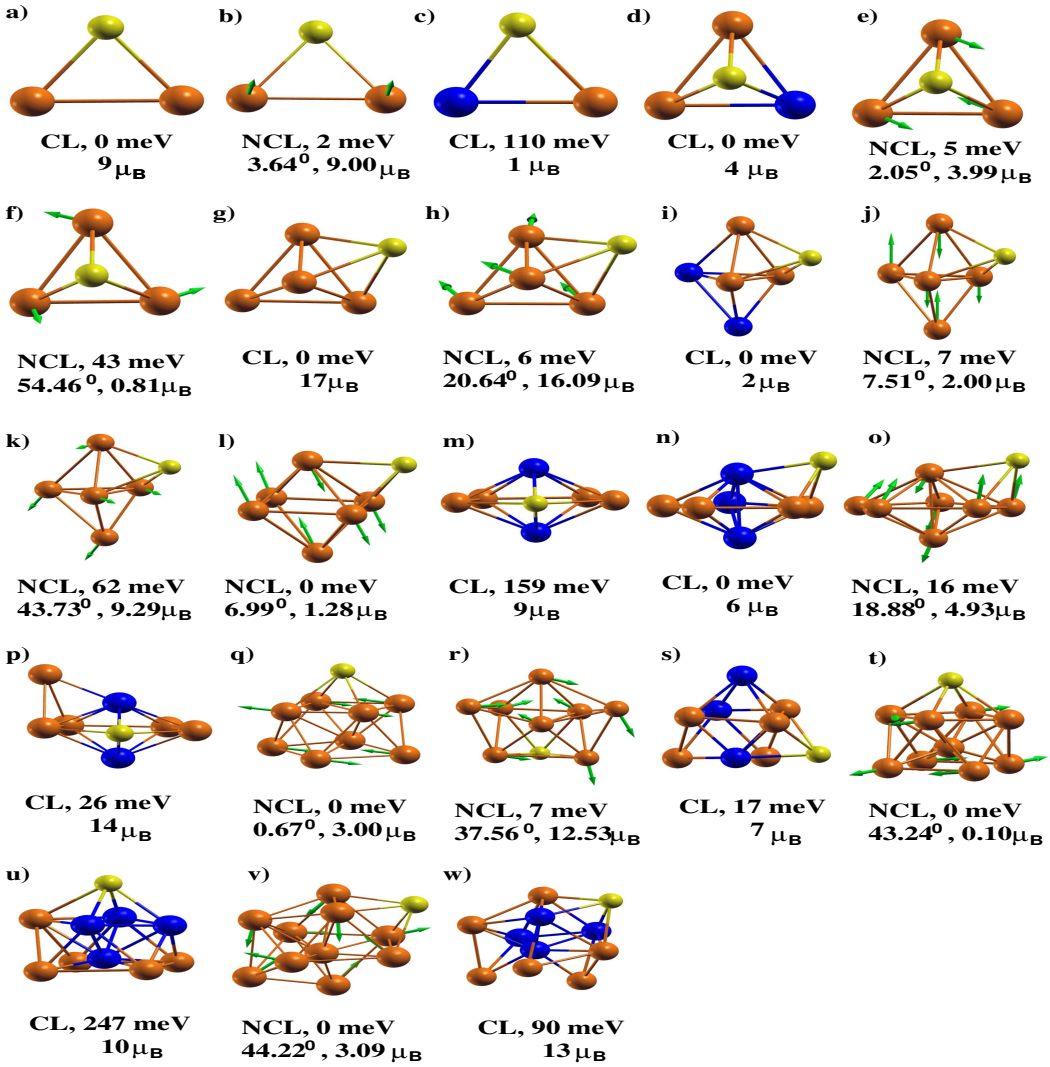

Figure 6.1: The ground state and closely lying isomers of As@Mn$_n$ clusters. The nature of magnetic ordering (collinear (CL) or non-collinear (NCL)), relative energy to the corresponding ground state (meV), the average θ (in degree) for NCL case and the total magnetic moment (μ_B) is given. For the collinear cases, orange(blue) refers the positive(negative) Mn moment. Yellow atom refers the As-atom for all the structures.

and has comparatively large magnetic moment and non-collinearity (Fig. 6.1r). Both these non-collinear structures are nearly degenerate. The optimal collinear structure (Fig. 6.1s) also lies very close in energy, which has 7 μ_B magnetic moment.

The ground state of As@Mn_9 is non-collinear with high non-collinearity, 43.24^0. However, the magnetic moment of this structure is nearly zero, 0.1 μ_B (Fig. 6.1t), which is much smaller than that of the pure Mn_9 cluster in its ground state. The next isomer is collinear in nature and has comparatively large magnetic moment, 10 μ_B. This collinear structure lies much higher, 249 meV, in energy.

We have found several isomers for the As@Mn_{10} cluster (Table 6.2). Among all a non-collinear magnetic structure (Fig. 6.1v) with high non-collinearity (45.22^0) is found to be the ground state. This structure has a total magnetic moment of 3.09 μ_B. The next isomer is also non-collinear which lies only 36 meV higher in energy. The optimal collinear structure have comparatively high magnetic moment and lies 90 meV higher (Fig. 6.1w).

6.3.2 Enhancement in bonding

As we have seen, in the chapters 4 and 5, for pure Mn_n clusters the binding energy is small compared to other $3d$ transition metal clusters. This was understood that it is derived from $4s^2\ 3d^5$ electronic distribution and comparatively large $4s^2\ 3d^5 \rightarrow 4s^1\ 3d^6$ promotion energy. However, the situation improves considerably due to single As-doping. The calculated binding energies, Calculated binding energies are plotted in Fig. 6.2 for both pure Mn_n and As@Mn_n clusters. When an As-atom is attached to the pure Mn_n clusters, due to the enhanced $p-d$ hybridization the binding energy of the resultant As@Mn_n clusters increase substantially. The total energy difference, δE, between the optimal collinear and non-collinear structure is plotted in the inset of Fig. 6.2. By definition if δE is positive(negative) the corresponding ground state is collinear(non-collinear). For both pure Mn_n and As@Mn_n clusters, the collinear states are found to be lower in energy than the corresponding optimal non-collinear states up to five Mn-atoms in the cluster and in the size range $n \geq 6$ the non-collinear states start to be ground state with the exception for n =7 for Mn_n and n =7,8 for As@Mn_n clusters. However, it should be noted here that for the entire size range there exists several collinear/non-collinear isomers which are close in energy with the corresponding ground state for both pure and doped clusters. This establishes the importance to treat the moments non-collinearly.

The next important issue is to see whether these Mn clustering around single As are

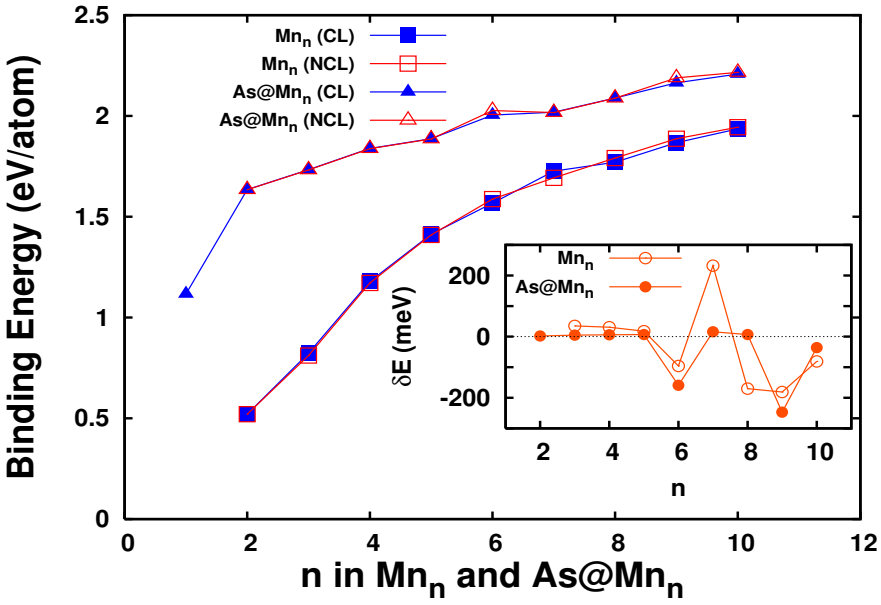

Figure 6.2: Plot of binding energy for optimal collinear and non-collinear configurations as a function of Mn atoms (n) in pure Mn$_n$ and As@Mn$_n$ clusters. Binding energy is defined as, BE(Mn$_n$) = $-$[E(Mn$_n$) $-$ n E(Mn)]/n for pure Mn$_n$ clusters and BE(As@Mn$_n$) = $-$[E(As@Mn$_n$) $-$ n E(Mn) $-$ E(As)]/(n+1) for As@Mn$_n$ clusters, where E(Mn$_n$) and E(As@Mn$_n$) are the total energies of pure Mn$_n$ and As@Mn$_n$ clusters, respectively. Inset shows the total energy difference between the optimal collinear(CL) and non-collinear (NCL) configuration (δE = -[E$_{\rm CL}$(n) - E$_{\rm NCL}$(n)]) as a function of n. The $\circ$($\bullet$) represent Mn$_n$(As@Mn$_n$) clusters.

at all energetically favorable or not. To understand this point, we calculate two different energy gains, Δ^1 - the energy gain in adding an As atom to a Mn$_n$ cluster and Δ^2 - the energy gain in adding a Mn atom to a Mn$_{1-n}$As cluster.

$$\Delta^1 = -[E(\text{As@Mn}_n) - E(\text{Mn}_n) - E(\text{As})] \quad (6.1)$$

$$\Delta^2 = -[E(\text{As@Mn}_n) - E(\text{As@Mn}_{1-n}) - E(\text{Mn})] \quad (6.2)$$

These two energy gains, Δ^1 and Δ^2, are plotted in Fig. 6.3. Due to the enhanced hybridization in As@Mn$_n$ clusters compared to pure Mn$_n$ cluster, the binding energy of the doped cluster increases substantially, which again increases with the size of the cluster

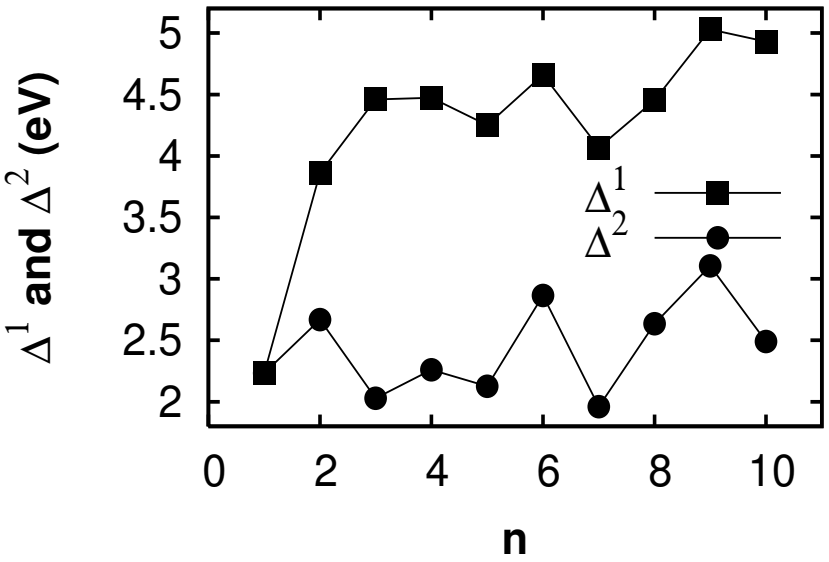

Figure 6.3: Two energy gains, Δ^1 and Δ^2, are plotted with n. Notice that for all n, the energy gain in adding an As-atom is larger than that of adding an Mn-atom to an existing pure Mn-cluster, i.e. $\Delta^1 >> \Delta^2$.

and consequently, Δ^1 increases with n, which finally tends to saturate (Fig. 6.3). The Δ^2 gives the number that how many Mn atoms can be bonded to a single As atom, which is still significant, 2.65 eV, for As@Mn_{10}. These behaviors of Δ^1 and Δ^2 and more precisely, $\Delta^1 \gg \Delta^2$ for all n, indicate that the Mn clusters around As are energetically favorable and we, therefore, argue that they are, likely to be, present in the low temperature molecular beam epitaxy (MBE) grown (GaMn)As/(InMn)As.

6.3.3 Magnetic moment

The next obvious question is what happens to the nature of Mn-Mn magnetic coupling in these As@Mn_n clusters due to single As-doping? The total magnetic moment of the corresponding ground states and closely lying isomers are given in Table 5.1 and Table 5.3 for pure Mn_n clusters and in Table 6.1 and Table 6.2 for As@Mn_n clusters, respectively, and are plotted in Fig. 6.4 for the ground states. Pure Mn_n clusters in the size range $n \leq 4$ have collinear ground state and the Mn-Mn coupling is ferromagnetic. These clusters have

a 5 μ_B/atom magnetic moment which is the Hund's rule value for the isolated Mn-atom. The magnetic moment per atom decreases drastically at and after n =5 and the magnetic ground states start to be non-collinear for $n \geq$6. However, we have found many collinear and non-collinear isomers with varying magnetic moment which are close in energy (not shown in Fig. 6.4, see for instance Table 6.1 and Table 6.2).

The large moment of pure Mn$_n$ and As@Mn$_n$ clusters arise from localized 3d electrons at Mn-atoms. However, the strong p−d hybridization induces a small negative polarization to the As-atom. For example, this negative polarization is 0.26 μ_B for Mn-As dimer. However, this negative polarization decreases non-monotonically to 0.01 μ_B for As@Mn$_{10}$ cluster. Generally, the total magnetic moment of As@Mn$_n$ cluster is lower than the corresponding pure Mn$_n$ cluster due to the $p-d$ hybridization. Similar to their pure counterparts, the Mn-Mn coupling in As@Mn$_2$ and As@Mn$_4$ collinear ferromagnetic and the emergence of non-collinear ground state is seen at and above n=6. We have plotted

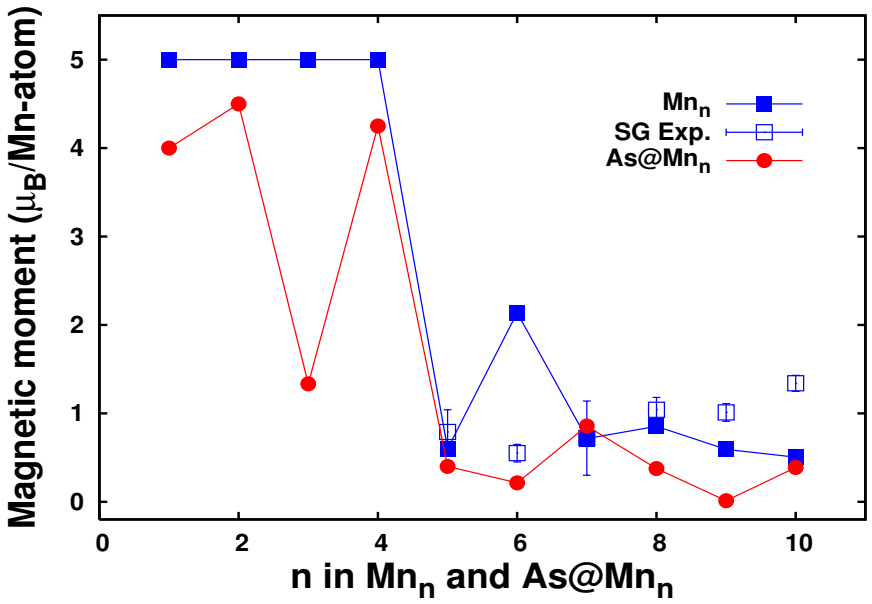

Figure 6.4: Plot of magnetic moment per atom as a function of n for pure Mn$_n$ and As@Mn$_n$ clusters. Values only for the ground states have only been shown (see Table 5.1 and Table 5.3 for Mn$_n$ isomers and Table 6.1 and Table 6.2 for As@Mn$_n$ isomers). The SG experimental values for pure Mn$_n$ clusters are shown with error bars.

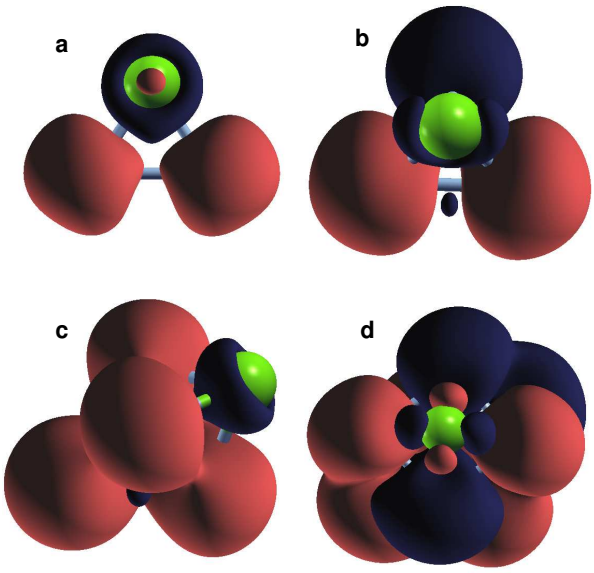

Figure 6.5: Constant spin density surfaces for (a) As@Mn_2, (b) As@Mn_3, (c) As@Mn_4 in their respective collinear ground state and (d) collinear isomer (3 μ_B ΔE = 120 meV) of As@Mn_8 clusters corresponding to 0.04, 0.04, 0.04 and 0.02 $e/\mathring{A}^3$, respectively. Red and blue surfaces represent positive and negative spin densities, respectively. Green ball is the As atom, which has negative polarization in all these structures. Note ferromagnetic (As@Mn_2 and As@Mn_4) and ferrimagnetic (As@Mn_3 and As@Mn_8) coupling between Mn atoms.

the constant spin density for collinear magnetic structures in Fig. 6.5. It is clear for the figure that the Mn-Mn coupling in As@Mn_2 and As@Mn_4 clusters are ferromagnetic, whereas the same is ferrimagnetic for As@Mn_3 and for a collinear isomer of As@Mn_8 clusters.

6.3.4 Exchange coupling

To further investigate the magnetic coupling behaviour we calculate exchange interactions J_{ij}'s for the GS geometry, the magnetic energy is mapped onto a Heisenberg form:

$$\mathcal{H} = -\sum_{i,j} J_{ij}\mathbf{S}_i \cdot \mathbf{S}_j, \tag{6.3}$$

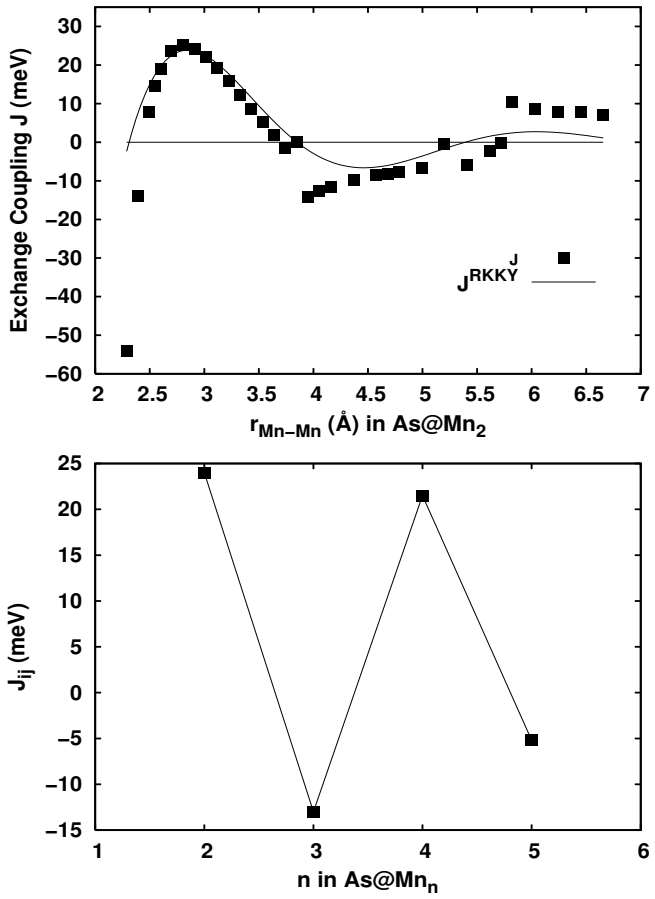

Figure 6.6: (Upper panel) Dependence of exchange coupling J on the Mn-Mn spatial separation $r_{\mathrm{Mn-Mn}}$ for Mn_2As cluster. Solid curve is the simplest RKKY form $J_{\mathrm{RKKY}} \propto r^{-3}\cos(2k_F r)$ fitted with $k_F = 1.02$ Å^{-1}. Solid line shows excellent agreement between the calculated $J(r)$ and the RKKY model. (Lower Panel) Plot of averaged exchanged coupling $\bar{J}_{ij}$ with r for As@Mn$_n$ (n=2-5).

where $\mathbf{S}$ are localized magnetic moments at Mn-sites.In clusters, due to the reduced symmetry and bonding anisotropy $|\mathbf{S}_i|$ vary from site to site and, therefore, rather than the conventional $|\mathbf{S}_i| = 1$ consideration, we take $\mathbf{S}_i$ as the projected magnetization density onto a sphere of radius 1.2 Å. Now we can calculate J_{ij} by computing the total energy for judicious choice of spin configurations with inequivalent combinations of pair correlation functions $\mathbf{S}_i \cdot \mathbf{S}_j$, which results in a set of linear equations for the J_{ij}'s. Calculated exchange coupling behaves anomalously to the RKKY-type predictions: J increases with

the concentration as $n^{1/3}$ at 0K and are independent of environment at fixed n. For As@Mn_2 cluster, exchange coupling $J(r)$ oscillates between positive and negative with $r_{\mathrm{Mn-Mn}}$ favoring FM and AFM solutions, respectively, as well as dies down as $1/r^3_{\mathrm{Mn-Mn}}$ (Fig. 6.6(a)), which is a typical RKKY-type behavior. But interestingly in contradiction with the RKKY-type predictions, we find the averaged exchange coupling $\bar{J}_{ij}$ decreases as n increases in As@Mn_n (Fig. 6.6), however, has a very large value $\sim$ 21 meV for FM As@Mn_4 and $\bar{J}_{ij}$ has strong environment dependency.

6.4 Summary

In summary, we have studied the electronic and magnetic properties of pure and As-doped manganese clusters, where, for both the cases, we find, the NCL treatment of atomic spins is important. FM to ferrimagnetic transition takes place at n =5 for pure manganese clusters. Single As-doping in the Mn_n clusters enhances the BE of resultant As@Mn_n clusters substantially. The subsequent larger energy gain in adding an As-atom to a Mn_n cluster than that of adding a Mn-atom ($\triangle^1 >> \triangle^2$) clearly indicate the tendency of Mn 'clustering' around As. The individual magnetic moment of the Mn atoms couple ferromagnetically only in As@Mn_2 and As@Mn_4 and are ferrimagnetic in nature for all other sizes studied here, whereas N-Mn_n ($n \leq 5$) were predicted to be all ferromagnetic [102]. However, for both pure and doped clusters, several different magnetic solutions close to the GS are possible [80]. In As@Mn_n clusters, As-atom induces FM order among its nearest neighbour Mn-atoms and calculated exchange coupling are anomalous and behave quite differently from the RKKY-type predictions. Present results can plausibly be discussed in the context of semiconductor ferromagnetism. The Mn clustering, during the low temperature MBE growth, is energetically favourable and their presence even after annealing at low (growth) temperature [154] could be responsible for the ferromagnetism and for the wide variation of Curie temperature observed in the (GaMn)As samples and should be taken into account to formulate an adequate theory of ferromagnetism in the III-V semiconductors [152]. This study points out that the ferromagnetic ordering of Mn-atoms are intrinsic for As@Mn_2 and As@Mn_4 clusters and the source of effective internal magnetic field, which influences energy structure and transport. They provide the high

temperature ferromagnetic contribution to the total magnetization. However, Xu and Schilfgaarde [158] recently studied clustering effect and found that clustering decreases Curie temperature whereas ordering increases it. But their study does not infer about any particular sized cluster. Moreover, we should note that, in dilute magnetic semiconductors the Curie temperature is controlled by the inter cluster couplings which are of long range in case of (GaMn)As [173]. The oscillatory behaviour of exchange coupling J (Fig. 6.6) will induce frustration which eventually could destabilize the ferromagnetism. The gas phase experiments involving Mn clustering in a As-seeded chamber can yield the direct information on the magnetic behavior of As@Mn_n clusters. We hope, our study will encourage such experiments.

Chapter 7

Structure, bonding and magnetism in Co_n clusters

In the chapters 4, 5 and 6, we have discussed the structural and magnetic properties of pure and As-doped manganese clusters. In this chapter, we will discuss the structure, bonding and magnetic behaviour of cobalt clusters in the size range of 2-20 atoms. We will discuss that in the intermediate size range cobalt clusters adopt hcp structure. This phenomena is quite different from the other $3d$ transition metal clusters. We discuss how magnetic moment is related to the average bond length and average coordination number[1].

7.1 Introduction

Early transition metals in the periodic table are non-magnetic in bulk solids, and only Fe, Co and Ni are known to be ferromagnetic among the $3d$ metals. However the small clusters of early transition metals are magnetic and those of late transition metals possess enhanced magnetic moments. For examples, chains of ferromagnetic atoms are more magnetic than the planes, and the planes are more magnetic than the bulk.

For bulk cobalt, fcc phase is the lowest in energy in the paramagnetic state. However, spin polarized calculation for ferromagnetic cobalt, confirms the hcp phase as the ground state due to magnetic ordering [182]. This indicates a strong correlation between the stable structure and magnetism. Again the stable magnetic state of cobalt is ferromagnetic for

[1]This chapter is based on the following paper:
(1) S. Datta, **Mukul Kabir**, S. Ganguly, Biplab Sanyal, T. Saha-Dasgupta and A. Mookerjee, *Structure, bonding and magnetism in cobalt clusters.*, Submitted to Phys. Rev. B (2006).

all crystal structures, although a metastable antiferromagnetic state exists. This is in contrast with other transition metals Mn, Cr and Fe which have a stable antiferromagnetic structure in their fcc phase. This means not only the crystal structure, but also the electronic configuration controls the magnetism. Cobalt atom has ground state electronic configuration as $3d^7 4s^2$, whereas the excited state $3d^7 4s^2$ is 0.418 eV higher [183].

As we have been discussed in chapter 1, the magnetic properties of bare cobalt clusters were first investigated via Stern-Gerlach molecular beam deflection approach by Bloomfield and co-workers (Co_{20}-Co_{215}) [184] and by De Heer and coworkers (Co_{30}-Co_{300}) [21]. These studies showed that in the temperature range of 77-300 K cobalt clusters are superparamagnetic and thus display magnetizations that increases with increasing magnetic field but decreases with increasing temperature. For small clusters, the intrinsic per-atom magnetic moments were found to be substantially larger than the bulk value, decreasing in a monotonic way with increasing size and eventually reaching the bulk value at ≈ 500 atoms. We are highly motivated by the recent experiment of de Heer *et al.* (Co_{12}-Co_{200}) [23] and most recent experiment of Knickelbein (Co_7 - Co_{32}) [22]. Here they came down to very small cluster size ($n = 7$), they got enhanced magnetic moment per atom compared to bulk value and the enhancement has been attributed to the lower coordination of the surface atoms which results in a narrowing of the d-band and thus greater spin polarization.

Information on the ground state geometry of the transition metal clusters are usually obtained from experiments involving chemical probe methods and photoelectron spectroscopy. However, such study for cobalt cluster is very limited and controversial. The chemical probe experiments [185] indicates strong evidence for icosahedral packing for hydrogenated cobalt and nickel clusters in the 50 to 200 atom size range. Although the structure of ammoniated iron, cobalt and nickel clusters in the size range from 19 to 34 atoms has been investigated [186] and it has been mentioned there that the bare clusters probably adopt a variety of structure. The photoionisation experiments [187], showed icosahedral atomic shell structures of large nickel and cobalt clusters of 50-800 atoms. However structure was not well identified for small cobalt clusters ($n \leq 50$) because subshell closings are close together in the different growth sequences. Bucher *et al.* [184] showed that a structural transition occurs and the isomers of different magnetic moments

exist in the size range 55-66.

The theoretical work on cobalt cluster is also limited and results are contradictory. Li and Gu performed first principle calculation of small cobalt clusters ($4 \leq n \leq 19$) using spin-polarized discrete variational method within local density functional theory [188]. But they have not optimized the structure and taken some special structures with lattice parameters same as bulk. Guevara *et al.* used an unrestricted Hartree-Fock tight-binding formalism [189], starting from an *spd*-bulk parametrization, although they only considered fixed bcc and fcc geometries of upto 177 atoms without structural optimization. Andriotis and Menon also used a tight-binding model coupled with molecular dynamic scheme [190]. Their calculated structures are mainly a combination of fcc and hcp relaxed geometries and some icosahedron for particular cluster sizes. Castro *et al.* performed all-electron density functional calculations using both the local density approximation and generalized gradient approximation and correlated the bonding character of $3d4s$ electrons with the structural, binding and magnetic properties. However, the size of the cluster was limited only up to 5 atoms. Recently, Lopez at al. studied Co cluster ($4 \leq n \leq 60$), where minimization was done using an evolutive algorithm based on a many-body Gupta potential and magnetic properties have been studied by a *spd*- tight-binding method [191]. As compared to *ab initio* methods, the parametrized tight-binding Hamiltonian reduces the computational cost drastically, but its main problem is the lack of transferability of its parameters. Here we have used first principle density functional theory allowing full relaxation of the atoms in free cobalt clusters without any symmetry constraints and the main purpose of this work is to show how the electronic as well as magnetic properties evolve with the increase of cluster size.

7.2 Computational Details

The calculations are performed using density functional theory (DFT), within the pseudopotential plane wave method. We have used projector augmented wave (PAW) method [59, 60] and Perdew-Bruke-Ernzerhof (PBE) exchange-correlation functional [48] for spin-polarized generalized gradient correction (GGA) as implemented in the Vienna *ab-initio* Simulation Package (VASP) [112]. The $3d$ and $4s$ electrons are treated as valence electrons

and the wave functions are expanded in the plane wave basis set with the kinetic energy cut-off 335 eV. Reciprocal space integrations are carried out at the Γ point. Symmetry unrestricted geometry and spin optimizations are performed using conjugate gradient and quasi-Newtonian methods until all the force components are less than a threshold value 0.005 eV/Å. Simple cubic supercells are used with the periodic boundary conditions, where two neighboring clusters are kept separated by at least 12 Å vacuum space. For each size, several initial geometrical structures have been considered. To get the ground state magnetic moment we have explicitly considered *all possible* spin configurations for each geometrical structure.

7.3 Results and discussions

7.3.1 Small Clusters : Co_2 - Co_{10}

Calculated binding energies, relative energies to the ground state and magnetic moments are given in the Table 7.1 for $n = 2-14$ and in Table 7.2 for $n = 15 - 20$ atom clusters. Both experimental and theoretical predictions of the true ground state of the Co_2 dimer is controversial. The first experimental estimation of cobalt dimer bond length and binding energy has been made by mass- spectroscopic technique [195], which are 2.31 Å and 1.72 eV, respectively. However, more recent collision-induced dissociation (CID) experiment [192] has been estimated a lower bound (1.32 eV) to the dimer dissociation energy. The present PAW pseudopotential calculation with PBE exchange correlation functional, gives dimer binding energy as 1.4522 eV/atom and a bond length of 1.96 Å, which is 78% of the bulk hcp cobalt. The cobalt atoms in dimer has bonding configuration nearer to $3d^8 4s^1$ pattern than that of the isolated Co atom, which is $3d^7 4s^2$. Therefore, in addition to the highly delocalized $4s$ electrons, the more localized $3d$ electrons also contribute to the bonding, which, consequently, produces a shorter bond length for the dimer. Leopold and Lineberger [193], by photoelectron spectroscopy on Co_2, have found that the $3d$ electrons contribute strongly to the bonding. Compared to neutral cobalt dimer, the CID experiment [192] gave high value of bond dissociation energy for cobalt dimer cation Co_2^+ which is formed by combining a ground state atom Co ($3d^7 4s^2$) with a ground state atomic ion Co^+ ($3d^8$) and, therefore, no promotional energy is required to form cationic dimer.

Infact, the bonding in Co_2^+ is relatively strong compared with other first-row transition metal dimer cations [194]. On the other hand, formation of neutral cobalt dimer requires promotion of both the ground state atoms to Co ($3d^8 4s^1$), which is 0.42 eV above the ground state ($3d^7\ 4s^2$) configuration. We found that Co_2 dimer has a total magnetic moment of 4 μ_B, which is also consistent with earlier mass spectroscopic measurement [195]. The bond length of a cobalt dimer suggested by Shim and Gingerich [196], on the basis of their HF-CI calculations, is 2.43 Å [196], which is much higher than the present value. However, the present value for the bond length and binding energy agrees with the previous first-principles calculations [197, 198, 120].

For Co_3 cluster, we have studied linear and triangular structures. An isosceles triangle with total magnetic moment 5 μ is found to be the ground state with binding energy 1.7834 eV/atom. Each of the two equal sides has length 2.19 Å and other one has length 2.10 Å. Another isosceles triangle with two long and one short bond lengths of 2.25 Å and 2.06 Å is found to be nearly degenerate with the ground state (lies only 0.003 eV higher in energy). According to the present calculation, the linear structure with a total magnetic moment of 7 μ_B is about 0.4302 eV higher than the ground state. The spin resonance spectra of Co_3 in Ar/Kr matrix, indicated a triangular structure and a total spin of 5 or 7 μ_B [184]. The CID study predicts a dissociation energy greater than 1.45 eV and Co_3^+ cation bond energy is larger than neutral Co_3. Yoshida *et al.* [199] reported that Co_3^- has a linear structure with bond distance of 2.25 - 2.5 Å based on their photoelectron spectra study. The all-electron (AE) density functional calculation [197] reported that the equilibrium structure for Co_3 is an isosceles triangle with bond lengths (2.12, 2.12, 2.24 Å), which has 1.7 μ_B/atom magnetic moment. While the tight-binding study [190] reported an isosceles triangular structure with much larger bond lengths (2.55, 2.69, 2.69 Å) to be the ground state, which has comparatively large magnetic moment, 2.33 μ_B/atom.

The experimental results on Co_4 is very limited. The CID study gave a dissociation energy of 2.41 eV. [192] Youshida *et al.* [199] found a tetrahedral structure with a bond length of $\approx$ 2.25±0.2 Å as the ground state for Co_4^- cluster anion. We examined with three different configurations for neutral Co_4 cluster: tetrahedral, rectangular and linear structures. A distorted tetrahedron with a total magnetic moment of 10 μ_B is appearing as the most stable structure, which has 2.2743 eV/atom energy and the average bond

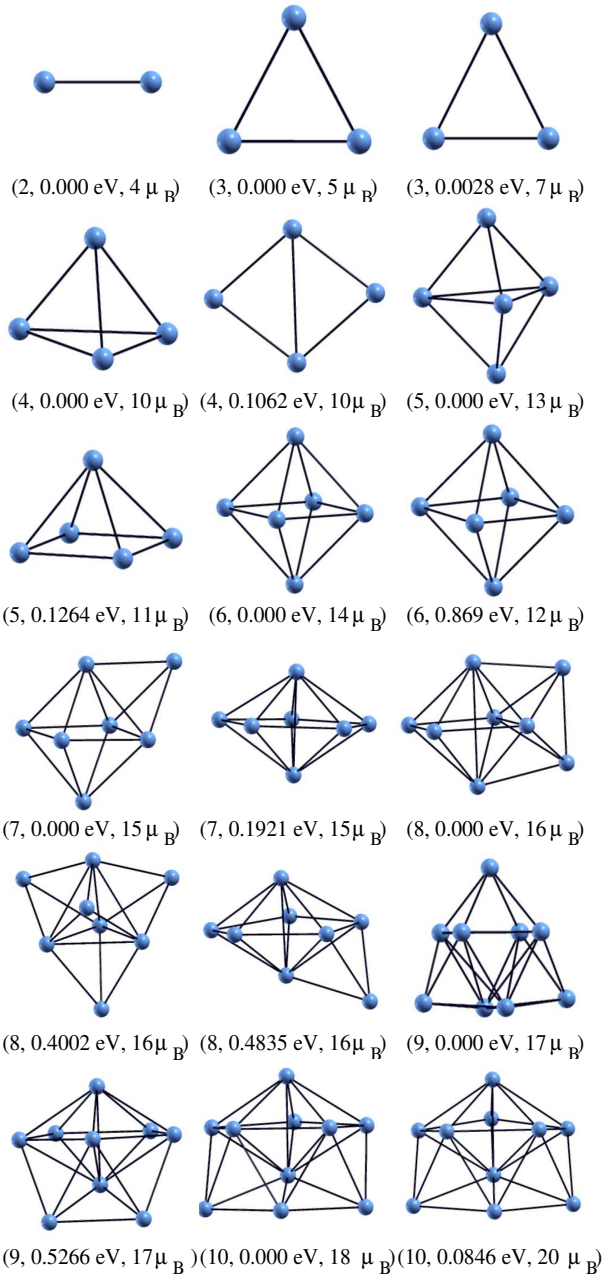

Figure 7.1: Equilibrium geometries of the energetically lowest isomers of cobalt cluster for n = 2-10. Numbers in the parenthesis represent number of atoms in the cluster, relative energy to the ground state and total magnetic moment, respectively.

length is found to be 2.3356 Å. Among the six sides of this tetrahedral ground state, two pairs have equal length of 2.14 Å, while the third pair is much larger, 2.72 Å. The initial rectangular structure becomes a rhombus after optimization, which has a total magnetic moment of 10 μ_B and lies 0.1062 eV higher in energy, is the next energetically favourable state, which has sides of length 2.14 Å and two diagonals of 2.67 Å and 3.35 Å. Our results for Co_4 are consistent with previous calculations [197, 191, 188, 190, 189]. Castro *et al.* [197] also predicted a strong Jhan-Teller distorted tetrahedron with bond lengths almost equal to the present value, as the ground state structure. The distorted tetrahedral ground state structure is accomplished by a reduction of some interatomic distances (and the enlargement of other bonds) until some short equilibrium bond lengths result for which there is a more effective participation of the (short range) $3d$-electrons in the bonds. In fact, in the distorted tetrahedron, there are some bond lengths (these are always on opposite TM-TM sides), which have values close to that of the dimer; these bonds have high $3d$ contributions and they are, therefore, the major source of increase of the bonding in the distorted structures. For both the ground states and the first isomer, the magnetic moment is found to be 2.5 μ_B/atom. The optimal linear structure is much more higher in energy than the ground state.

We took trigonal bipyramid, square pyramid and two planar structures viz. a double triangle connected at a vertex and a pentagon as the initial structures for Co_5 cluster. The trigonal bipyramid with total magnetic moment 13 μ_B is the most stable structure with 2.553 eV/atom binding energy and average bond length of 2.339 Å. In this most stable configuration, there are two types of bond lengths: upper three sides of top triangular pyramid and lower three sides of bottom triangular pyramid, all have same length of 2.18 Å, while each side of the interfacing planar triangle is much larger, 2.65 Å. Another triangular bipyramid of total magnetic moment 11 μ_B and a square pyramid of total magnetic moment 11 μ_B are appearing as degenerate first isomer ($\sim$ 0.125 eV above from ground state). The optimal planar pentagon with a magnetic moment 11 μ_B lies much, 1.0375 eV, higher and the double triangle structure is even higher in energy from ground state. Previous all-electron calculation with GGA functional by Castro *et al.* [197] predicted a triangular bipyramid with average bond length 2.28 Å and magnetic moment 2 μ_B/atom to be the ground state. Lopez *et al.* [191] also got a trigonal bipyramidal

structure as the ground state with average bond length of 2.37 Å, but their magnetic moment is quite high 2.94 μ_B/atom.

We have studied caped trigonal bipyramid, octahedron and pentagonal pyramid to search the ground state for Co_6 cluster. From now on for the larger clusters, the planar structures have been discarded by intuition. Here a octahedral structure with 14 μ_B total magnetic moment is found to the ground state. An initial caped triangular bipyramidal structure relaxes to an octahedron with 14 μ_B magnetic moment. Each side of this octahedron is about 2.27 Å and has binding energy of 2.929 eV/atom. Another slightly distorted octahedron of total magnetic moment 12 μ_B appears as the first isomer. However, it is 0.869 eV higher compared to the ground state. The first isomer predicted by Lopez *et al.* [191] is different from our, which is a caped trigonal bipyramid. The optimal pentagonal pyramid lies much higher, 1.7 eV, in energy compared to the ground state and this has a total magnetic moment of 12 μ_B. Comparing with previous theoretical studies [191, 188, 200, 198], we can say, that the octahedral structure is generally accepted as the most stable structure for Co_6. Although, the tight-binding calculation [190] predicted a different geometry with T_d symmetry. Both the local density approximation calculation [188] and the tight-binding calculation [188] predicted same magnetic moment as the present value. However, the tight-binding calculation [190] gives much larger average bond length, 2.76 Å, while Lopez *et al.* [191] predicted a quite higher magnetic moment, 2.73 μ_B for the ground state. The CID experiment [192] estimated a bond dissociation energy as 3.31 eV. Yoshida *et al.* [199] showed by photoelectron spectroscopy study that pentagonal pyramid with bond distances $\sim 2.75 \pm 0.1$ Å is the most probable structure for Co_6^- anion cluster, i.e. the structure is strongly correlated with the charged state of the cluster.

For Co_7 cluster, the closed packed structures are caped octahedron, pentagonal bipyramid and bicaped triangular bipyramid. However, after geometry optimization, caped octahedron with total magnetic moment 15 μ_B is appearing as the most stable structure with average bond length 2.29 Å, which has 2.9711 eV/atom binding energy. The experimentally measured magnetic moment is 2.359 ± 0.248 μ_B [22], which is a little bit higher than our results. The dissociation energy is predicted to be 2.65 eV by the CID experiment [192]. The optimal pentagonal bipyramid has a total magnetic moment of 15

μ_B, which lies 0.1921 eV higher in energy from the ground state. This is the first isomer, which has an average bond length of 2.3159 Å. Another pentagonal bipyramid of total magnetic moment 13 μ_B, which lies 0.3515 eV higher in energy from the ground state is the second isomer and a bicaped triangular bipyramid with total magnetic moment 15 μ_B, which lies 0.4219 eV higher is the third isomer. The previous theoretical results are quite contradictory to our results. Using Gupta potential, Lopez *et al.* [191] found a pentagonal bipyramidal structure as the ground state, which has an average bond length of 2.40Å and 2.81 μ_B/atom magnetic moment and predicted a caped octahedra as the first isomer. Fan *et al.* [198] also favoured a pentagonal bipyramidal structure with 15 μ_B magnetic moment as the most stable structure.

We have studied three different geometries for Co_8, viz., bicaped octahedron, caped pentagonal bipyramid and tricaped triangular bipyramid. The bicaped octahedron with total magnetic moment 16 μ_B is the most stable structure, which has 3.0736 eV/atom binding energy and 2.304 Å as average bond length. The experimental bond dissociation energy is predicted to be 2.93 eV [192] and the magnetic moment is predicted to be, 2.510 $\pm$ 0.154 μ_B/atom [22], which is higher than the present value. The optimal tricaped triangular bipyramid with total magnetic moment 16 μ_B lies 0.4 eV higher in energy from the ground state is predicted to be the first isomer. This isomer has an average bond length of 2.309 Å. The optimal caped pentagonal bipyramid with magnetic moment 16 μ_B and average bond length of 2.324 Å is found to be the second isomer, which lies 0.4835 eV higher in energy. Lopez *et al.* [191] found a bicaped octahedral structure as the most stable structure with an average bond length of 2.39 Å and a magnetic moment of 2.69 μ_B/atom. Guevera *et al.* [189] found a magnetic moment of their nonoptimized Co_8 structure as 2.25 μ_B, which is in between our and the experimental value.

For the Co_9 cluster, we took tricaped octahedron and bicaped pentagonal bipyramid as the initial configurations. A distorted tricaped octahedron is found to be the most stable structure with 3.1428 eV/atom binding energy, which has 17 μ_B total magnetic moment. The experimentally predicted magnetic moment, 2.38 $\pm$ 0.11 μ_B/atom [22], is higher than the present value and the experimental dissociation energy is found to be 2.89 eV [192]. The optimal bicaped pentagonal bipyramid with a total magnetic moment of 17 μ_B, which lies 0.5266 eV higher in energy, is the first isomer. The average bond

length for these two structures are 2.309 and 2.336 Å, respectively. However, Lopez *et al.* [191], found a bicaped pentagonal bipyramid as the ground state, which had a magnetic moment of 2.63 μ_B/atom.

Different tricaped pentagonal bi-pyramid structures (TCPBP) along with different tetra capped octahedral structures were taken as initial structures for Co_{10} cluster. A TCPBP structure with 18 μ_B total magnetic moment is found to be the ground state. This ground state has an average bond length of 2.347 Å and has 3.1365 eV/atom binding energy. Experimental measured value is 2.07 $\pm$ 0.10 μ_B. The CID study [192] predicted the bond dissociation energy of Co_{10} cluster to be 3.05 eV. Our predicted magnetic moment is quite smaller compared to those of its neighbours which is indeed the case in experimental scenario. This is because of the fact that TCPBP is an icosahedral fragment. For this structure average coordination and average bond lengths are slightly higher and the competing effect of these two makes the magnetic moment smaller than its neighbouring clusters. Another TCPBP with total magnetic moment 20 μ_B which lies 0.0846 eV higher in energy compared to ground state is the first isomer. This structure has 2.355 Å average bond length. Lopez *et al.* [191] predicted a TCTBP structure with 2.45 μ_B/atom magnetic moment as the ground state, whereas Guevara *et al.* [189] predicted a fcc structure with magnetic moment 2 μ_B/atom.

7.3.2 Intermediate size clusters: Co_{11} - Co_{20}

As the number of atoms in the cluster increases, the determination of the ground state become a difficult task as the number of minima in the potential energy surface increases with the number of atoms in the cluster. However, for each cluster we have considered several possible geometrical structures as initial guess and we relax all of them for all possible spin multiplicities. The predicted ground state structure along with an another isomer for each cluster have been shown in Fig. 7.2.

A 13-atom close packed hexagonal structure consists of a hexagonal ring around a central atom and two triangular planes above and below it i.e. 3,7,3 stacking, while a 13-atom closed packed icosahedral structure has two pentagonal rings, two apex points and a central point i.e. of 1,5,1,5,1 stacking. The initial structures for both the Co_{11} and Co_{12}

Table 7.1: Binding energy, relative energy to the GS ($\triangle E = E - E_{GS}$) and magnetic moment (with a comparison to the SG experiment [22]) for Co_n (n = 2-14) clusters.

Cluster	E_b (eV/atom)	$\triangle E$ (eV)	Magnetic Moment (μ_B/atom)	
			Theory	SG Exp. [22]
Co_2	1.4522	0.0000	2.00	–
Co_3	1.7834	0.0000	1.67	–
	1.7825	0.0028	2.33	
Co_4	2.2743	0.0000	2.50	–
	2.2478	0.1062	2.50	
Co_5	2.5530	0.0000	2.60	–
	2.5279	0.1253	2.20	
Co_6	2.9290	0.0000	2.33	–
	2.7842	0.8690	2.00	
Co_7	2.9711	0.0000	2.14	2.359 ± 0.248
	2.9437	0.1921	2.14	
Co_8	3.0736	0.0000	2.00	2.510 ± 0.154
	3.0235	0.4002	2.00	
	3.0134	0.4835	2.00	
Co_9	3.1428	0.0000	1.89	2.385 ± 0.108
	3.0842	0.5266	1.89	
Co_{10}	3.1365	0.0000	1.80	2.072 ± 0.10
	3.1280	0.0846	2.00	
Co_{11}	3.2048	0.0000	1.91	2.422 ± 0.085
	3.2033	0.0161	1.91	
Co_{12}	3.2517	0.0000	2.00	2.257 ± 0.085
	3.2431	0.1025	1.89	
Co_{13}	3.2790	0.0000	1.92	2.297 ± 0.070
	3.2683	0.1396	2.08	
	3.2662	0.1666	2.38	
Co_{14}	3.3225	0.0000	2.00	2.289 ± 0.063
	3.3222	0.0044	2.00	
	3.3222	0.0053	1.71	
	3.3220	0.0071	1.86	
	3.3200	0.0075	2.14	

Table 7.2: Binding energy, relative energy to the GS ($\triangle E = E - E_{GS}$) and magnetic moment (with a comparison to the SG experiment [22]) for Co_n (n = 15-20) clusters.

Cluster	E_b (eV/atom)	$\triangle E$ (eV)	Magnetic Moment (μ_B/atom)	
			Theory	SG Exp. [22]
Co_{15}	3.3965	0.0000	2.07	2.381 ± 0.026
	3.3934	0.0462	1.93	
	3.3882	0.1245	2.20	
	3.3852	0.1687	1.80	
	3.3851	0.1709	1.93	
Co_{16}	3.4579	0.0000	2.13	2.531 ± 0.038
	3.4576	0.0050	2.00	
	3.4449	0.2081	1.88	
	3.4386	0.3076	2.25	
	3.4379	0.3192	1.88	
Co_{17}	3.5135	0.0000	2.06	2.240 ± 0.037
	3.5062	0.1232	2.18	
	3.5036	0.1672	1.94	
	3.4895	0.4073	1.82	
	3.4657	0.8124	2.06	
Co_{18}	3.5550	0.0000	2.00	2.072 ± 0.037
	3.5536	0.0244	2.11	
	3.5442	0.1944	1.89	
	3.5233	0.5714	2.00	
Co_{19}	3.6066	0.0000	2.05	2.209 ± 0.029
	3.5974	0.1738	1.95	
	3.5814	0.4782	1.84	
	3.5591	0.9011	1.74	
	3.5457	1.1575	2.16	
	3.5424	1.2199	1.95	
Co_{20}	3.6200	0.0000	2.00	2.037 ± 0.049
	3.6070	0.2621	1.90	
	3.5883	0.6335	1.80	
	3.5755	0.8910	2.10	
	3.5649	1.1030	1.90	

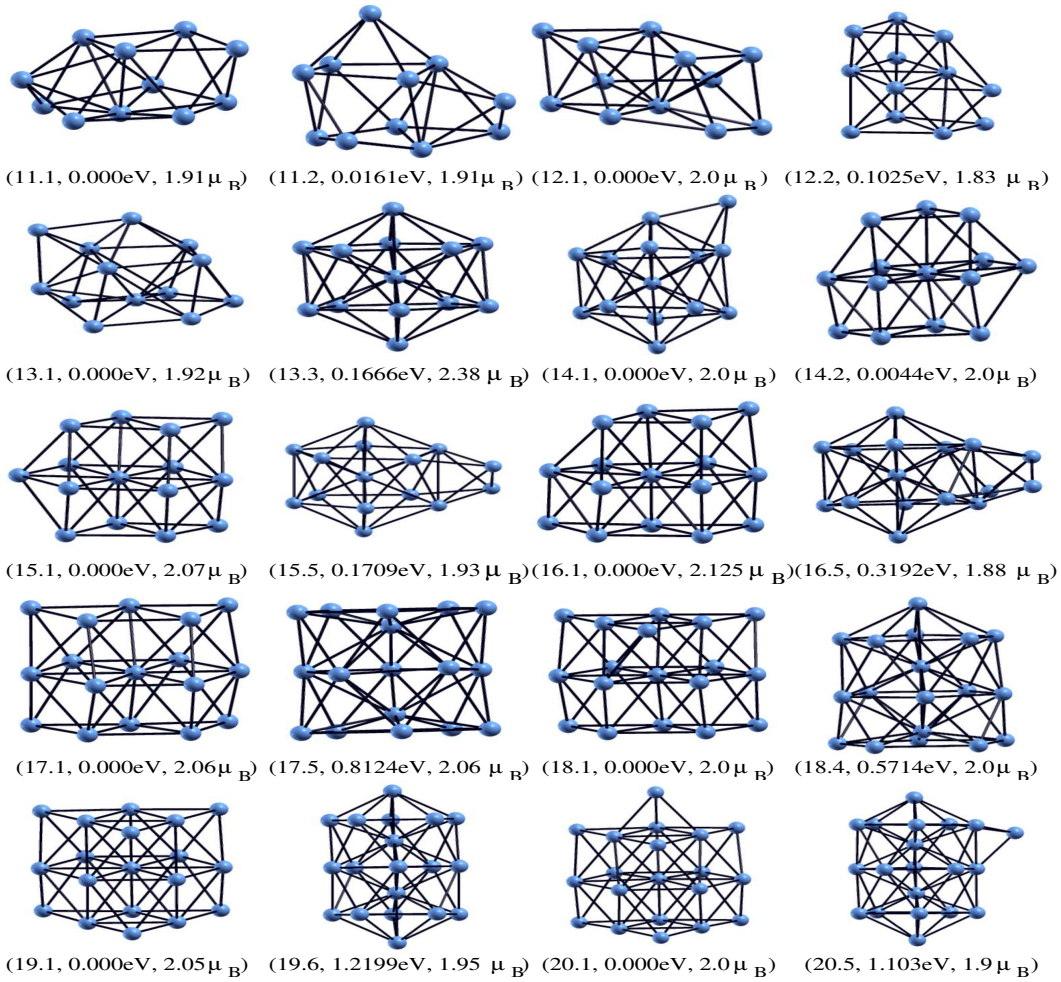

Figure 7.2: The ground state and a few higher energy structures for the size range $n = 11 - 20$. The first number in the parenthesis $n.k$ indicates that the structure corresponds to the k-th isomer of Co_n cluster. Second and third entries give the relative energy to the ground state and total magnetic moment, respectively of k-th isomer.

clusters, have been derived from these 13-atom closed packed structures by removing 1 or 2 atoms, respectively. As initial structures, we considered two hexagonal structures (4,7 and 3,5,3 stackings) and two icosahedral structures (5,1,5 and 1,5,1,4 stackings). After relaxation, all the structures are distorted heavily. The distortion of the 4,7 hexagonal structure is such that one atom from the hexagonal ring comes out of the plane and is the most stable configuration with binding energy 3.2048 eV/atom. This structure

has a total moment 21 μ. The experimentally measured magnetic moment, 2.42 $\pm$ 0.09 μ_B/atom [22] is considerably higher than the present value, 1.91 μ_B/atom. The initial 1,5,1,4 icosahedral structure is found to be the next isomer after relaxation, which is 0.0161 eV higher from ground state and has a total magnetic moment 21 μ_B.

For Co_{12}, we have tried with two hcp structures: one with 3,6,3 stacking (without the central atom) and the other with 2,7,3 stacking (with the central atom) and two icosahedral structures: a closed icosahedral structure without one apex atom and a closed icosahedral structure without the central atom. The initial hexagonal structures After relaxation the initial hcp structures undergo a considerable rearrangement to a structure, which consists of a plane of 7 atoms coupled with another plane of 5 atoms. This structure having a magnetic moment of 24 μ_B is the ground state, which has 3.2517 eV/atom binding energy. An structural rearrangement has also been seen for 1,5,5,1 icosahedral structure, which looks like a hcp fragment of 3,5,4 staking after relaxation. This structure has a magnetic moment of 22 μ_B and has 3.2431 eV/atom magnetic moment. The other icosahedral structure with 1,5,1,5 stacking does not lead to such rearrangement after relaxation. However, it lies much higher in energy compared to ground state. The ground state magnetic moment, agrees with the recent SG experiment [22] and the previous theoretical calculations as well [191, 189]

The obvious candidates for the Co_{13} cluster are the icosahedral, hexagonal close packed (HCP), cuboctahedral and face-centered cubic structures. The distorted hexagonal structure is found to be the ground state and it can be seen as the most stable Co_{11} with additional two caped atoms. This structure has total magnetic moment of 25 μ_B and has 3.279 eV/atom energy. Knickelbein found the experimental moment to be 2.297 $\pm$ 0.07 μ_B/atom [22], which is slightly higher than the present value, 1.92 μ_B/atom. However, this is in good agreement with Bucher *et al.* [184], who predicted 2.08 μ_B magnetic moment, which is rather close to the present value. Another distorted hcp structure with total magnetic moment 27 μ_B is found to the first isomer, which lies 0.1396 eV higher in energy. The optimal icosahedral structure has a total magnetic moment of 31 μ_B, which is 0.1666 eV higher in energy appears to be the second isomer. The optimal fcc and cubooctahedral structures are much higher in energy compared to the ground state. Because of close packness of the icosahedral structure, its average coordination is higher and the av-

erage bond length is smaller than the distorted hcp ground state. The present prediction of hcp ground state is in agreement with the previous calculations [190]. However, there are some other calculations [191, 200], which favour the icosahedral structure.

For Co_{14} cluster, the trial structures are a complete icosahedra with a single atom capping and a hexagonal with 3,7,4 stacking. Icosahedral structure with total spin 28 μ_B and the hexagonal structure with the same magnetic moment μ_B are almost degenerate. They are separated by only 0.0044 eV energy. However, we found several isomers which lie very close to these structures. An icosahedral structure of total magnetic moment 24 μ_B, an hexagonal structure of 26 μ_B and another icosahedra of total magnetic moment 30 μ_B lie only 0.0053 eV, 0.0071 eV and 0.0075 eV above the ground state,respectively. The very recent SG experiment has been predicted a magnetic moment of 2.289 $\pm$ 0.063 μ_B/atom for Co_{14} cluster. Guevara *et al.* [189] predicted a magnetic moment of fcc Co_{14} as 2.14 μ_B/atom and Lopez *et al.* [191] predicted it to be 2.38 μ_B/atom.

For the Co_{15} cluster, the hexagonal structure with 4,7,4 atomic staking is found to the ground state, which has 3.3965 eV/atom binding energy. This structure has 31 μ_B magnetic moment. The experimental [22] magnetic moment is slightly higher than the present value. The other hexagonal structures with total magnetic moments 29 μ_B, 33 μ_B and 27 μ_B lie 0.0462 eV, 0.1245 eV and 0.1687 eV higher than the ground state, respectively. The optimal icosahedral structure has 1,5,1,5,1,2 staking lies 0.1709 eV higher, which has 29 μ_B magnetic moment is the fourth isomer.

The same structural growth is observed in the case of Co_{16}. Hexagonal structure with a magnetic moment of 34 μ_B is found to be the ground state for Co_{16} cluster. This structure has a 4,7,5 staking and 3.4579 eV/atom binding energy. Another three hexagonal structures with magnetic moments 32 μ_B, 30 μ_B and 36 μ_B are found to be next isomers, which lie 0.005 eV, 0.2081 eV and 0.3076 eV higher in energy,respectively. The optimal icosahedral structures with 1,5,1,5,1,3 staking and with magnetic moments 30 μ_B and 32 μ_B lie 0.3192 eV and 0.3552 eV higher, respectively. The other icosahedral structure with 5,1,5,4 stacking is higher in energy.

The hexagonal structure with magnetic moment 35 μ_B is the ground state for Co_{17} cluster. This structure has 5,7,5 staking and 3.5135 eV/atom binding energy. The present moment, 2.06 μ_B is slightly smaller than the SG experimental value, 2.24 $\pm$ 0.04 μ_B/atom

[22]. The next three isomers are also hexagonal structures with magnetic moments 37 μ_B, 33 μ_B and 31 μ_B, which lie 0.1232 eV, 0.1672 eV and 0.4073 eV higher than the ground state,respectively. The 5,1,5,1,5 icosahedral structure with magnetic moment 35 μ_B, which lies 0.8124 eV higher is found to be the fourth isomer.

For Co_{18} cluster a hcp structure with 6,7,5 staking and a total magnetic moment of 36 μ_B is found to be the ground state. This has a binding energy of 3.6066 eV/atom. The magnetic moment is in agreement with the experimental value, 2.072 $\pm$ 0.04 μ_B/atom. The other two hcp structures of magnetic moments 38 μ_B and 34 μ_B, which are 0.0244 eV and 0.1944 eV higher in energy are the first and second isomers, respectively. The icosahedral structure of total magnetic moment 36 μ_B and which is 0.5714 eV higher is the the third isomer. Another hexagonal structure with total magnetic moment 32 μ_B is the fourth isomer, which lies 0.5939 eV higher in energy.

For Co_{19} cluster, we have investigated a double icosahedral stacking and a hcp structure with 6,7,6 staking and a cuboctahedral structure. The hcp structure with a total magnetic moment of 39 μ_B is the most stable structure with 3.6066 eV/atom binding energy. The predicted magnetic moment, 2.05 μ_B/atom, is in agreement with the recent SG experimental value, 2.209 $\pm$ 0.029 μ_B/atom [22]. The next four isomers are also found to be of same hcp packing. These isomers with magnetic moments 37 μ_B, 35 μ_B, 33 μ_B and 41 μ_B, which lie 0.1738 eV, 0.4782 eV, 0.9012 eV and 1.1575 eV higher than the ground state, respectively. On the other hand, the optimal icosahedral structure has a total magnetic moment of 38 μ_B, which lies 1.2199 eV higher from the ground state and is the fifth isomer. The fcc and hcp fragments have also been proposed in the previous theoretical calculations [188, 189], however, some calculations [191, 190] predicted icosahedral ground state for Co_{19}.

For Co_{20}, we have studied a hcp structure with a caped atom on the 19-atom hcp structure and an icosahedral structure which is a singly capped 19-atom double icosahedra. Again the hexagonal structure with 3.62 eV/atom binding energy is found to be the ground state. This hcp ground state has a magnetic moment of 40 μ_B, which is in agreement with the SG experimental value, 2.037 $\pm$ 0.049 μ_B/atom [22]. Similar to what we have seen for Co_{15}, Co_{16}, Co_{17}, Co_{18} and Co_{19} clusters, the next isomers are also of hcp motif. The hcp structures with magnetic moments 38 μ_B, 36 μ_B and 42 μ_B which are 0.2621 eV, 0.6335 eV

and 0.891 eV higher are found to be the first, second and third isomers, which lie 0.2621 eV, 0.6335 eV and 0.891 eV higher, respectively. The optimal icosahedral structure has total magnetic moment 38 μ_B, which lies 1.103 eV higher than the hcp ground state is the fourth isomer.

7.3.3 Binding energy, stability and dissociation energy

Calculated binding energies are are plotted in Fig.7.3 for Co_n clusters in the size range n =2-20. Since the coordination number increases with the number of atom in the cluster, the binding energy increases monotonically. The binding energy of the largest cluster studied here (Co_{20}) is 3.62 eV/atom, which is 83 % of the experimental bulk value, 4.40 eV/atom [182], for hcp cobalt. Upon extrapolation of the linear fit to the binding energy

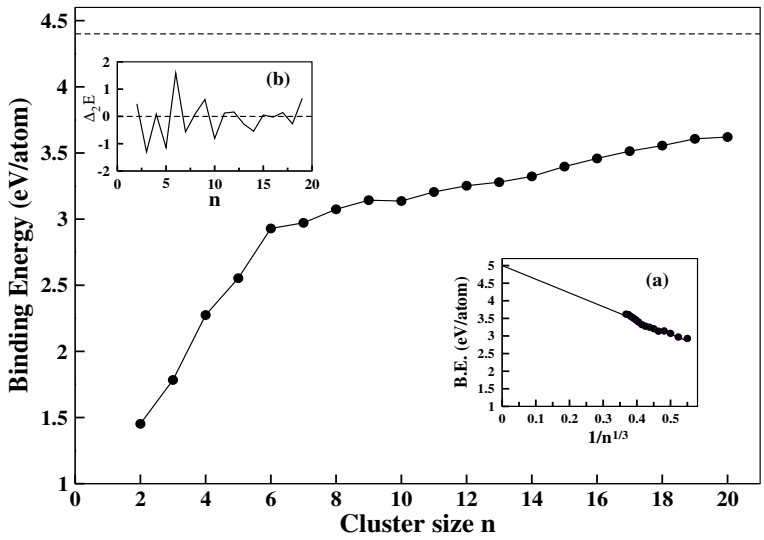

Figure 7.3: Plot of binding energy per atom as a function of cluster size n for the entire size range $2 \leq n \leq 20$. The dashed line corresponds to bulk binding energy per atom of cobalt. (a) Plot of second difference, $\Delta_2 E$ in total energy, which represents the relative stability.(b) Plot of the same as a function of $1/n^{\frac{1}{3}}$ for the clusters Co_n, $2 \leq n \leq 20$ and a linear fit (B.E. $= -3.90\frac{1}{n^{\frac{1}{3}}} + 5.00$) to the data.

per atom data to $n^{-1/3}$ (Fig.7.3(a)), we can estimate the binding energy of the infinitely large cluster. This is found to be 5 eV/atom, which is much larger than that of the hcp bulk cobalt, 4.40 eV/atom [182]. However, within the same level of theory we found the cohesive energy to be 5.11 eV/atom for hcp bulk cobalt. This overestimation is consistent with the previous DFT calculations [182].

A close investigation of the binding energy curve reveals kinks at $n = 6$, 9 and 19. These kinks represent enhanced stability compared to their neighbouring clusters. Therefore, it would be interesting to investigate the second difference in the total energy: $\Delta_2 E(n) = E(n+1) + E(n-1) - 2E(n)$, where $E(n)$ represents the total energy of an $n-$atom cluster. As $\Delta_2 E(n)$ represents the stability of the corresponding cluster compared to its neighbors, the effect will be prominent. $\Delta_2 E$ has been plotted in Fig.7.3(b), where we see the peaks at $n = 6$, 9 and 19. The stable structure for $n = 6$ is an octahedron and for $n = 9$, it is a distorted tricapped octahedron. Note that these two structures are the fragments of a hexagonal structure. The CID experiment has also been indicated a maximum at $n = 6$ in the measured dissociation energy, which indicates higher stability of the hexamer. The extra stability of hexamer indicates that the octahedral structure can be act as a building block for larger size clusters and, indeed, for Co_{15}-Co_{20} clusters, we have found a distinct hexagonal growth pattern and an octahedron is just a fragment of hexagonal structure. The calculated stability (Fig.7.3 (b)) shows minima at $n = 3$, 5, 7, 10 and 14, which are probably related to their weak bonding and low coordination compared to their neighbours.

This can be further demonstrated by studying the dissociation energies as a n-atom cluster fragments to m- and $(n-m)$-atom clusters. The m-channel dissociation energy can be calculated as,

$$D_m(n) = E(m) + E(n-m) - E(n), \tag{7.1}$$

where $E(n)$, $E(m)$ and $E(n-m)$ are the total energies of n, m and $n-m$ atom clusters, respectively. We have plotted the calculated single channel (D_1) and dimer channel (D_2) dissociation energies in Fig.7.4 and D_1 is compared with the CID experiment [192]. Hales *et al.* [192] estimated the single channel dissociation energy for the neutral Co_n clusters. However, they have estimated this dissociation energy through an indirect method: Actually, they have measured the dissociation energy by collision-induced dissociation of Co_n^+

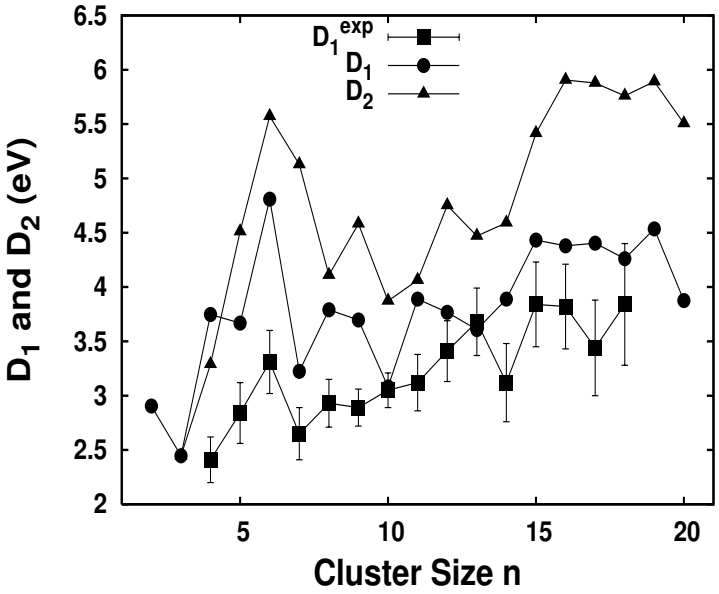

Figure 7.4: Plot of single channel, D_1 and dimer channel, D_2, dissociation energy as a function of n. We compare our calculated single channel dissociation with the CID experiment.

clusters and derived the same for the neutral Co_n clusters by using the ionization energies (IE) of the neutral Co_n clusters measured by Yang and Knickelbein [201], and Parks *et al.* [202], i.e. $D_1^{exp} = D_1(Co_n^+) + IE(Co_n) - IE(Co_{n-1})$. The calculated single channel dissociation energy, D_1 shows a peak at n =6 and deeps at n = 5, 7 and 10, which are consistent with the stability analysis. However, we do not find any deep in the dissociation energy at n =14, what has been seen in CID experiment. Generally the single channel dissociation energy is the most favourable except for n =4, where the dimer dissociation ($Co_4 \rightarrow Co_2 + Co_2$) is favorable than the single channel ($Co_4 \rightarrow Co_3 + Co$) dissociation.

To illustrate this we calculated the average bond lengths and average coordination number, which have been plotted in the Fig.7.5(a) and Fig.7.5(b), respectively, as a function of cluster size in their respective ground state. These two quantities are closely related to the structure of the cluster. We define the average bond length as $\langle r \rangle = \frac{1}{n_b} \sum_{i>j} r_{ij}$, where r_{ij} is the bond distance between the j-th and i-th atom, and n_b is the number of such bonds. Here we consider that two atoms are bonded if their interatomic distance is within 2.91 Å, which is around the average of the first (2.51 Å) and second (3.54

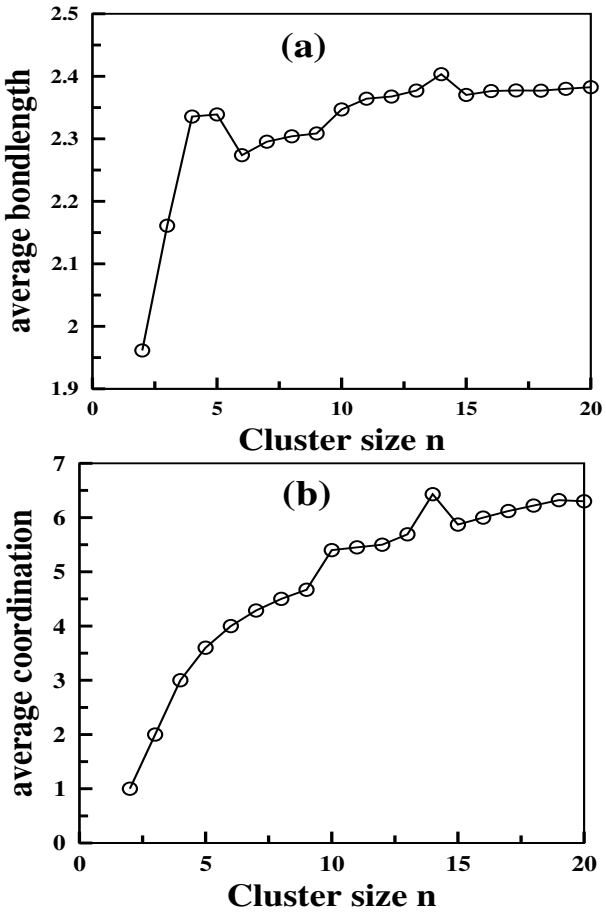

Figure 7.5: Plot of (a) average bond length and (b) average coordination, as function of cluster size.

Å) nearest-neighbour distances in bulk. The average coordination number in a cluster is defined as $\langle n_c \rangle = \frac{1}{n} \sum_k n_k$ where n_k is the number of neighbours within the chosen cut-off of the k-th atom in the cluster of n atoms.

The convergence of average bond length to the bulk value (2.51 Å) is much faster than the convergence of average coordination, which is far below the bulk value (12 for hcp Co). Deeps at $n = 6$ and 9 in Fig. 7.5(a) indicate that in these clusters are closely spaced and are more stable than the neighbouring structures. While the peeks $n = 5$, 10 and 14 in Fig. 7.5(a) and at $n = 10$ and 14 in Fig. 7.5(a) at $n = 14$ indicate those atoms in this cluster are quite far away than their respective neighbours. Note that for $n = 14$, two degenerate ground states have been observed: one with icosahedral symmetry and other

has hexagonal symmetry.

7.4 Magnetic moment

The calculated magnetic moments are plotted in Fig.7.6 as a function of cluster size (n). The Co-Co interaction is always ferromagnetic for the entire size range studied, as it is for hcp bulk cobalt. However, the magnetic moment (2−2.5 μ_B/atom) is larger than the hcp bulk value, 1.72 μ_B/atom [24]. This enhancement is moment in a few atom cluster can readily be understood from the more localized d-electrons resulting from the decrease in effective hybridization. The calculated magnetic moments are in good agreement with the very recent SG experiment by Knickelbein [22]. Fig.7.6 shows a qualitative agreement between the calculated and the experimental value, though the calculated moments are always underestimated. This may be due to the fact that we did not include the spin-orbit

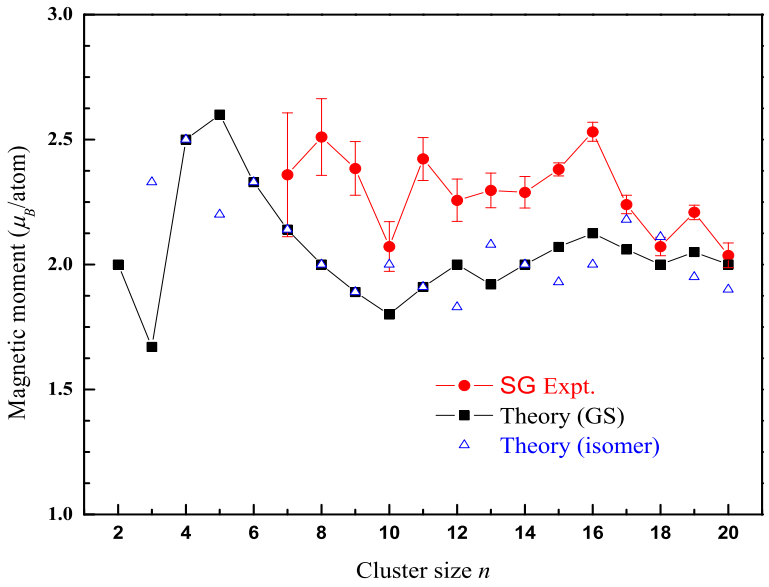

Figure 7.6: Size dependent variation of magnetic moment of the corresponding ground states. Calculated magnetic moments are compared with experimental results (Ref. [22]).

interaction in the present calculation. Moreover, it should remember that the magnetic moments in a magnetic deflection measurement are derived within a models, which may influence the value. For example, Knickelbein used either superparamagnetic or locked moment model to derive the moments experimentally for Co_n clusters [22].

The magnetic moment is strongly correlated with the effective hybridization, which is related to the average bond length and average coordination number. As the $\langle n_c \rangle$ decreases the the magnetic moment should increase through the decrease in effective hybridization. On the other hand, the dependency of magnetic moment on the $\langle r \rangle$ is directly proportional: A decrease in $\langle r \rangle$ results in decrease in magnetic moment through the enhancement in effective bonding. Fig.7.5(a) and Fig.7.5(b) show that as we go to $n = 4$ to n =10, both the $\langle r \rangle$ and $\langle n_c \rangle$ decrease, whereas Fig.7.6 shows that the magnetic moment per atom increases. Therefore, within these two competing contributions ($\langle r \rangle$ and $\langle n_c \rangle$) to the magnetic moment, the average coordination number dominates over the average bond length in the size range n =4-10.

In the intermediate size range, n =11-10, the variation of $\langle r \rangle$ (Fig.7.5a) and $\langle n_c \rangle$ (Fig.7.5b) is very slow with n, and therefore, the magnetic moment per atom does not vary rapidly, which are around 2 μ_B/atom for all the clusters in this size range. So, to illustrate the effect of $\langle r \rangle$ and $\langle n_c \rangle$ on the magnetism in this intermediate size range we compare these two quantities for the optimal hcp and icosahedral structures (see Fig.7.2). It has been seen that for a hcp, both the $\langle r \rangle$ and $\langle n_c \rangle$ are smaller than the corresponding icosahedral structure for a particular n-atom cluster. In addition the magnetic moments of optimal hcp clusters are always larger than or equal to that of the corresponding optimal icosahedral clusters, which again demonstrates that in this intermediate size range also the coordination dominates over the average bond length.

7.5 Conclusion

In this chapter we have discussed structure, bonding and magnetism in Co_n clusters in the size range n =2-20. In the intermediate size range clusters adopt hcp structural packing. The calculated magnetic moments are in good agreement with the recent SG experiment: they follow the same trend but are always underestimated. It is found that the effect of

average coordination number dominates over the average bond length to determine the effective hybridization and, therefore, the magnetic moment of the cluster.

Chapter 8

About this thesis and outlook

In this chapter we will discuss about the work done for this thesis. Chemical and magnetic interactions in low dimensional nanostructures give rise to novel properties. It is essential to understand these complex interactions in microscopic detail from the point of view of fundamental understanding and also due to enormous possibilities of technological applications. By the usage of the state of the art electronic structure techniques based on density-functional theory (DFT) as well as tight-binding method, my interest evolves with the microscopic detail of these systems, which is extremely useful for the fundamental understanding as well as manipulating electronic and magnetic properties of technologically important materials.

In this thesis, we have concentrated mainly on the calculation of structural, electronic and magnetic properties of transition-metal clusters. We have also discussed the effect of doping to all these properties in these clusters. Our calculations were always motivated by some experiments, which is very important for a theoretical study. For example, mass abandance spectra, collision-induced dissociation experiments have been done on these clusters studied here in this thesis. Moreover, form the magnetic point of view, the Stern-Gerlach experiments are important to follow and nowadays, experimentalists have achieved to make free standing clusters as small as 5-atoms in it and measure their magnetic properties through cluster beam deflection measurements. We have closely followed all these experiments.

Most of the calculations on structural, electronic and magnetic properties we have used density function theory within the PAW pseudopotential method and we have always

used PBE functional for the exchange-correlation energy. However, we have developed a parametraized tight-binding molecular dynamics to study copper clusters. In the following I, very briefly, describe how the thesis has been evolved.

In the chapter 1 we have introduced the physics of cluster. We have discussed its importance form both the scientific and technological point of view. We also have focused on the experimentally observed unexpected magnetic behaviour in the clusters of transition metal clusters, what has been observed through Stern-Gerlach cluster beam experiments.

In the chapter 2 we have discussed our tight-binding molecular dynamics method, what we have implemented later for copper clusters. We have also discussed the basic ideas of many-body problem from the first-principles and we have also discussed the PAW pseudopotential method briefly. This is used to study Mn_n, As@Mn_n and Co_n clusters.

In the chapter 3 we have implemented the tight-binding molecular dynamics (what we have been discussed in the Chapter 2) with parameters fitted to first-principles calculations on the smaller clusters and with an environment correction, to be a powerful technique for studying large transition/noble metal clusters. In particular, the structure and stability of Cu_n clusters for $n = 3 - 55$ are studied by using this technique. The results for small Cu_n clusters ($n = 3 - 9$) show good agreement with *ab initio* calculations and available experimental results. In the size range $10 \leq n \leq 55$ most of the clusters adopt icosahedral structure which can be derived from the 13-atom icosahedron, the polyicosahedral 19-, 23-, and 26-atom clusters and the 55-atom icosahedron, by adding or removing atoms. However, a local geometrical change from icosahedral to decahedral structure is observed for $n = 40 - 44$ and return to the icosahedral growth pattern is found at $n = 45$ which continues. Electronic "magic numbers" ($n = 2$, 8, 20, 34, 40) in this regime are correctly reproduced. Due to electron pairing in HOMOs, even-odd alternation is found. A sudden loss of even-odd alternation in second difference of cluster binding energy, HOMO-LUMO gap energy and ionization potential is observed in the region $n \sim 40$ due to structural change there. Interplay between electronic and geometrical structure is found.

In the chapter 4 we systematically investigate the structural, electronic and magnetic properties of Mn_n clusters ($n = 2-20$) within the *ab-initio* pseudopotential plane wave method using generalized gradient approximation for the exchange-correlation energy. A new kind of icosahedral structural growth has been predicted in the intermediate size

range. Calculated magnetic moments show an excellent agreement with the Stern-Gerlach experiment. A transition from ferromagnetic to ferrimagnetic Mn−Mn coupling takes place at $n = 5$ and the ferrimagnetic states continue to be the ground states for the entire size range. Possible presence of multiple isomers in the experimental beam has been argued. No signature of non-metal to metal transition is observed in this size range and the coordination dependence of $d-$electron localization is discussed. However, here all the calculations are done under the collinear atomic moment assumption. In this chapter we have discussed Mn_n clusters with the assumption that all the atomic moments align collinearly i.e parallel or anti-parallel to each other. However, spin canting or non-collinearity of the atomic moments often occur in low symmetry systems such as surfaces and clusters.

In the chapter 5 we relaxed our collinear moment assumption and studied how it affects the electronic and magnetic properties of pure Mn_n clusters. No considerable structural change has been found due to noncollinear treatment of atomic moments. The ground state of both pure Mn_n clusters for $n \leq 5$ is collinear and emergence of noncollinear ground states is seen for $n \geq 6$. However, there exists many collinear and noncollinear isomers. Although the results presented here are specific to the Mn_n clusters, they also contain more general picture: noncollinear magnetic ordering is possible in small magnetic clusters.

In the chapter 6 we have discussed properties of As@Mn_n clusters from fully non-collinear treatment. We have discussed how structure, bonding and magnetic properties are perturbed due to single As-doping. We did not See any substantial structural change due to As-doping, rather they can be viewed as As-capped Mn_n structures. However, the binding energy is enhanced substantially due to As-doping and we have concluded that As-atom may act as a nucleation center for Mn-atoms. Similar to the pure Mn_n clusters small clusters show collinear magnetic ordering, whereas noncollinear magnetic structures start to be the ground state for $n \geq 6$ for As@Mn_n clusters. Calculated Mn-Mn exchange coupling in these As@Mn_n clusters show anomalous behaviour, which is found to be quite different from the RKKY-type predictions. All these results were discussed in the context of Mn-clustering in (Ga,Mn)As and (In,Mn)As spintronic materials.

In the chapter 7 we have investigated structure, bonding and magnetism in Co_n clusters in the size range n =2-20, from the first-principle calculation. In the intermediate

size range clusters adopt hcp structural packing. Calculated magnetic moments show same trend as it has been observed in the SG experiments, though they are always underestimated compared to experimental value. It has also been seen that the average coordination number dominates over the average bond length to determine the cluster magnetic moment.

8.1 Outlook

The continuing development of material science and nanostructure technologies make evident the need for detailed theoretical understanding of these systems. Several theoretical approximations have been developed to study their basic properties. Most of these methods provide excellent information on the ground state, although the *ab initio* methods demand typically a substantial computational effort. These methods are then limited to study systems with a somewhat small number of atoms, and only a few calculations of excited properties have been performed. Interesting information has been obtained on dynamical changes in the structure at finite temperatures and the bonding characteristic for larger clusters. Developments in the transferable tight binding method will allow to study larger clusters of metals and semiconductors. In the next few years we hope to see important developments in these directions.

From the point of view of technological applications, clusters of transition metals are very important. Recent development in pseudopotential and their implementation in the *ab initio* method is a interesting problem. But for more work on larger clusters and other systems will be useful with the availability of better computational facility and algorithms which scale linearly with the system size. Due to improved technology, nowadays, it is possible to measure the magnetic moment of free standing clusters as small as 5-atoms in it. This is done through the SG molecular beam experiment. We hope to see SG experiments for even lower size range in the coming years.

From the magnetic point of view of the clusters, it would be interesting to study chemical effect on cluster magnetism and how magnetic properties behave for heterogeneous clusters. However, both the experimental and theoretical investigations are limited on the issues. We hope to see an increased attention to these area of research.

Bibliography

[1] W. A. de Heer, *Rev. Mod. Phys.* **65**, 611 (1993).

[2] M. Brack, *Rev. Mod. Phys.* **65**, 677 (1993).

[3] M. D. Morse, *Chem. Rev.* (Washington, D. C.) **86**, 1049 (1986).

[4] C. E. Moore, *Atomic Energy Levels*, Natl. Bur. Stand. (U. S.) Circ. No. 467 (U. S. GPO, Washington, D. C., 1952), Vol. II.

[5] K. A. Gingerich, *Faraday Discuss. Chem. Soc.* **14**, 109 (1980).

[6] A. Kant, S.-S. Lin and B. Strauss, *J. Chem. Phys.* **49**, 1983 (1968).

[7] A. Terasaki, S. Minemoto and T. Kondow, *J. Chem. Phys.* **117**, 7520 (2002).

[8] M. F. Jarrold, A. J. Illies and M. T. Bowers, *J. Amer. Chem. Soc.* **107**, 7339 (1985).

[9] K. Raghavachari, K. K. Sunhil and K. D. Jordon, *J. Chem. Phys.* **83**, 4633 (1985).

[10] I. Katakuse, T. Ichihara, Y. Fujita, T. Matsuo, T. Sakurai and H. Matsuda, *Int. J. Mass Spectrom. Ion Proc.* **67**, 229 (1985).

[11] I. Katakuse, T. Ichihara, Y. Fujita, T. Matsuo, T. Sakurai and H. Matsuda, *Int. J. Mass Spectrom. Ion Proc.* **74**, 33 (1986).

[12] B. J. Winter, E. K. Parks and S. J. Riley, *J. Chem. Phys.* , **94**, 8618 (1991).

[13] M. B. Knickelbein, *Chem. Phys. Lett.***192**, 129 (1992).

[14] G. Ganteför, M. Gausa, K. H. Meiwes-Broer, H. O. J. Lutz, *Chem. Soc., Faraday Trans.* **86**, 2483 (1990).

[15] D. G. Leopold, J. Ho, W. C. Lineberger, *J. Chem. Phys.* **86**, 1715 (1987).

[16] C. L. Pettiette, S. H. Yang, M. J. Craycraft, J. Conceicao, R. T. Laaksonen, O. Cheshnovsky and R. E. Smalley, *J. Chem. Phys.* , **88**, 5377 (1988).

[17] A. J. Cox, J. G. Louderback and L. A. Bloomfield, *Phys. Rev. Lett.* **71**, 923 (1993); A. J. Cox, J. G. Louderback, S. E. Apsel and L. A. Bloomfield, *Phys. Rev. B* **49**, 12295 (1994).

[18] I. M. L. Billas, J. A. Becker, A. Chatelain and W. A. de Heer, *Phys. Rev. Lett.* **71**, 4067 (1993); D. M. Cox, D. J. Trevor, R. L. Wheetten, E. A. Rohlfing and A. Kaldor, *Phys. Rev. B* **32**, 7290 (1985).

[19] J. P. Bucher, D. C. Douglass and L. A. Bloomfield, *Phys. Rev. Lett.* **66**, 3052 (1999).

[20] D. C. Douglass, A. J. Cox, J. P. Bucher and L. A. Bloomfield, *Phys. Rev. B* **47**, 12874 (1993).

[21] I. M. L. Billas, A. Chatelain, and W. A. de Heer, *Science* **265**, 1682 (1994); I. M. L. Billas, A. Chatelain, and W. A. de Heer, *J. Magn. Magn. Mater.* **168**, 64 (1997); D. Gerion, A. Hirt, I. M. L. Billas, A. Chatelain, and W. A. de Heer, *Phys. Rev. B* **62**, 7491 (2000).

[22] M. B. Knickelbein, *J. Chem. Phys.* **125**, 044308 (2006).

[23] Xiaoshan Xu, Shuangye Yin, Ramiro Moro and Walt A. de Heer, *Phys. Rev. Lett.* **95**, 237209 (2005).

[24] C. Kittel, *Introduction to Solid State Physics* (Wiley, New York, 1996), 7th ed.

[25] L. A. Bloomfield, J. Deng, H. Zhang and J. W. Emmert, in *Proceedings of the International Symposium on Cluster and Nanostructure Interfaces*, edited by P. Jena, S. N. Khanna and B. K. Rao (World Publishers, Singapore, 2000), p.131

[26] M. B. Knickelbein, *Phys. Rev. Lett.* **86**, 5255 (2001).

[27] M. B. Knickelbein, *Phys. Rev. B* **70**, 14424 (2004).

[28] O. K. Andersen and T. Saha-Dasgupta, *Phys. Rev. B* **62**, R16219 (2000)

[29] J. C. Slater and G. F. Koster, *Phys. Rev.* **94**, 1498 (1954).

[30] N. Lathiotakis, A. Andriotis, M. Menon and J. Connolly, *J. Chem. Phys.* , **104**, 992 (1996).

[31] W. A. Harrison, *Electronic Structure and the Properties of Solids* (Dover,1989).

[32] D. Tomaǹek and M. Schluter, *Phys. Rev.* B **36**, 1208 (1987).

[33] R. P. Feynman, *Phys. Rev.* **56**, 340 (1939).

[34] W. C. Swope, H. C. Anderson, P. H. Berenes and K. R. Wilson, *J. Chem. Phys.* **76**, 637 (1982).

[35] M. S. Methfessel and van M. Schilfgaarde, *Phys. Rev.* B, **48**, 4937 (1993); *Int. J. Mod. Phys.* B, **7**, 262 (1993); M. S. Methfessel, van M. Schilfgaarde and M. Schaffler, *Phys. Rev. Lett.* **70**, 29 (1993).

[36] D. M. Deaven and K. M. Ho, *Phys. Rev. Lett.* , **75**, 288 (1995); D. M. Deaven, N. Tit, J. R. Morris and K. M. Ho, *Chem. Phys. Lett.*, **256**, 195 (1996).

[37] B. Hartke, *Chem. Phys. Lett.*, **240**, 560 (1995).

[38] Y. H. Luo, J. J. Zhao, S. T. Qiu and G. H. Wang, *Phys. Rev.* B, **59**, 14903 (1999).

[39] J. A. Niesse and H. R. Mayne, *Chem. Phys. Lett.*, **261**, 576 (1996); *J. Chem. Phys.* , **105**, 4700 (1996).

[40] P. Hohenberg and W. Kohn, *Phys. Rev. B* **136**, 864 (1964).

[41] W. Kohn and L. J. Sham, *Phys. Rev. A* **140**, 1133 (1965).

[42] Y. Wang, *Phys. Rev. B* **54**, 16533 (1996).

[43] J.P. Perdew and A. Zunger, *Phys. Rev. B* **23**, 5048 (1981).

[44] D.M. Ceperley and B.J. Alder, *Phys. Rev. Lett.* **45**, 566 (1980).

[45] L. Hedin and B.I. Lundqvist, *J. Phys. C* **4**, 2064 (1971).

[46] E.P. Wigner, *Phys. Rev.* **46**, 1002 (1934); see also R.M. Dreizler and E.K.U. Gross, *Density Functional Theory*, Springer, New York (1990).

[47] A.H. MacDonald and S.H. Vosko, *J. Phys. C* **12**, 2977 (1979).

[48] J. P. Perdew, K. Burke and M. Ernzerhof, *Phys. Rev. Lett.* **77**, 3865 (1996).

[49] A.D. Becke, *Phys. Rev. A* **38**, 3098 (1988).

[50] J.P. Perdew, *Phys. Rev. B* **34**, 7406 (1986).

[51] C. Lee, W. Yang and R.G. Parr, *Phys. Rev. B* **37**, 785 (1988).

[52] O.K. Andersen, *Phys. Rev. B* **12**, 3060 (1975).

[53] J.C. Slater, *Phys. Rev.* **51**, 846 (1937). .

[54] P.M. Marcus, *Int. J. Quantum. Chem.* **1S**, 567 (1967).

[55] J. Korringa, *Physica* **13**, 392 (1947).

[56] W. Kohn and N. Rostocker, *Phys. Rev.* **94**, 111 (1954).

[57] D.R. Hamann, M. Schlüter and C. Chiang, *Phys. Rev. Lett.* **43**, 1494 (1979).

[58] D. Vanderbilt, *Phys. Rev. B* **41**, 7892 (1985) .

[59] P. E. Blöchl, *Phys. Rev. B* **50**, 17953 (1994).

[60] G. Kresse and D. Joubert, *Phys. Rev. B* **59**, 1758 (1999).

[61] P. Pulay, in *Modern Theoretical Chemistry*, edited by H. F. Schaefer (Plenum, New York, 1977); Mol Phys. **17**, 197 (1969).

[62] S. Goedecker and K. Maschke, *Phys. Rev. B* **45**, 1597 (1992).

[63] M. Valden, X. Lai and D. W. Goodman, *Science* **281**, 1647 (1998)

[64] M. B. Kinickelbein, *Annu. Rev. Phys. Chem.* **50** 79 (1999)

[65] S. H. Joo, S. J. Choi, I. Oh, J. Kwak, Z. Liu, O. Terasaki and R. Ryoo, *Nature* (London) **412**, 169 (2001).

[66] P. L. Hansen, J. B. Wagner, S. Helveg, J. R. Rostrup-Nielsen, B. S. Clausen and H. Topsoe, *Science* **295**, 2053 (2002).

[67] C. Binns, *Surf. Sci. Rep.* **44**, 1 (2001).

[68] S. J. Park, T. A. Taton and C. A. Mirkin, *Science* **295**, 1503 (2002).

[69] D. I. Gittins, D. Bethell, D. J. Schiffrin and R. J. Nicolas, *Nature* (London) **408**, 67 (2000).

[70] J. Tiggesbaumker, L. Koller, K. Meiwes-Broer and A. Liebsch, *Phys. Rev.* A **48**, 1749 (1993).

[71] G. Apai, J. F. Hamilton, J. Stohr and A. Thompson, *Phys. Rev. Lett.* **43**, 165 (1979).

[72] A. Balerna, E. Bernicri, P. Piccozi, A. Reale, S. Santucci, E. Burrattini and S. Mobilio, *Surf. Sci.* **156**, 206 (1985).

[73] P. A. Montano, H. Purdum, G. K. Shenoy, T. I. Morrison and W. Schultze, *Surf. Sci.* **156**, 216 (1985).

[74] K. J. Taylor, C. L. Pettiette-Hall, O. Cheshnovsky and R. E. Smalley, *J. Chem. Phys.* **96**, 3319 (1992).

[75] J. Ho, K. M. Ervin and W. C. Lineberger, *J. Chem. Phys.* **93**, 6987 (1990).

[76] V. A. Spasov, T. H. Lee and K. M. Ervin, *J. Chem. Phys.* **112**, 1713 (2000).

[77] C. Massobrio, A. Pasquarello, R. Car, *Chem. Phys. Lett.*, **238**, 215 (1995).

[78] P. Calaminici, A. M. Köster, N. Russo, and D. R. Salahub, *J. Chem. Phys.* **105** 9546 (1996).

[79] H. Akeby, I. Panas, L. G. M. Pettersson, P. Seigbahn and U. Wahlgren, *J. Chem. Phys.* **94** 5471 (1990).

[80] M. Kabir, A. Mookerjee, R. P. Datta, A. Banerjea and A. K. Bhattacharya *Int. J. Mod. Phys.* B **17**, 2061 (2003).

[81] G. D'Agostino, *Philos. Mag. B* **68**, 903 (1993).

[82] R. P. Gupta, *Phys. Rev.* B, **23**, 6265 (1983).

[83] S. Darby, T. V. Mortimer-Jones, R. L. Johnston and C. Roberts, *J. Chem. Phys.* , **116**, 1536 (2002).

[84] M. Menon and R. E. Allen, *Phys. Rev.* B **33**, 7099 (1986); **38**, 6196 (1988).

[85] M. Menon and K. R. Subbaswamy, *Phys. Rev.* B **47**, 12754 (1993); **50**, 11577 (1994); **51**, 17952 (1996).

[86] P. Ordejón, D. Lebedenko and M. Menon, *Phys. Rev.* B, **50**, 5645 (1994).

[87] M. Menon, J. Connolly, N. Lathiotaki and A. Andriotis, *Phys. Rev.* B, **50**, 8903 (1994).

[88] J. Zhao, Y. Luo and G. Wang, *Eur. Phys. J.* D, **14**, 309 (2001).

[89] N. Aslund, R. F. Barrow, W. G. Richards and D. N. Travis, *Ark. Fys.* **30** 171 (1965).

[90] K. P. Huber and G. Herzberg, *Molecular Spectra and Molecular Structure*, Vol. IV (Van Nostrand-Reinhold, New York, 1989).

[91] C. W. Bauschlicher, Jr., S. R. Langhoff and H. Partridge, *J. Chem. Phys.* **91**, 2412 (1989); C. W. Bauschlicher, Jr., *Chem. Phys. Lett.***156**, 91 (1989).

[92] U. Lammers and G. Borstel, *Phys. Rev.* B, **49**, 17360 (1994).

[93] Y. Wang, T. F. George, D. M. Lindsay and A. C. Beri, *J. Chem. Phys.* , **86**, 3593 (1987); D. M. Lindsay, L. Chu, Y. Wang and T. F. George, *ibid.* **87**, 1685 (1987).

[94] S. Valkealahti and M. Manninen, *Phys. Rev.* B, **45**, 9459 (1992).

[95] O. B. Christensen and K. W. Jacobsen, *J. Phys.: Condens. Matter* **5**, 5591 (1993).

[96] O. B. Christensen, K. W. Jacobsen, J. K. Norskov and M. Mannien, *Phys. Rev. Lett.* , **66**, 2219 (1991).

[97] Even a small variation in the parameters (in particular parameter q) in the Gupta potential can lead to changes in the global minima. *see*- K. Michaelian, N. Rendon and I. L. Garzón, *Phys. Rev.* B **60**, 2000 (1999).

[98] The set of SK-TB parameters in this scheme implies that within the Koopmans' theorem, ionization potentials are approximately equal to the on-site energy $E_s = E_d$, which is usually much higher than highest occupied s-orbital energy of the free atom. A constant shift is made in plotting of the Fig.3.6. *See* Ref.[30].

[99] R. E. Cohen, H. J. Mehl and D. A. Papaconstantopoulos, *Phys. Rev.* B **50**, 14694, (1994).

[100] K. Tono, A. Terasaki, T. Ohta and T. Kondow, *J. Chem. Phys.* **123**, 174314 (2005).

[101] R. J. Van Zee and W. Weltner,Jr., *J. Chem. Phys.* **89**, 4444 (1988); C. A. Bauman, R. J. Van Zee, S. Bhat, and W. Weltner,Jr., *J. Chem. Phys.* **78**, 190 (1983).

[102] S. K. Nayak, B. K. Rao and P. Jena, *J. Phys.: Condens. Matter* **10**, 10863 (1998).

[103] S. K. Nayak and P. Jena, *Chem. Phys. Lett.* **289**, 473 (1998).

[104] M. R. Pederson, F. Ruse and S. N. Khanna, *Phys. Rev. B* **58**, 5632 (1998).

[105] S. K. Nayak, M. Nooijen and P. Jena, *J. Phys. Chem. A* **103**, 9853 (1999).

[106] P. Bobadova-Parvanova, K. A. Jackson, S. Srinivas and M. Horoi, *Phys. Rev. A* **67**, R61202 (2003).

[107] P. Bobadova-Parvanova, K. A. Jackson, S. Srinivas and M. Horoi, *J. Chem. Phys* **122**, 14310 (2005).

[108] N. O. Jones, S. N. Khanna, T. Baruah and M. R. Pederson, *Phys. Rev. B* **70**, 45416 (2004).

[109] T. M. Briere, M. H. F. Sluiter, V. Kumar and Y. Kawazoe, *Phys. Rev. B* **66**, 64412 (2002).

[110] E. K. Parks, G. C. Nieman and S. J. Riley, *J. Chem. Phys.* **104**, 3531 (1996).

[111] G. M. Koretsky and M. B. Knickelbein, *J. Chem. Phys.* **106**, 9810 (1997).

[112] G. Kresse and J. Furthmuller, *Phys. Rev. B* **54**, 11169 (1996).

[113] R. K. Nesbet, *Phys. Rev.* **135**, A460 (1964).

[114] D. D. Shillady, P. Jena, B. K. Rao, and M. R. Press, *Int. J. Quantum Chem.* **22**, 231 (1998).

[115] K. D. Bier, T. L. Haslett, A. D. Krikwood and M. Moskovits, *J. Chem. Phys.* **89**, 6 (1988).

[116] R. J. Van Zee and W. Weltner,Jr., *J. Chem. Phys.* **89**, 4444 (1988); C. A. Bauman, R. J. Van Zee, S. Bhat, and W. Weltner,Jr., *J. Chem. Phys.* **78**, 190 (1983); R. J. Van Zee, C. A. Baumann and W. Weltner, *J. Chem. Phys.* **74**, 6977 (1981).

[117] P. Bobadova-Parvanova, K. A. Jackson, S. Srinivas and M. Horoi, *Phys. Rev. A* **67**, 61202 (2003); *J. Chem. Phys.* **122**, 14310 (2005).

[118] A. Wolf and H-H. Schmidtke, *Int. J. Quantum Chem.* **18**, 1187 (1980).

[119] N. Fujima and T. Yamaguchi, *J. Phys. Sols Japan* **64**, 1251 (1995).

[120] J. Harris and R. O. Jones, *J. Chem. Phys.* **70**, 830 (1979).

[121] D. R. Salahub and N. A. Baykara, *Surf. Sci.* **156**, 605 (1985).

[122] G. W. Ludwig, H. H. Woodbury and R. O. Carlson, *J. Phys. Chem. Solids* **8**, 490 (1959).

[123] S. N. Khanna, B. K. Rao, P. Jena and M. B. Knickelbein, *Chem. Phys. Lett.* **378**, 374 (2003).

[124] M. Kabir, A. Mookerjee and A. K. Bhattacharya, *Eur. Phy. J. D* **31**, 477 (2004).

[125] M. Kabir, A. Mookerjee and A. K. Bhattacharya, *Phys. Rev. A* **69**, 043203 (2004).

[126] M. Kabir, D. G. Kanhere and A. Mookerjee, *Phys. Rev. B* **73**, 75210 (2006).

[127] B. K. Rao and P. Jena, *Phys. Rev. Lett.* **89**, 185504 (2002).

[128] K. Rademann, B. Kaiser, U. Even, and F. Hensel, *Phys. Rev. Lett.* **59**, 2319 (1987).

[129] R. Lorenz, J. Hafner, S. S. Jaswal, and D. J. Sellmyer, *Phys. Rev. Lett.* **74**, 3688 (1995).

[130] M. Liebs, K. Hummler and M. Fähnle, *Phys. Rev. B* **51**, 8664 (1995).

[131] Y Tsunoda, *J. Phys.: Condens. Matter* **1**, 10427 (1989).

[132] O. N. Mryasov, A. I. Liechtenstein, L. M. Sandratskii and V A Gubanov, *J. Phys.: Condens. Matter* **3**, 7683 (1991).

[133] H. Zabel, *J. Phys.: Condens. Matter* **11** 9303 (1999).

[134] T. Oda, A. Pasquarello and R. Car, *Phys. Rev. Lett.* **80**, 3622 (1998).

[135] O. Ivanov and V. P. Antropov, *J. Appl. Phys.* **85**, 4821 (1999).

[136] D. Hobbs, G. Kresse and J. Hafner, *Phys. Rev. B* **62**, 11556 (2000).

[137] R. S. Tebble and D. J. Craik, *Magnetic Materials* (Wiley, New York, 1969) p. 48.

[138] D. Hobbs, J. Hafner, and D. Spiák, *Phys. Rev. B* **68**, 14407 (2003).

[139] J. Hafner and D. Hobbs, *Phys. Rev. B* **68**, 14408 (2003).

[140] C.G. Shull and M.K. Wilkinson, *Rev. Mod. Phys.* **25**, 100 (1953); J.S. Kasper and B.W. Roberts, *Phys. Rev.* **101** 537 (1956); J.A. Oberteuffer, J.A. Marcus, L.H. Schwartz, and G.P. Felcher, *Phys. Lett.* **28A**, 267 (1969); N. Kunitomi, Y. Yamada, Y. Nakai, and Y. Fujii, *J. Appl. Phys.* **40**, 1265 (1969); T. Yamada, N. Kunitomi, Y. Nakai, D.E. Cox, and G. Shirane, *J. Phys. Soc. Jpn.* **28**, 615 (1970); A.C. Lawson, A.C. Larson, M.C. Aronson, S. Johnson, Z. Fisk, P.C. Canfield, J.D. Thompson, and R.B. Von Dreele, *J. Appl. Phys.* **76**, 7049 (1994).

[141] T. Yamada and S. Tazawa, *J. Phys. Soc. Jpn.* **28**, 609 (1970).

[142] H. Yamagata and K. Asayama, *J. Phys. Soc. Jpn.* **33**, 400 (1972).

[143] T. Morisato, S. N. Khanna and Y. Kawazoe, *Phys. Rev. B* **72**, 014435 (2005).

[144] R. C. Longo, E. G. Noya, and L. J. Gallego, *Phys. Rev. B* **72**, 174409 (2005).

[145] A. Bergman, L. Nordström, A. B. Klautau, S. Frota-Pessoa and O. Eriksson; *arXiv:cond-mat/0511542* (2005).

[146] U. von Barth and L. Hedin, *J. Phys. C* 5, 1629 (1972).

[147] L.M. Sandratskii and P.G. Guletskii, *J. Phys. F: Met. Phys.* 16, L43 (1986).

[148] J. Kübler, K. H. Höck, and J. Sticht, *J. Appl. Phys.* 63, 3482 (1988).

[149] J. Kübler, K.H. Höck, J. Sticht, and A.R. Williams, *J. Phys. F: Met. Phys.* 18, 469 (1988).

[150] S. T. Bramwell and M. J. P. Gingras, *Science* **294**, 1495 (2001).

[151] M. Kabir, D. G. Kanhere and A. Mookerjee, *Phys. Rev. B* **73**, 75210 (2006).

[152] M. van Schilfgaarde and O. N. Mryasov, *Phys. Rev. B* **63**, 233205 (2001).

[153] J. M. Sullivan, G. I. Boishin, L. J. Whitman, A. T. Hanbicki, B. T. Jonker, and S. C. Erwin, *Phys. Rev. B* **68**, 235324 (2003).

[154] M. Zajac, J. Gosk, E. Grzanka, M. Kamińska, A. Twardowski, B. Strojek, T. Szyszko, and S. Podsiadlo, *J. Appl. Phys.* **93**, 4715 (2003).

[155] D. C. Kundaliya, S. B. Ogale, S. E. Lofland, S. Dhar, C. J. Metting, S. R. Shinde, Z. Ma, B. Varughese, K.V. Ramanujachary, L. Salamanca-Riba, T. Venkatesan, *Nature Materials* **3**, 709 (2004).

[156] K.M.Yu, W. Walukiewicz, T. Wojtowicz, I. Kuryliszyn, X. Liu, Y. Sasaki, and J. K. Furdyna, *Phys. Rev. B* **65**, 201303 (2002).

[157] P. Mahadevan and A. Zunger, *Phys. Rev. B* **68**, 75202 (2003).

[158] J. L. Xu, M. van Schilfgaarde and G. D. Samolyuk, *Phys. Rev. Lett.* **94**, 97201 (2005).

[159] L. Bergqvist, O. Eriksson, J. Kudrnovský, V. Drchal, P. Korzhavyi, and I. Turek, *Phys. Rev. Lett.* **93**, 137202 (2004).

[160] J. Blinowski and P. Kacman, *Phys. Rev. B* **67**, 121204 (2003).

[161] S. J. Potashnik, K. C. Ku, S. H. Chun, J. J. Berry, N. Samarth, and P. Schiffer, *Appl. Phys. Lett.* **79**, 1495 (2001).

[162] S. Sanvito and N. A. Hill, *Appl. Phys. Lett.* **78**, 3493 (2001).

[163] P. A. Khorzhavyi, I. A. Abrikosov, E. A. Smirnova, L. Bergqvist, P. Mohn, R. Mathieu, P. Svedlindh, J. Sadowski, E. I. Isaev, Yu. Kh. Vekilov, and O. Eriksson, *Phys. Rev. Lett.* **88**, 187202 (2002).

[164] D. Chiba, K. Tankamura, F. Matsukura and H. Ohno, *Appl. Phys. Lett.* **82**, 3020 (2003).

[165] K. W. Edmonds, P. Boguslawski, K. Y. Wang, R. P. Campion, S. N. Novikov, N. R. S. Farley, B. L. Gallagher, C. T. Foxon, M. Sawicki, T. Dietl, M. B. Nardelli, and J. Bernholc, *Phys. Rev. Lett.* **92**, 37201 (2004).

[166] K. C. Ku, S. J. Potashnik, R. F. Wang, S. H. Chun, P. Schiffer, N. Samarth, M. J. Seong, A. Mascarenhas, E. Johnston-Halperin, R. C. Myers, A. C. Gossard, and D. D. Awschalom, *Appl. Phys. Lett.* **82**, 2302 (2003).

[167] J. Kudrnovský, I. Turek, V. Drchal, F. Mca, P. Weinberger, and P. Bruno, *Phys. Rev. B* **69**, 115208 (2004).

[168] S. C. Erwin and C. S. Hellberg, *Phys. Rev. B* **68**, 245206 (2003).

[169] L. M. Sandratskii and P. Bruno, *Phys. Rev. B* **66**, 134435 (2002).

[170] G. Bouzerar, J. Kudrnovský, L. Bergqvist, and P. Bruno, *Phys. Rev. B* **68**, R081203 (2003).

[171] M. Sato, H. Katayama-Yoshida, and P. Dederics, *Europhys. Lett.* **61**, 403 (2003).

[172] K. Sato, W. Schweika, P. H. Dederichs and H. Katayama-Yoshida, *Phys. Rev. B* **70**, R201202 (2004).

[173] G. Bouzerar, T. Ziman1 and J. Kudrnovský, *Europhys. Lett.* **69**, 812 (2005).

[174] L. Bergqvist, O. Eriksson, J. Kudrnovský, V. Drchal, A. Bergman, L. Nordström, and I. Turek, *Phys. Rev. B* **72**, 195210 (2005).

[175] S. J. Potashnik, K. C. Ku, R. Mahendiran, S. H. Chun, R. F. Wang, N. Samarth, and P. Schiffer, *Phys. Rev. B* **66**, 012408 (2002).

[176] J. Schliemann and A. H. MacDonald, *Phys. Rev. Lett.* **88**, 137201 (2002).

[177] J. Schliemann, *Phys. Rev. B* **67**, 045202 (2003).

[178] G. A. Fiete, G. Zaránd, B. Jankó, P. Redliski, and C. P. Moca, *Phys. Rev. B* **71**, 115202 (2005).

[179] Due to the negative polarization of the As-atom, the summation in the Equation 5.3 includes the As-atom too for As@Mn_n clusters.

[180] W. Eckartdt, Phys. Rev. B, **29**, 1558 (1984); W. D. Knight, K. Clemenger, W. A. de Heer, W. A. Saunders, M. Y. Chou, and M. L. Cohen, *Phys. Rev. Lett.* **52**, 2141 (1984).

[181] I. A. Harris, K. A. Norman, R. V. Mulkern, and J. A. Northby, *Chem. Phys. Lett.* **130**, 316 (1984); J. Farges, M. F. de Feraudy, B. Raoult, and G. Torchet, *J. Chem. Phys.* **84**, 3491 (1986).

[182] B. I. Min, T. Oguchi and A. J. Freeman, *Phys. Rev. B* **33**, R7852 (1986).

[183] M. Pereiro, S. Man'kovsky, D. Baldomir, M. Iglesias, P. Mlynarski, M. Valladares, D. Suarez, M. Castro, J. E. Arias, *Comp. Materials Science* **22**, 118 (2001).

[184] J. P. Bucher, D. C. Douglass and L. A. Bloomfield, *Phys. Rev. Lett.* **66**, 3052 (1991); D. C. Douglass, A. J. Cox, J. P. Bucher and L. A. Bloomfield, *Phys. Rev. B* **47**, 12874 (1993).

[185] T. D. Klots, B. J. Winter, E. K. Parks, and S. J. Riley, *J. Chem. Phys.* **95**, 8919 (1991).

[186] E. K. Parks, B. J. Winter, T. D. Klots, and S. J. Riley, *J. Chem. Phys.* **96**, 8267 (1992).

[187] M. Pellarin, B. Baguenard, J. L. Vialle, J. Lerme, M. Broyer, J. Miller, and A. Perez, *Chem. Phys. Lett.* **217**, 349 (1994).

[188] Z.-Q. Li and B L. Gu, *Phys. Rev. B* **47**, 13611 (1993).

[189] J. Guevara, F. Parisi, A. M. Llois, and M. Weissmann, *Phys. Rev. B* **55**, 13283 (1997).

[190] A. N. Andriotis, and M. Menon, *Phys. Rev. B* **57**, 10069 (1998).

[191] J. L. Rodriguez-Lopez, F. Aguilera-Granja, K. Michaelian, and A. Vega, Phys. Rev. B, **67**, 174413 (2003).

[192] D. A. Hales, C. - X. Su, L. Lian, and P. B. Armentrout, *J. Chem. Phys.* **100**, 1049 (1994).

[193] D. G. Leopold, W. C. Lineberger, *J. Chem. Phys.* **85**, 51 (1986).

[194] P. B. Armentrout, D. A. Hales, and L. Lian, in Advances in Metal and Semiconductor Clusters, edited by M. A. Duncan (JAI, Greenwich, in press), Vol. II.

[195] A. Kant, B. Strauss, *J. Chem. Phys.* **41**, 3806 (1964).

[196] I. Shim and K. A. Gingerich, *J. Chem. Phys.* **78**, 5693 (1983).

[197] M. Castro, C. Jamorski, D. R. Salahub, *Chem. Phys. Lett.* **271**, 133 (1997); *Phys. Rev. B* **67**, 174413 (2003).

[198] H.- J. Fan, C.- W. Liu, M.-S. Liao, *Chem. Phys. Lett.* **273**, 353 (1997).

[199] H. Yoshida, A. Terasaki, K. Kobayashi, M. Tsukada and T. Kondow, *J. Chem. Phys.* **102**, 5960 (1995).

[200] Q.- M. Ma, Z. Xie, J. Wang, Y. Liu, Y.- C. Li, *Phys. Lett. A* **358**, 289 (2006)

[201] S. Yang and M. Knickelbein, *J. Chem. Phys.* **93**, 1533 (1990).

[202] E. K. Parks, T. D. Klots, and S. J. Riley, *J. Chem. Phys.* **92**, 3813 (1990).